

Exploration of Charge Transport Phenomena in Transition Metal Oxides for Energy Technologies

dem Fachbereich Mathematik und Informatik, Physik,
Geographie der Justus-Liebig-Universität Gießen vorgelegte

Dissertation

zur Erlangung des Grades
Doktor der Naturwissenschaften
– **Dr. rer. nat.** –

von
Simon Burkhardt
geboren am 28. Dezember 1991
in Alsfeld

Gießen 2019

Dean / Dekan Prof. Dr. Kai-Thomas Brinkmann

1. Reviewer / Gutachter Prof. Dr. Peter J. Klar

2. Reviewer / Gutachter Prof. Dr. Jürgen Janek

Submitted / eingereicht 11. November 2019

Die vorliegende Arbeit wurde im Zeitraum vom 1. Oktober 2016 bis 11. November 2019 im Rahmen des Graduiertenkollegs 2204 „Substitutionsmaterialien für nachhaltige Energietechnologien“ der Deutschen Forschungsgemeinschaft am I. Physikalischen Institut, sowie am Physikalisch-Chemischen Institut der Justus-Liebig-Universität Gießen unter Betreuung von Prof. Dr. Peter J. Klar und Prof. Dr. Jürgen Janek angefertigt.

Ich erkläre: Ich habe die vorgelegte Dissertation selbstständig und ohne unerlaubte fremde Hilfe und nur mit den Hilfen angefertigt, die ich in der Dissertation angegeben habe. Alle Textstellen, die wörtlich oder sinngemäß aus veröffentlichten Schriften entnommen sind, und alle Angaben, die auf mündlichen Auskünften beruhen, sind als solche kenntlich gemacht. Ich stimme einer evtl. Überprüfung meiner Dissertation durch eine Antiplagiat-Software zu. Bei den von mir durchgeführten und in der Dissertation erwähnten Untersuchungen habe ich die Grundsätze guter wissenschaftlicher Praxis, wie sie in der „Satzung der Justus-Liebig-Universität Gießen zur Sicherung guter wissenschaftlicher Praxis“ niedergelegt sind, eingehalten.

Gießen, den 11. November 2019

.....
Simon Burkhardt

Table of Contents

1	Summary	7
2	Introduction	9
3	Fundamentals	13
3.1	Electrochromism and Electrochromic Materials	13
3.2	Properties of WO ₃ Thin Films	17
3.2.1	Electrochromic Coloration in WO ₃	22
3.2.2	Charge Transport and Diffusion in WO ₃	25
3.3	Electrochemical Energy Storage and Lithium-Ion Batteries	28
3.4	Positive Electrode Materials for Lithium-Ion Batteries	32
4	Results and Discussion	37
4.1	Diffusion of Hydrogen in WO ₃ Thin Films (Publication 1)	37
4.2	Charge Transport in Single NCM 111 Secondary Particles (Publication 2)	48
5	Conclusions and Outlook	59
	References	63
	Appendix	79
A	Cell Design for Simultaneous Electrochemical and Optical Experiments on Thin Films	79
B	Supporting Information on Publication 1	82
C	Cell Design for Investigations on Single Particles	85
D	Supporting Information on Publication 2	88
	Acknowledgments	99

1 Summary

This Ph.D. project has been devoted to the exploration of charge transport phenomena in transition metal oxide (TMO) thin films and particles. For this purpose, new experimental methods combining microfabrication processes with different characterization methods from the fields of electrochemistry and/or optical spectroscopy were developed. These methods were employed to study the diffusion of hydrogen in tungsten trioxide (WO_3) thin films, as well as electronic and ionic charge transport in single micrometer-sized lithium-nickel-cobalt-manganese-oxide ($\text{LiNi}_{1/3}\text{Co}_{1/3}\text{Mn}_{1/3}\text{O}_2$, NCM 111) secondary particles.

By optically monitoring the diffusion of hydrogen in WO_3 thin films, which resulted from the generation of a concentration gradient due to locally confined hydrogen insertion, the influence of the thin film morphology on the diffusion process was studied. The experimental data were modeled by simulations using a concentration-dependent diffusion process. Contrary to what is reported in the literature on WO_3 thin films, the diffusion of hydrogen in polycrystalline thin films is faster than in amorphous thin films. Additionally, direct evidence for the influence of the hydrogen concentration on the diffusion processes was given, which differs depending on the thin film morphology. This novel finding potentially challenges the interpretation of experimental results from earlier studies on this material reported in literature. The results led to the first publication “*In Situ Monitoring of Lateral Hydrogen Diffusion in Amorphous and Polycrystalline WO_3 Thin Films*”.

The investigation of charge transport in single secondary NCM 111 particles was aimed at the characterization of ionic and electronic charge transport in single micrometer-sized particles of this material. As an electrochemically active material, which has the ability to reversibly store Li^+ ions, it is used in cathodes in lithium-ion batteries (LIBs) and therefore belongs to the group of “cathode active materials” (CAMs). Although several reports on the investigation of electrochemical properties of single CAM particles can be found in the literature, ionic and electronic charge transport have not been studied on a single particle level before; thus the goal was to fill this experimental gap. This involved the development of a specially designed cell, the preparation of samples containing immobilized single particles on defined positions, the actual execution of different electrochemical experiments on single particles, the implementation of simulations, and modeling the observed correlations between derived parameters and the particle size. The results of these experiments and simulations suggested that the method introduced offers a successful approach for investigating charge transport on single-particle level and revealed an aspect of charge transport in such particles, which has not been previously reported: the identification of the preferred conduction pathways for lithium ions and electrons in this mixed-conducting material. The second publication “*Charge Transport in Single NCM Cathode Active Material Particles*

for Lithium-Ion Batteries Studied under Well-Defined Contact Conditions” discusses the corresponding findings.

In order to put the content of this thesis into a wider perspective, a short *Introduction* in an eponymous section is provided. The following section *Fundamentals* gives some basic information about the material systems investigated to facilitate the understanding of the results illustrated by the two peer-reviewed publications in the section *Results and Discussion*. The last section of this thesis *Conclusions and Outlook* summarizes the content and outlines future tasks and opportunities for further research, to which the presented experimental approaches provide access.

2 Introduction

In 2018, the growth rate of global energy consumption (2.3 %) was nearly twice the average growth rate of the past decade [1]. This increasing pace is accompanied by the highest growth rate of the global energy-related carbon dioxide (CO₂) emissions (1.7 %) since 2013 [1]. There is a very strong consensus among climate scientists that the origin of climate change occurring is anthropogenic [2, 3]. Thus, there is a high demand for technologies capable of reducing global energy consumption and CO₂ emissions. Meeting this demand should be considered an important measure in assuming responsibility toward developing countries, which contribute less to climate change but are acutely vulnerable to negative impacts [4], and toward future generations.

This circumstance, among others, is driving a constant advancement of existing and new technologies, especially in the sectors of building and construction as well as transportation, due to their large contribution to both the global energy consumption (64 % in 2018) and the global energy-related CO₂ emissions (62 % in 2018) [1]. Such an advancement leads to a multitude of new materials, with ever-increasing variety [5]. In most cases these new materials are investigated according to applications they are intended for. Such a restriction is necessary to enable a feasible and economic optimization along with a direct assessment of the material of choice in terms of performance in an application. However, criteria other than the ability of a material to enable certain applications due to its properties potentially fade from the spotlight, despite having a crucial role in sustainability. Such criteria may take into account different aspects such as the availability of natural or human resources, energy, time, or money, which are required for the production, recycling, or waste management, under given geopolitical, socio-economic, or governmental circumstances and regulations. The priority of each criterion strongly depends on the material system of interest and the time at which these criteria are assessed. Materials that are more affected by these criteria than others are often called “critical” materials [6, 7] which, according to the definition of criticality in terms of the European Commission [8], are characterized by a high supply risk and a high economic importance.

This applies to the transition metals tungsten and cobalt [9], whose oxides exhibit valuable properties for certain “energy technologies”, i.e., technologies with a high potential for reducing global energy consumption and global energy-related CO₂ emissions. The fact that tungsten and cobalt are considered critical is the result of studies that have evaluated many of the aspects mentioned above. Details on the assessment of the criticality of tungsten and cobalt can be found in the literature [8, 9]. Some aspects worth mentioning are listed here to understand their diversity and scope:

- Unique material properties reduce the possibilities for substitution. For instance, cobalt has the highest known Curie temperature at 1121 °C [8]; tungsten has a melting point of 3422 °C, which is the highest melting point of all elements. It also has a comparably high density of 19.3 g cm⁻³ [10], and the use of both materials can increase the hardness or the corrosion resistance of an alloy [8].
- Unevenly distributed shares of the global mine production potentially increase the supply risk. Between 2010 and 2014, 84 % of the world’s tungsten production came from China and 64 % of the world’s cobalt production came from the Democratic Republic of Congo (DRC) (five-year averages) [8].
- The purchase of cobalt and tungsten has a high potential to support armed groups and illegal mining, and consequently human rights violations and adverse working conditions in the mines. Tungsten and its minerals are considered a conflict material/mineral; the supply chain is the subject of a European Union regulation that comes into effect on January 1st, 2021 [8, 11] and the Dodd-Frank Wall Street Reform and Consumer Protection Act of the US government [12]. The latter also affects other minerals, which potentially finance conflicts in the DRC and other countries [12].

It is desirable to reduce the extent by which a product and its price are affected by such aspects. One way this can be achieved is by replacing critical materials with less critical ones, or by reducing the amount required for a given product to meet the desired specifications. This requires a detailed understanding of the material properties and the microscopic processes, which determine the specifications of an application but are not well understood due to their complexity. While this understanding is not a requirement for an empirical optimization process, it is very attractive from a scientific point of view and crucial for the development of new applications, systematic approaches regarding the adjustment of certain material properties, or the reduction and substitution of critical materials. This especially holds true for transition metals and transition metal oxides (TMOs) possessing an electronic system that is very sensitive to modifications of almost any kind and is responsible for their use in many technologically relevant applications.

Relevant and illustrative examples for the aforementioned conflict from the sectors of building, construction, and transportation are, e.g., technologies such as “smart windows” [13] and lithium-ion-batteries (LIBs) [14]. The former are capable of regulating the flow of electromagnetic radiation through glazing and are a very promising technology to reduce the contributions of temperature control inside buildings to their overall energy consumption and greenhouse gas emission [15–17]. The latter – probably more popular – example of the LIBs, for which John B. Goodenough, M. Stanley Whittingham and Akira Yoshino were awarded the Nobel prize in 2019 [18], gained increasingly more technological relevance due to their potential for replacing conventional combustion engines in vehicles and the predicted consequential reduction of greenhouse gas emissions [19]. Both technologies

experienced a pronounced increase in their market share [20, 21], are in the focus of current industrial research and development, and, to a certain extent, rely on the reversible insertion and extraction of charge carriers into TMOs. In both cases, specifications like coloration efficiency, bleached- and colored-state transmittance, response or switching time, and long-term durability (for “smart windows”), or cell and operating voltage, discharge capacity, energy density, power density and cycling stability (for both applications) are used to compare different concepts and the material performance on a device scale.

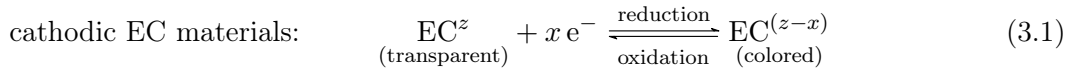
The insertion, extraction, and transport of different charge carriers determine the performance of these materials to a large extent but are in many cases not well understood, often due to experimental difficulties related to the individual characterization of single thin films in “smart windows” or especially single particles in composite electrodes of LIBs. Thus, providing experimental access to the characterization of charge transport and gaining deeper insights into well-known representative materials from both examples is an important contribution to the improvement of existing technologies and the development of new ones. The impact in a scientific and economic sense will be determined in the future.

3 Fundamentals

TMOs, as well as their applications, have been investigated intensively for several decades. However, still open research questions remain as the class of TMOs is so versatile. Hence, it is desirable to introduce the materials, important properties, and current state-of-the-art technologies based on these materials in order to provide an adequate scientific background to follow the ideas discussed in the publications and to be able to place them into an appropriate context.

3.1 Electrochromism and Electrochromic Materials

Electrochromism describes the ability of a material or material system to reversibly change its optical properties in the visible and near infrared range of the electromagnetic spectrum as a response to an applied bias that oxidizes or reduces an electroactive species [20, 22–24]. Based on this definition^a, electrochromism can be attributed to rather different processes involving either redox reactions of soluble species (type I, e.g. oxidation of dimethyl viologen dichloride in an aqueous potassium chloride solution [26]), redox reactions followed by the subsequent formation of an insoluble deposit on an electrode surface (type II, e.g. reduction of diheptyl viologen ions in the presence of bromine ions [27]) or the insertion/extraction of ions and electrons into particles or thin films representing an electrochemically active layer (type III, e.g. electrochemical reduction of a WO₃ thin films [28]). Independent of the number of components necessary to induce an electrochromic (EC) coloration or bleaching process, the terms “electrochromic material” or “EC material” are used here for the sake of convenience. A further classification of EC materials is often based on the reaction that triggers the coloration. While a cathodic EC material colors upon reduction of the electroactive species, the oxidation of an electroactive species initiates the coloration of anodic EC materials. This definition is represented by the corresponding reaction equations



in which an EC material EC^z, with *z* being an arbitrary oxidation number of the corresponding electroactive species, colors either upon reduction or oxidation [29]. To compare

^a The term “electrochromism” was originally introduced by John R. Platt to describe the response of organic dye-molecules in solution on the application of an electric field across the solvent, as shifts in absorption and emission spectra can arise due to electric-field induced switching between two resonance structures [25].

the performance and the applicability of different EC materials on a device level, different aspects and physical quantities describing an EC material system need to be addressed:

- The sensitivity of the human eye depends on the wavelength of the detected radiation and color impressions can vary considerably. To quantify the **color** of an EC material in a certain state, the CIE 1976 $L^*a^*b^*$ color space of the International Commission on Illumination (Commission internationale de l'éclairage, CIE) is often used [20].
- The **transmittance change** (sometimes also called “contrast” or “contrast ratio”) of an EC material achieved during coloration or bleaching $\Delta T(\lambda)$ is defined as the difference between the transmittance in the fully oxidized state $T_{\text{ox}}(\lambda)$ and fully reduced state $T_{\text{red}}(\lambda)$ according to

$$\Delta T(\lambda) := T_{\text{ox}}(\lambda) - T_{\text{red}}(\lambda). \quad (3.3)$$

Changes in the optical properties usually affect $\Delta T(\lambda)$ in an extended spectral range, which requires the specification of a wavelength or a spectral range over which the transmittance was integrated [30]. If electrochromic materials possess two states with two different colors, a more sophisticated comparison is necessary. In these cases, the so-called “photopic contrast”, taking the sensitivity of the human eye into account, is used [31]. The photopic contrast can be calculated by

$$\Delta T_{\text{photopic}} = \frac{\int_{\lambda_1}^{\lambda_2} \Delta T(\lambda) S(\lambda) P(\lambda) d\lambda}{\int_{\lambda_1}^{\lambda_2} S(\lambda) P(\lambda) d\lambda}, \quad (3.4)$$

where $\Delta T(\lambda)$, $S(\lambda)$, and $P(\lambda)$ are the difference between the spectral transmittance of the EC material in the oxidized and reduced state, the normalized spectral emittance of a 6000 K blackbody, and the normalized spectral response of the human eye, respectively.

- The time necessary to complete an optical transition between an oxidized and a reduced state, or a bleached and a colored state, is referred to as **switching time** or **response time**. In some cases a further differentiation is used to describe the time necessary for coloration (coloration time) or bleaching (bleaching time). An attempt has recently been made to establish a standard method for the determination of the switching time that is independent of the EC material and can also be applied to the transmittance change of EC devices [32]. This attempt is motivated by the observation that the transmittance change $\Delta T(\lambda, t)$ of different EC materials can be adequately described by

$$\Delta T(\lambda, t) = \Delta T_{\text{max}}(\lambda) \left(1 - e^{-\frac{t}{\tau}} \right), \quad (3.5)$$

if square-wave potential steps with varying pulse length t are used to induce an optical transition. The time constant τ is then equal to the pulse length t_{63} of a square-wave potential step that is required to obtain a transmittance change of 63 % of the maximum transmission change $\Delta T_{\max}(\lambda)$ observed at large pulse lengths [32]. However, influences of EC thin film degradation or the applied potentials on the parameters $\Delta T_{\max}(\lambda)$ and τ will still have to be taken into account.

- A quantity relating the changes of the absorbance^a $\Delta A_{10}(\lambda)$ with the electric charge per area necessary to induce these optical changes Q_A is the EC **coloration efficiency** $\eta_{\text{EC}}(\lambda)$. The EC coloration efficiency $\eta_{\text{EC}}(\lambda)$ is usually given in $\text{cm}^2 \text{C}^{-1}$ at a certain wavelength and is defined as

$$\eta_{\text{CE}}(\lambda) := \frac{\Delta A_{10}(\lambda)}{Q_A} = \frac{(A_{10,\text{red}}(\lambda) - A_{10,\text{ox}}(\lambda))}{Q_A} = \frac{\log_{10} \left(\frac{T_{\text{ox}}(\lambda)}{T_{\text{red}}(\lambda)} \right)}{Q_A} \quad (3.6)$$

where $T_{\text{ox}}(\lambda)$ and $T_{\text{red}}(\lambda)$ denote the transmittance in the oxidized and reduced state, respectively [29, 34–39]. According to this definition the sign of the coloration efficiency of cathodic and anodic EC materials should differ, but in most cases absolute values are reported.

- The changes in the optical properties of EC materials are induced by an applied voltage. If the electrochemically reduced or oxidized species are stable enough, the voltage can be removed and the EC material will stay in its redox state for a certain time. Such EC materials exhibit a high **optical memory** when the device is taken to open circuit and can be used in EC devices without a continuous power supply [20, 40].
- Strongly depending on the desired application, the **reversibility** of an EC process is an important aspect to consider. While long-term degradation of EC materials leads to decrease of the transmission change and thus limits their operational lifetime [41–45], an irreversible EC process is required for the application of EC materials in so-called “smart labels”. These labels will change color or become visible if, e.g., the temperature of a pharmaceutical/medical product exceeds a certain limit during storage or inappropriate handling of a parcel containing sensitive materials leads to damage of the contents [35].

^a The coloration efficiency is in many cases defined using the term “optical density”. The usage of this term is discouraged and the term “absorbance” should be used instead [33].

Further aspects like industrial scalability, economic concerns, sustainability of the entire production chain, and recyclability gain increasing importance for device manufacturing and are also addressed in the literature [46–48].

Many different materials, e.g., metal coordination complexes, organic molecular dyes, conducting polymers, and TMOs, exhibit EC properties. This inherently leads to a wide range of applications and devices relying on the EC properties of these materials. Windows that can be reversibly switched between an opaque and a transparent state (“smart windows”), combinations of “smart windows” with photovoltaics or solar cells; cheap and printable EC labels; rear-view-mirrors, which are capable of reducing the glare caused by other cars; EC displays; lenses; sunglasses; or “smart” textiles, generally called “EC devices”, rely on these materials. An overview of EC devices as well as references containing more detailed information can be found in the literature [20]. Depending on the requirements an EC device needs to meet, the range of suitable EC materials is limited. For example, organic EC materials exhibit many advantageous properties compared to inorganic ones like low-cost processability, larger optical contrast, shorter switching times and a wider range of colors. However, inorganic EC materials outperform most organic ones in terms of chemical, electrochemical, photochemical, environmental and thermal stability [20, 49] allowing operational lifetimes of up to 10^6 cycles of coloration and bleaching [35, 50] with acceptable decreases in the transmission change. This is one of the major reasons for today’s dominance of TMO thin films in “smart windows” [20].

In principle, a “smart window” consists of several glass panes. The volume between two panes, which is created by a spacer, is sealed at its boundaries inside the window frame and can either be filled with air or other gases to enhance thermal insulation [51]. Typically, one surface of the glass panes facing the inside of the window is equipped with a series of thin layers that make up the EC component of a “smart window” as depicted in figure 3.1. The EC component is protected by another pane of glass or alternatively by other means like a polymer foil, increasing long-term stability. Thin films of a transparent electron conducting material make up the outer layers of the EC device and enable electrical contacting. Depending on the design, one EC thin film and an ion storage layer or two EC thin films of opposite coloration behavior (see equations 3.1 and 3.2.) are connected to the transparent conductors and separated by a purely ion conducting layer. The latter can be a material such as a ceramic oxide [44, 52, 53] like Ta_2O_5 , a polymer electrolyte based on vinyl polymers [54], or a liquid electrolyte like lithium perchlorate (LiClO_4) in propylene carbonate (4-methyl-1,3-dioxolan-2-one, PC) [55].

If a voltage is applied between the transparent conducting layers, electrons and ions will be inserted into or extracted from the EC layer, triggering redox reactions involving the electroactive species in the EC layer and a color change of the window. By this the transmittance of electromagnetic radiation can be regulated.

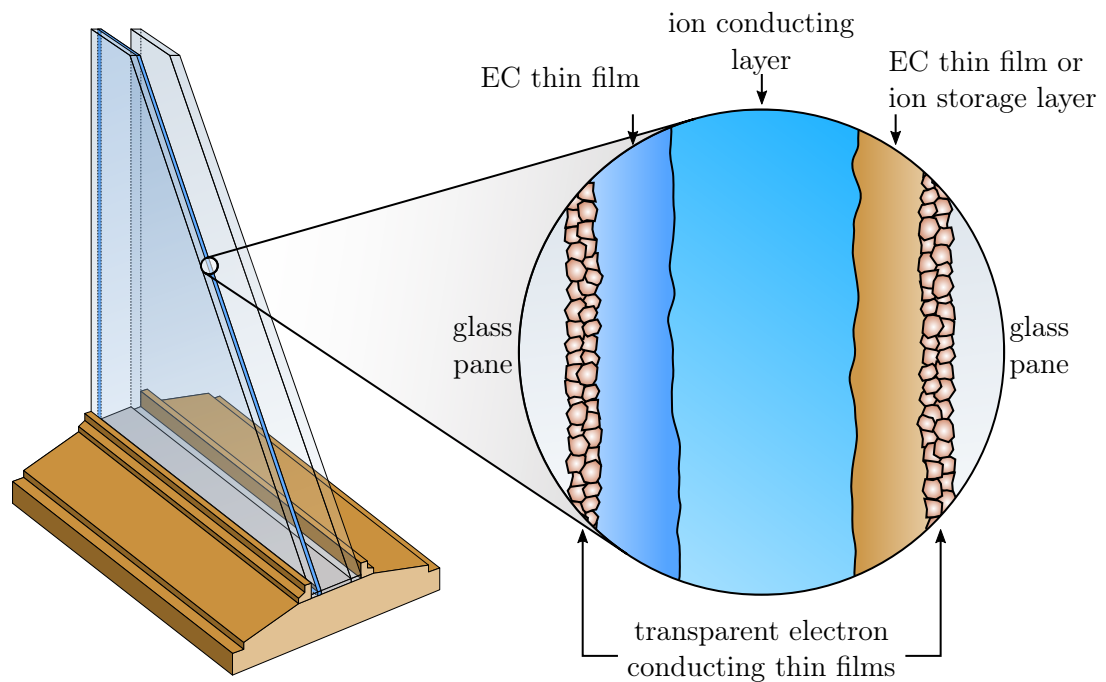


Figure 3.1: Schematic representation of a “smart window” with an EC component between two glass panes (left, adapted from [15] and [44] with permission from Elsevier) and a cross-section of the EC component (right) comprising transparent electron conducting thin films, an EC thin film and an ion storage layer or a second EC thin film, as well as an ion conducting layer between them.

The cathodic EC material that is most frequently used in today’s “smart windows” is a WO_3 thin film^a. The description of a bluish tungsten oxide compound was first reported in 1816 [56]. Changes of the optical properties of WO_3 upon reduction have also been known since 1930, when this effect was used to detect atomic hydrogen [57]. The first known experiments on WO_3 thin films in an electrochemical cell date back to 1953 [22], but it took until 1969 to become public. In this year Satyen K. Deb published his findings in a report [58], which is often referred to as the beginning of research on electrochromic WO_3 thin films. Today, WO_3 is one of the most intensively studied EC materials and often regarded as a model system for investigations, although details on certain properties are still under debate. A better understanding of these details will lead to better devices in the future and should enable widespread application.

3.2 Properties of WO_3 Thin Films

The crystal structure of WO_3 consists of corner-sharing WO_6 octahedra and is often described as a defect perovskite, due to its similarities to the structure of the original perovskite with the general composition ABO_3 . By conceptually removing the cation A^{2+} from the corners of the perovskite unit cell, the unit cell of a BO_3 defect perovskite is

^a According to a statement of Prof. Dr. Claes G. Granqvist, Head of the Ångström Laboratory, Uppsala University, on August 28th, 2019, 11:09 am.

obtained. The crystal lattice built-up from such a unit cell is a network of BO_6 octahedra that is similar to the cubic crystal structure of ReO_3 [59] and provides a three dimensional network of vacancies at the corners of the BO_3 unit cells. Figure 3.2 illustrates the correlation between the structures of a perovskite, a defect perovskite and the network of BO_6 octahedra.

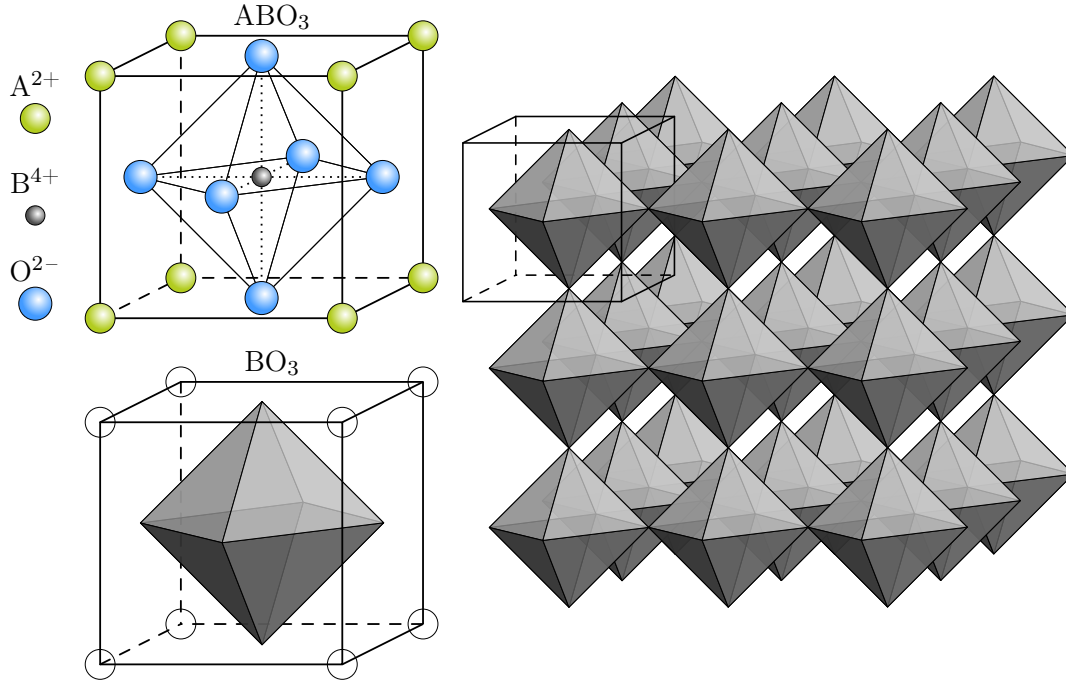


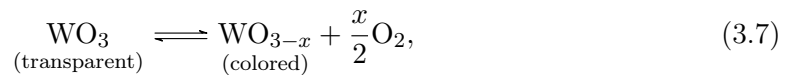
Figure 3.2: Images of the unit cells of a perovskite with the composition ABO_3 (top left), a defect perovskite with the composition BO_3 (bottom left), and a $3 \times 3 \times 3$ supercell built-up from the unit cell of a defect perovskite (right). The representation of the defect perovskite unit cell is reduced to a BO_6 octahedron; O^{2-} ions at the corners, as well as a B^{6+} ion in the center are omitted. The open circles at the corners of the unit cell indicate vacancies, which are occupied by A^{2+} ions in the perovskite structure. This crystal lattice is a regular network of ideal BO_6 octahedra with open channels in all three dimensions.

The open structure of a defect perovskite provides channels and transport pathways for interstitial ions, which is advantageous for the reversible insertion and extraction of small ions like H^+ and Li^+ . The network of octahedra described is sensitive to changes in the temperature or the degree of protonation/lithiation and can adopt several crystal structures.

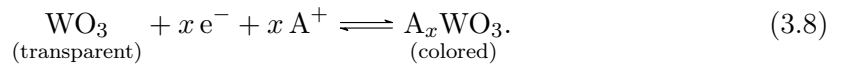
The structural properties of WO_3 are caused by certain types of interactions between W^{6+} and O^{2-} ions. Probably due to the structural similarities, the binding properties in WO_3 are often explained in reference to those found in the cubic structure of ReO_3 [60–63]. A drawback of this approximation is a limited extent to which the description of cubic WO_3 can be used to explain experimental observations involving other crystal structures of WO_3 ; for example, it underestimates the band gap [64]. The electronic configurations of tungsten and oxygen are $[\text{Xe}]4f^{14}5d^46s^2$ and $1s^22s^22p^4$, respectively. In a simplified view of purely ionic bonds between W^{6+} ions and O^{2-} ions, six electrons originating from W 6s

and W 5d orbitals fill the O 2p states of three oxygen atoms completely, resulting in W⁶⁺ and three O²⁻ ions. The Madelung potential and the electrostatic splitting cause a shift of the ionic states and lead to splitting of the W 5d and the O 2p states. The energetic states determining the band structure of WO₃ are one filled O 2p_{||}, two filled O 2p_⊥, three empty W 5d_{t_{2g}}, and two empty W 5d_{e_g} states. The resulting electronic band structure comprises a filled O 2p valence band, an empty W 5d conduction band separated by a band gap, which makes WO₃ a semiconductor. Reported experimental values for the band gap energy of WO₃ are 3.52 eV [65] for a direct band gap, and vary between 2.59 eV, and 2.79 eV for an indirect band gap [65–68]. More detailed descriptions of the electronic structure, based on molecular orbital theory, suggest that components of W 5d and O 2p orbitals are present in both electronic bands due to hybridization and covalent mixing of O 2p and W 5d states [62, 63, 69].

Changes in the electronic structure of WO₃ have a strong impact on the structural properties [63, 70–72] and may induce phase transitions. While a certain consensus on this correlation exists, explanations differ and are based on increasing covalent interactions between W 5d and O 2p orbitals [70], decreasing W–O bonding strength [71], or a lowering of the conduction band [72]. In general, the electronic and optical properties of TMO d-band perovskites are mostly determined by the binding properties between the transition metal and octahedrally coordinated oxygen ions. The contributions of an additional cation, as found in the regular perovskite structure, are often neglected, although the electrostatic potentials of such a cation may have a strong influence on the energy of the valence and conduction band [73]. This approximation is also called “rigid band” approximation and refers to the rigidity of the band structure of ionic perovskites with a comparably large band gap like SrTiO₃ [74]. However, an external stimulus that causes the filling of the W 5d band can lead to changes in the crystal structure of the material. Stimuli that induce such an n-doping of WO₃ could be, e.g., the incorporation of oxygen vacancies V_O^{••} [75, 76] according to



or the insertion of small ions A⁺ and charge compensating electrons by electrochemical means [77, 78]. The latter is often represented by the reaction



which, according to the definition in reaction equation 3.1, makes WO₃ a cathodic EC material that is colored upon reduction. This macroscopic picture is sufficiently accurate for studies aiming at empirical optimization for specific applications. However, even though the changes in the optical properties are similar [75], the processes taking place upon oxygen vacancy formation and cation insertion have different impacts on the electronic conductivity of the material and lead to structural changes [79]. Several other phases like WO₂ and so-called Magnéli phases with the overall composition W_mO_{3m-1} and W_mO_{3m-2}

($m = 1, 2, \dots$) are known to form upon the formation of oxygen vacancies and shear dislocations as x in WO_{3-x} exceeds 10^{-4} [80]. This aspect becomes even more obvious from the W-O phase diagram depicted in figure 3.3 [81]. The assignment of Greek letters α , β , and γ indicates changes in the crystal structure of WO_3 in accordance with figure 3.4.

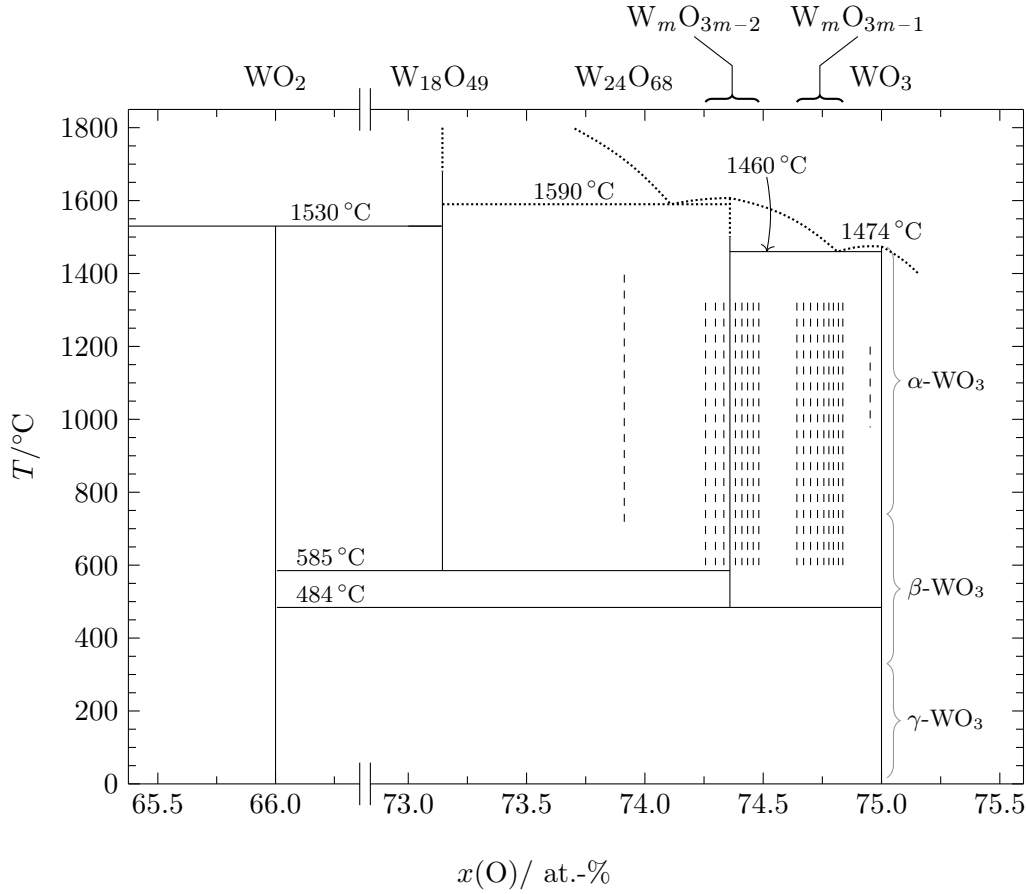


Figure 3.3: Phase diagram of tungsten and oxygen (W_{1-x}O_x) at 1 bar with dotted lines added speculatively (adapted by permission from Springer Nature Customer Service GmbH: Springer Nature, Bulletin of Alloy and Phase Diagrams, “The O-W (Oxygen-Tungsten) System”, H. A. Wriedt © 1989 [81]).

The structural transitions that occur when small ions are inserted are similar to those that have been studied intensively in the past as a function of temperature, which are used here to illustrate the correlation between the different structures. While WO_3 exhibits a monoclinic (Pc between 15 K and 220 K) [82, 83] or a triclinic phase ($P\bar{1}$ (C_i^1) between 220 K and 290 K) [84–87] below room temperature, it crystallizes in a monoclinic (often also referred to pseudoorthorhombic) phase ($P2_1/n$) at temperatures above 290 K [85, 88–93]. This modification shows a deviation of the unit cell angle β from 90° by about 1%, which is caused by distortions, rotations, and inclinations of the WO_6 octahedra accompanied by off-centering of W^{6+} ions. At elevated temperatures, this monoclinic phase transforms into an orthorhombic phase [92, 94] ($Pbcn$ between 623 K and 1073 K [95], $Pmnb$ between 740 K and 973 K [96]), which shows two additional structural transitions upon further increasing temperature into tetragonal phases [92, 94] ($P4/ncc$ at 1073 K, $P4/nmm$ above 1171 K) [95, 97–99]. Although a cubic WO_3 structure was predicted to be energetically

less favorable than distorted networks of octahedra unless electrons in the conduction band stabilize the cubic structure [63], the preparation of a cubic WO₃ phase has been reported [100–102]. In terms of the network of WO₆ octahedra, the different crystal structures of WO₃ mainly differ in the tilting of the octahedra along different crystallographic axes. A notation introduced by Glazer to classify systems containing tilted octahedra can be applied to describe the different crystal structures [103]. In the so-called Glazer notation, the three letters a , b , and c denote the crystallographic directions [100], [010], and [001] around which tilting occurs. If the tilting around two different directions is equal, the same letter is used in some cases. To indicate in-phase, out-of-phase or no tilting of several layers of octahedra along a certain direction, +, −, or 0 are added as superscript to the corresponding letter. Figure 3.4 depicts the different crystal structures of WO₃ upon increasing temperature, the temperature ranges in which they are observed, and the corresponding Glazer notation [104].

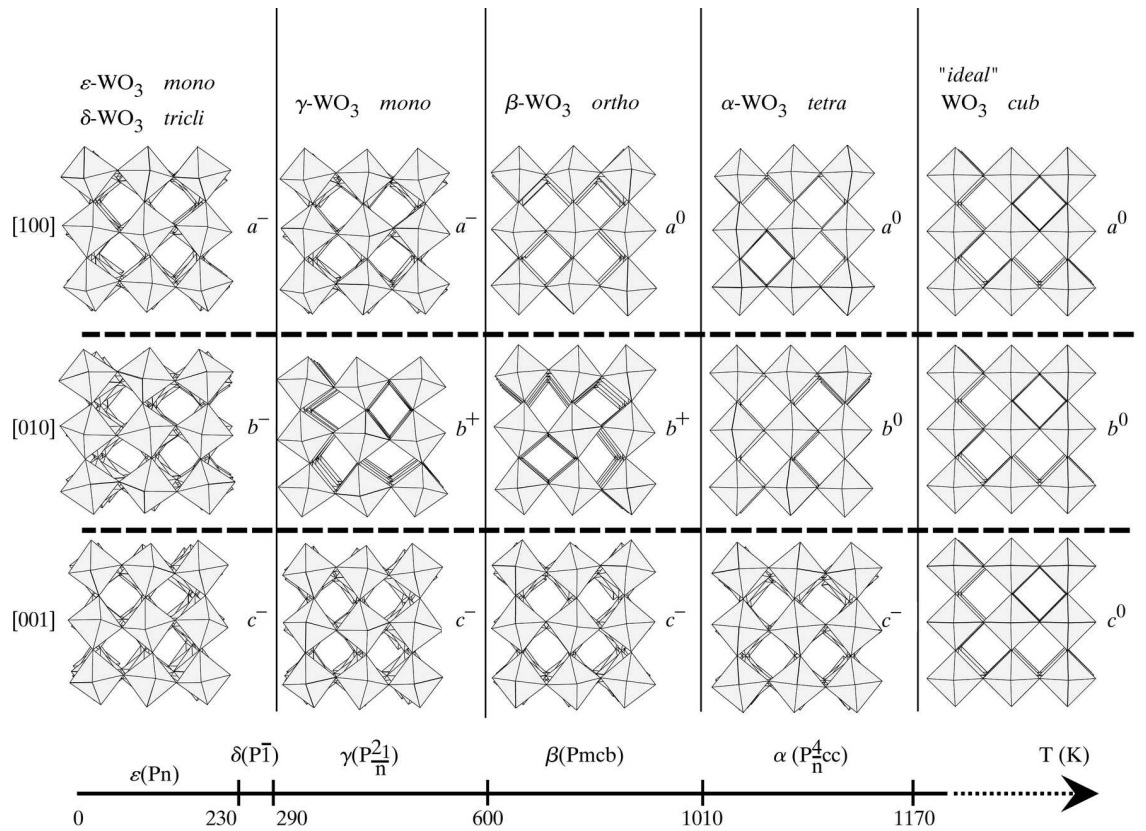


Figure 3.4: Crystal structures of WO₃ at different temperatures shown along different crystallographic directions. The tilting of the octahedra is classified according to the Glazer notation, where in-phase, out-of-phase, and no tilting are indicated by +, −, and 0. Reproduced with permission of the International Union of Crystallography (<https://journals.iucr.org/>) [104].

Starting with the monoclinic room temperature phase of WO₃, a similar sequence of phase transitions is reported upon protonation or lithiation, which lead to the formation of an orthorhombic phase (H_{0.1}WO₃), tetragonal phases (H_{0.23±0.02}WO₃, H_{0.33}WO₃, Li_{0.1}WO₃) and cubic phases (H_{0.5}WO₃, Li_{0.36}WO₃) [105–108]. The sequence of phase transitions upon protonation of WO₃ was studied using WO₃ powders, but it is also generally expected to

occur during the electrochemical coloration of polycrystalline WO_3 thin films with hydrogen [109]. However, the structural properties of thin films might, of course, be altered due to a potential lattice mismatch between the WO_3 thin film and the substrate employed.

In view of the considerable importance of amorphous WO_3 thin films for EC devices, which show higher coloration efficiencies and a larger number of coloration and bleaching cycles without deterioration [110], the corresponding structural features are worth mentioning. Here, the term “amorphous” refers to a crystal lattice, in which structural elements exhibit local ordering only. Amorphous WO_3 solids and thin films are therefore disordered on scales exceeding a few nanometers. This absence of long-range ordering of structural elements in the crystal structure prevents constructive interference of incident and diffracted X-rays to occur at defined angles. Thus, X-ray diffraction patterns of amorphous thin films generally show broad characteristics rather than sharp reflections. However, the structure of amorphous WO_3 thin films is still regarded to be composed of corner-linked octahedra, albeit in a disordered manner manifested by statistical variations of the bond lengths and angles [111]. Structural changes in amorphous WO_3 films induced by continuous insertion and extraction of small ions involve the growth of crystalline domains in the thin film [112]. This Ostwald ripening-like growth of larger grains at the expense of smaller grains was also observed after several insertion and extraction cycles of Li^+ ions into nanocrystalline WO_3 thin layers [113].

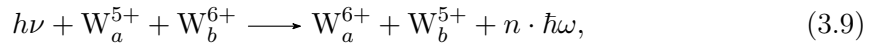
3.2.1 Electrochromic Coloration in WO_3

As already indicated in equation 3.8, the insertion of small ions into WO_3 thin films not only induces structural changes in WO_3 thin films as charge compensating electrons are added to the electronic structure simultaneously. This in turn also affects other properties like optical or electrical properties and, therefore, also electrochemical properties, which themselves are further influenced by the thin film morphology [114–117]. Thus, the plethora of experimental results on properties of WO_3 concerning the EC coloration and bleaching processes is mainly due to the countless possible combinations of thin film properties, thin film characterization techniques, and experimental methods capable of investigating the changes during EC coloration and bleaching. An attempt to give an overview of the experimental and theoretical results of WO_3 , which would do the amount of results justice is beyond the scope of this thesis, but can be found in the literature [22, 24, 29, 111]. A brief summary of the mechanisms developed and proposed to describe the optical properties of WO_3 thin films upon the insertion of small ions is given here without explicitly assessing their ranges of applicability and validity:

Color Centers, Intervalence Charge Transfer, Polaronic Transitions

One of the first proposed explanations for the coloration of WO_3 thin films, i.e., the absorption of radiation with energies below the band gap, refers to **color centers**, similar to *F*-centers, which are a specific type of color center and known to be responsible for colors in ionic solids [118, 119]. Further specifying the nature of these color centers, excited

electrons captured by positively charged structural defects need to be mentioned [120]. A model, which is also related to this certain type of color center, but employs another description, is the absorption due to **intervalence charge transfer** (IVCT). According to this model, the double injection of electrons and A⁺ ions leads to the formation of A_xWO₃. Additional electrons are localized on a lattice site of a W⁶⁺ ion and reduce it to a W⁵⁺ ion. Analogue to other systems with transition metal ions of mixed valences like, e.g., “Prussian Blue”, absorption takes place, if the energy of an incident photon is large enough to excite an electron from a W⁵⁺ ground state into an excited state of an adjacent W⁶⁺ ion, where it thermalizes via emission of n phonons and reduces the adjacent W⁶⁺ ion to a W⁵⁺ ion [117, 121–123]. This process is often illustrated by



where the subscripts a and b are used to indicate two different lattice sites and $h\nu$ and $\hbar\omega$ represent the energies of an incident photon and emitted phonons, respectively. The essential aspect of non-radiative thermalization via phonon emission and thus the term $n \cdot \hbar\omega$ in equation 3.9 is often neglected in the literature. Due to experimental findings on the influence of oxygen deficiency on EC coloration of WO₃ thin films, similar transitions involving W⁵⁺ and W⁴⁺ states, which differ in their contribution to optical absorption, as well as site saturation effects have also been considered [113, 124–131].

Addressing the origin of the localization of an electron at a tungsten site, the formation of **small polarons** due to the interactions between electrons and LO phonons in WO₃ was proposed [132, 133]. A polaron is a quasi particle describing an electron in a polar crystal, which polarizes and distorts its surrounding ionic lattice in a way that this polarization lowers the energy of the electron. In this way a potential well is created, in which the electron is stabilized and localized. The term “small polaron” refers to a situation in which the dimension of the polaron is smaller than the lattice constant of the crystal lattice [134–138] and their impact on different properties has been described by several authors [139–141]. Interpretations of experimental results according to large polaron theory have also been reported [142]

Intra- and Interband Absorption

The successful description of the optical absorption spectrum of colored WO₃ thin films in terms of **intraband absorption** in disordered systems with a strong electron-phonon interaction [143] was demonstrated several times [123, 128, 130, 131]. This model assumes that the Fermi energy lies in a band of localized states and close to the top of the density of states of this band. Thus, optical absorption arises from the excitation of electrons near the Fermi level into empty states of the same band [143]. Such an intraband transition was also proposed in a slightly different form, mainly differing in the aspect that excitation of electrons from states at the bottom of the conduction band into empty states of the same band was considered [144]. Besides transitions between similar states of different tungsten

ions via IVCT, transitions between different bands have also been considered as a possible explanation for absorption. Such an **interband charge transfer** absorption process could take place by exciting electrons from the partially filled π^* band to energetically higher σ^* bands [122], or from the conduction band into a band of states of the inserted cation [145, 146]. Depending on the energetic position of the aforementioned reduced states of tungsten relative to the valence and conduction bands, an absorption process due to the excitation of electrons from the valence band into an impurity band of reduced tungsten states [122], or from such an impurity band into the conduction band [75, 138, 147] was proposed.

Drude-like Reflectance and Absorption

While a certain overlap between metal ions and localization of electrons is necessary to explain absorption by IVCT, the collective movement of delocalized electrons induced by electromagnetic radiation gives rise to **free-carrier absorption** and **plasma resonance reflection**. The characteristic quantity describing the frequency of longitudinal eigenoscillations of free charge carriers is the plasmon (also plasma cut-off) frequency ω_p . It is given by

$$\omega_p = e_0 \sqrt{\frac{c_n}{m^* \varepsilon_0 \varepsilon_r}} \quad (3.10)$$

where c_n is the concentration of free electrons, m^* is the electron effective mass, ε_0 is the vacuum permittivity, and ε_r is the dielectric constant of the solid under investigation in the absence of free charge carriers. From equation 3.10 the effect of n-doping and a corresponding increase of the concentration of free electrons c_n becomes obvious: the plasma resonance may shift into the visible range of the electromagnetic spectrum and restrict the transmittance of the solid toward smaller wavelengths [122, 148–151]. While this model neglects any influence of the small cation inserted, the impact of scattering at ionized impurities was also discussed [152], as was the description of the optical properties of WO_3 in terms of the dielectric function of a single oscillator [153, 154].

However, the details of the absorption mechanisms of amorphous, partially crystallized, and (poly-)crystalline WO_3 thin films and the differences between them are presently not entirely understood. The situation is very complex due to many-body interactions like, e.g., electron-ion or electron-electron interaction as is also observed in other semiconducting materials [155–158], band gap shifts [159] probably due to the Burstein-Moss effect [160–162], or electron-phonon interactions [111]. Also defect agglomeration, differences between n-doping by oxygen vacancies and by small ions, as well as inactive states of the inserted ion have been reported [116, 163, 164]. Especially investigations of different energetic states in transparent and colored WO_3 thin films by (X-ray) photoelectron spectroscopy contributed to the development of the described models. This method might be limited to electronic states at the surface of the films, since preferential sputtering and the formation of oxygen vacancies complicates depth profiling [165]. The impact of such effects on optical, electronic and electrochemical properties is still the subject of current research

[166]. It is further complicated by the above-mentioned interrelationships between the film preparation technique, the exact composition including incorporated H₂O and oxygen vacancies, and morphological properties, like, e.g., porosity, specific surface area or grains and grain boundaries.

3.2.2 Charge Transport and Diffusion in WO₃

The large variety of more or less appropriate descriptions of the EC coloration of WO₃ thin films upon insertion of small ions also affects the interpretation of results gathered by various experimental techniques. The most relevant techniques for studying charge storage and charge transport are from the fields of solid state physics and electrochemistry.

The simultaneous insertion of electrons and small ions into WO₃ thin films advocates the description of charge transport in WO₃ in terms of a mixed conductor with partly ionic and partly electronic conduction. In such a mixed ion-electron conductor (MIEC), charge is transported through the movement of mobile ionic and electronic charge carriers. Although, both types of charge carriers are often regarded to move independently from each other, this assumption does not hold in general. The origin of this correlation is described by the following scenario:

The interaction between a moving ionic charge carrier and electronic charge carriers exerts a force on electronic charge carriers capable of accelerating them towards the direction of the moving ionic charge carrier. The ionic charge carrier effectively drags electronic charge carriers along with it and induces an electronic current in the absence of an potential gradient. This dragging of electronic charge carriers effectively changes the valence of the ionic charge carrier [167]. The same consideration can be applied vice versa. Related to this, an electrochemical potential gradient across a MIEC accelerates both types of charge carriers, which in general have different mobilities. This would lead to the formation of an opposed electrochemical potential gradient due to different concentration gradients of both charge carriers, which in turn would accelerate the less mobile species and slow down the more mobile ones until a balanced flux of both charge carriers is created [168]. The coupled diffusion of an ionic defect k with a partial ionic conductivity σ_k and electronic charge carriers with an effective electronic conductivity $\tilde{\sigma}_e$ can be described by an effective coupled chemical diffusion coefficient (CCDC) $\tilde{D}_{k,e}$ as

$$\tilde{D}_{k,e} = \frac{\sigma_k \tilde{\sigma}_e}{q_k^2 (\sigma_k + \tilde{\sigma}_e)} \frac{d\mu_{A_k}}{dc_k}, \quad (3.11)$$

where q_k is the effective charge of the mobile ionic defect, μ_{A_k} is the chemical potential of the neutral component formed by the ionic defect and electronic charge carriers and c_k is the concentration of the ionic defect [168, 169]. Taking the Nernst-Einstein equation into account, either in its pristine form or as a variation, corrected for the interaction between ionic and electronic charge transport [167], a linear correlation between the conductivity

and the diffusion coefficient of a certain species is established from which

$$\tilde{D}_{k,e} \propto \frac{D_k \tilde{D}_e}{D_k + \tilde{D}_e} \quad (3.12)$$

follows. From equations 3.11 and 3.12 it can be seen that the charge carrier with the lowest conductivity or diffusivity determines the CCDC.

Experimental results on charge transport, i.e. the transport of ions and electrons in WO_3 thin films decidedly demonstrate the higher mobility of electrons compared to protons or lithium ions. The electronic conductivity of WO_3 thin film varies from $10^{-6} \text{ S cm}^{-1}$ to 10^2 S cm^{-1} upon coloration [122] and the diffusion coefficient of electrons in WO_3 was determined to vary between $1.26 \cdot 10^{-3} \text{ cm}^2 \text{ s}^{-1}$ and $5.05 \cdot 10^{-3} \text{ cm}^2 \text{ s}^{-1}$ [170, 171]. By contrast, the diffusion coefficients of technologically more relevant Li^+ ions are reported to vary between $10^{-9} \text{ cm}^2 \text{ s}^{-1}$ and $10^{-13} \text{ cm}^2 \text{ s}^{-1}$ depending on many factors like, e.g., the lithium content in Li_xWO_3 [172–177], the thin film porosity [173, 178], its composition [173, 179] as well as the degree of crystallinity [177]. Reports on the influence of the water content of the electrolyte [180], the electrolyte itself [181], the applied potential used for electrochemical insertion of Li^+ ions [179, 182] and the water content of the environment [173] on the diffusion of Li^+ ions in WO_3 thin films indicate the difficulties in studying and interpreting experimental results on diffusion. An observation that is comparably often described qualitatively is the dependence of the diffusion coefficient on the concentration of the Li^+ ions. However, a uniform description of the relationship between diffusion and the concentration of Li^+ ions has not yet been achieved [172–175, 177, 178, 183–186]. This might also be caused by the experiments being very sensitive to many often unknown structural quantities, which may affect the outcome significantly. A similar impression of the complexity of diffusion processes can be obtained by surveying the literature on diffusion of protons instead of Li^+ ions in WO_3 thin films (see discussion and references in publication 1 of this thesis), with proton diffusion coefficients being approximately one order of magnitude larger.

The experimental methods used for investigating diffusion processes are in most cases electrochemical techniques such as electrochemical impedance spectroscopy (EIS), the galvanostatic intermittent titration technique (GITT) or chronoamperometry, and cyclic voltammetry. Of the other less frequently described approaches the application of the trap-release-followed-by-diffusion-and-migration (TRDM) method is also noteworthy [182]. Most of the electrochemical experiments performed are comparably close to the working principle of EC thin films in an EC device. This means they use electrochemical cell configurations including a liquid electrolyte, a counter electrode and a reference electrode to investigate the properties of a WO_3 thin film. The latter is used as or as a part of the working electrode. By this, the direct assessment of the EC performance of a certain WO_3 thin film in a device is possible, which probably motivated many studies of electrochemical properties of WO_3 thin films. Important insights obtained from such experiments are differences in the kinetics of H^+ and Li^+ or Na^+ ion insertion, which can lead to high

ion concentrations at the electrode-electrolyte interface and differences in the number of irreversible side reactions [184]. The combination of in situ transmission measurements during ion insertion and ex situ XPS studies revealed differences in the absorbance change upon ion insertion depending on the electrode potential and the oxidation state of tungsten ions in nanocrystalline WO₃ thin films [113]. The formation of W⁵⁺ states at a potential of -0.05 V (vs. $E_{\text{Ag}/\text{AgCl}}$) and W⁴⁺ states at -0.3 V (vs. $E_{\text{Ag}/\text{AgCl}}$) yields three possible transitions $\text{W}^{6+} \rightarrow \text{W}^{5+}$, $\text{W}^{5+} \rightarrow \text{W}^{4+}$, and $\text{W}^{6+} \rightarrow \text{W}^{4+}$, which contribute differently to the overall EC coloration [113]. Also trapping of Li⁺ ions in WO₃ films was observed recently upon ion insertion and extraction [187–191], which in fact can influence results from electrochemical measurements remarkably. However, no matter if the current or the cell voltage of an electrochemical cell is measured in such an experiment, the measured signal will display the response of a full electrochemical cell rather than the response of the WO₃ thin film only. A major part of the quantitative analysis of results from these experiments is based on assumptions, e.g., that the insertion kinetics of ions across the electrolyte-electrode-interface or the transport of ions through the electrolyte are not rate-limiting; that the diffusion coefficient of a species does not depend on its concentration; or that side reactions and parasitic currents are negligible, i.e., that the flowing charge is a direct measure for the concentration of a certain species in the thin film. Making such assumptions is necessary for the quantitative evaluation of experimental results by means of analytical expressions.

In most cases, the derivation of such expressions involves the solution of Fick’s second law or related partial differential equations in combination with expressions for the flowing current across the electrolyte-electrode-interface like, e.g., the Butler-Volmer equation [192]. Whether analytical solutions for appropriate equations and boundary conditions can be obtained or not, strongly depends on the degree of simplification, even if the diffusion coefficient is assumed to be independent of the concentration of the mobile species. While the latter has been shown to affect the ionic diffusion coefficient, most of the frequently used equations cannot be expected to hold for extended ranges of concentration of a certain species. Especially not if the kinetics of the electrochemical ion insertion or extraction proceed on a time scale comparable to that of the diffusion process of interest. The reports on influences of the cell configuration on the diffusion of inserted ions demonstrate that the obtained diffusion coefficients are to be understood as effective (albeit technologically probably more relevant) diffusion coefficients and not as a CCDCs in their proper sense. This distinction between an effective and a CCDC might in fact be important to consider in order to understand the broad range of reports and results on “diffusion” in WO₃.

A correlation of both diffusion coefficients can hardly be achieved, since the extent to which the CCDC is superimposed by other effects is barely known. Reports on diffusion coefficients in WO₃ derived by non-electrochemical methods are surprisingly rare. Even though such results are crucial in understanding how large possible deviations between both diffusion coefficients might be; which effects limit the observed processes in electrochemical experiments; or if the interpretation of results from the latter needs to account

for additional effects. The answers to these questions are likely to depend on the thin film morphology, whose effects on electrochromism in WO_3 are still not well understood. It is very desirable, to characterize the diffusion processes of ions in WO_3 thin films by means of experimental methods different from electrochemical techniques.

3.3 Electrochemical Energy Storage and Lithium-Ion Batteries

The vast field of electrochemical storage systems, in general, addresses today's need for storing and providing energy in all sorts of different situations and time scales. As a consequence the requirements may vary significantly. In all storage systems charge carriers have to be separated, transported (which enables the use of electric energy) and combined again. The way, in which charge carriers are stored distinguishes batteries from, e.g. fuel cells or supercapacitors, as charge is stored within the electrodes in case of batteries. The usage of the electric energy stored in the electrodes requires the separation of ionic and electronic currents. These electrodes are ideally connected to each other by a solely ion conducting, i.e., electronically insulating pathway through an electrolyte, and a solely electron conducting, i.e. ionically insulating pathway through the current collectors and wiring in an electric circuit. The choice of the different components determines, which electrochemical reactions take place at the electrodes and, therefore, define the specific energy and the specific power of the battery [193].

One way of classifying batteries is based on the reversibility of the electrochemical reactions taking place upon discharging the battery, which determines, if the battery system can be recharged or not. While primary systems cannot be recharged in a sufficiently efficient way and only to a very limited extent, secondary systems can be recharged. Despite their limited rechargeability, primary systems relying on the dissolution of metal anodes are used in hearing aids, cameras, watches, and other devices [194]. In order to compare battery systems, which rely on very different electrochemical reactions and processes, specifications are used, of which some are described:

- In order to compare the amount of charge that can be withdrawn from different systems under specified discharge conditions, it is frequently related to the mass of either the complete cell, one electrochemically active material or all the electronically active materials in both electrodes, which gives the **specific charge** q . The mass to which "specific" quantities are related to is very important to consider, since a battery requires parts, which do not participate in electrochemical redox reactions (electrochemically inactive parts) and therefore reduce the theoretical specific quantity inherently.
- The **cell voltage** is the potential difference between both current collectors of a battery. It is determined by both, thermodynamic and kinetic boundary conditions. These are given for a certain electrode material and for certain electrochemical reactions, which take place in a possibly competing manner. Depending on whether a

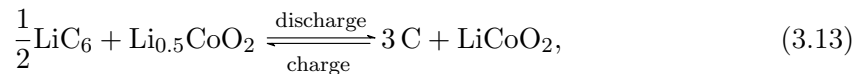
battery voltage is given under load or not, it is referred to as terminal voltage and open-circuit voltage, respectively.

- The “**state-of-charge**” (SOC) relates a certain charge, which is still provided by a battery to the specific charge of the battery and given in percent. Related to that is the “**depth of discharge**” (DOD), which relates the withdrawn charge to the specific charge.
- The **charge/discharge current** is the current, which is used to charge/discharge a battery. It is often given in terms of a “C-rate”, which relates the current to the specific charge of the battery. A 1C rate for instance describes a current, which is capable of completely charging/discharging a battery within one hour. A fivefold increase of the current, i.e. a 5C rate will charge/discharge the battery in 12 min.
- The term **specific energy** w refers to the total electrical energy, which can be obtained by discharging a battery divided by a meaningful mass. A frequently used unit for the specific energy is W h kg^{-1} [195]. Specific energies vary considerably among the different battery systems from the lead acid battery with 30 W h kg^{-1} , the nickel-metal hydride system with 95 W h kg^{-1} , and the LIB with up to 250 W h kg^{-1} to, e.g., primary lithium-metal batteries with a MnO_2 positive electrode and a specific energy of about 330 W h kg^{-1} or the zinc-air cell with more than 450 W h kg^{-1} [194, 196].
- Analogous, the **specific power** p relates the total electrical power during discharge to a certain meaningful mass and is frequently given in W kg^{-1} [195].
- To quantify the degree of reversibility of electrochemical reactions in batteries, the **Coulomb efficiency** (sometimes coulombic efficiency) Φ_Q is defined by the ratio of the amount of charge accessed during discharging it, Q_{dis} , divided by the maximum charge that can be stored in the battery system upon charging it, Q_{ch} [195]. Depending on the battery system the Coulomb efficiency of a discharge-charge cycle (also cycle efficiency, charge factor) can vary between 60 % to 70 % for Li/O_2 cells and more than 99.5 % for high-quality lithium-polymer batteries.

As is obvious from the above definitions, the choice of the electrode materials determines the electrochemical reactions, which take place upon discharge and therefore also the specific energy and the specific power of the system. The amount of charge accessible during a discharge process determines the specific energy. The specific power is additionally determined by the rate at which charge can be provided. It is given by the rate at which charge transfer across the interfaces and mass transport in the individual components take place [193]. The performance of a battery is generally improved either in terms of the above mentioned quantities or in terms of lower costs for production, or increased safety.

Very attractive systems for battery applications are the ones based on Li, because of its low redox potential of -3.04 V with respect to the potential of the standard hydrogen electrode (SHE), its low molar mass of 6.94 g mol^{-1} and the small size of Li^+ ions [193]. This leads to intrinsically high theoretical specific energy and power of such cells. After some attempts comprising combinations of lithium metal as negative electrode with MnO_2 (primary battery by Sanyo in 1972) or MoS_2 (secondary battery by Moli in 1985), Sony introduced the material combination of carbon as negative electrode (anode active material, AAM) and LiCoO_2 as positive electrode (cathode active material, CAM) [197]. The terms “anode” and “cathode” are commonly used to refer to one of both electrodes in a battery and should not be confused with a certain reaction taking place at this electrode. Only during discharge, an oxidation reaction takes place at the anode (negative electrode) and a reduction reaction takes place at the cathode (positive electrode). The term “active material” refers to the participation of a material in electrochemical reactions during charge/discharge, as opposed to (electrochemically) “inactive materials”. The LIB was commercialized in 1991 and made technologies like smartphones and tablets possible. Due to large economic interests and trends toward the reduction of greenhouse gas emissions, this technology was in the focus of a very fast developing research field and still is a strong driving force for research today.

The working principle of a LIB is – like the one of an EC device – based on the insertion and extraction of Li^+ ions and electrons into/from electrode materials, which are separated by an Li^+ ion conducting electrolyte with negligible electronic conductivity. A porous membrane, which is often called a “separator”, is added to prevent a direct contact between the electrodes. The choice of the electrode materials determines the cell voltage provided by the LIB, due to the chemical potential of lithium at the surface of these materials [198]. The chemical potential of lithium in both materials also determines which electrolyte exhibits a suitable electrochemical stability window and can be employed in a certain voltage range without decomposing. The electrochemical reactions taking place during discharge and charge are



which lead to a battery system that is usually charged to 4.1 V or 4.2 V , depending on the properties of the carbonaceous material employed at the negative electrode [197, 199]. With the transfer of 0.5 mol of Li^+ ions and an average voltage of 3.8 V a theoretical specific energy, i.e. a total electrical energy related to the mass of both electrochemically active materials of 380 W h kg^{-1} results.

However, in practice, more components than the two electrochemically active electrode materials are necessary to assemble a complete electrochemical energy storage system. Some of them typically found in LIBs are listed here:

- The electrolyte is needed to enable Li^+ transport between both electrodes.
- The separator, whose pores are filled with the electrolyte, is necessary to prevent a

direct contact between both electrodes, which would short the cell.

- Metallic current collectors, namely copper at the negative electrode and aluminum at the positive electrode, provide a more homogeneous potential distribution across the electrode areas and ensure a good electronic contact.
- An electronically conducting additive, e.g., a carbonaceous material, is often used to reduce the length of the conduction pathway for electrons through comparably bad conducting electrode materials, which reduces the internal battery resistance.
- If the latter is mixed with an electrochemically active material to form a solid composite electrode, it may be necessary to improve the mechanical stability of this composite. This is achieved by adding binding materials, like polyvinylidene fluoride (PVDF).

Depending on the technical implementation of an electrochemical cell in a battery, more compounds lead to a discrepancy between theoretical and practical specific energies of any kind of battery [200]. The specific energy of the first LIBs by Sony were reported to vary between 80 W h kg^{-1} and 120 W h kg^{-1} [197]. Depending on the positive electrode material used, commercially available LIBs today have practical specific energies between 100 W h kg^{-1} and 270 W h kg^{-1} [201–203], with further improvements to over 350 W h kg^{-1} [204, 205] recently announced. A schematic depiction of a LIB is given in figure 3.5, together with schemes, showing three different battery stack designs in which LIBs are produced.

Since the commercialization of LIBs, much work has been done to improve the overall performance of this battery system in terms of the crucial characteristics mentioned above. This process includes the identification of degradation and decomposition mechanisms. This led to a very detailed picture on the numerous processes that can take place in and between the materials during cell operation and revealed fundamental limits for this system. Such investigations demonstrated structural changes and instabilities upon delithiation of LiCoO_2 , as well as oxygen evolution if the cell is charged above 4.2 V. The formation and the composition of a solid electrolyte interface (SEI) at both electrodes was also studied; its role in stabilizing the cell performance is still not clear. Further observations involve the dissolution of active positive electrode material and side reactions of the commonly used electrolyte compound LiPF_6 with moisture, which leads to the formation of HF [194, 206, 207]. In addition to these aspects, CoO_2 is an expensive ore to mine and is toxic, which complicates large-scale applications in large-scale grid storage [193].

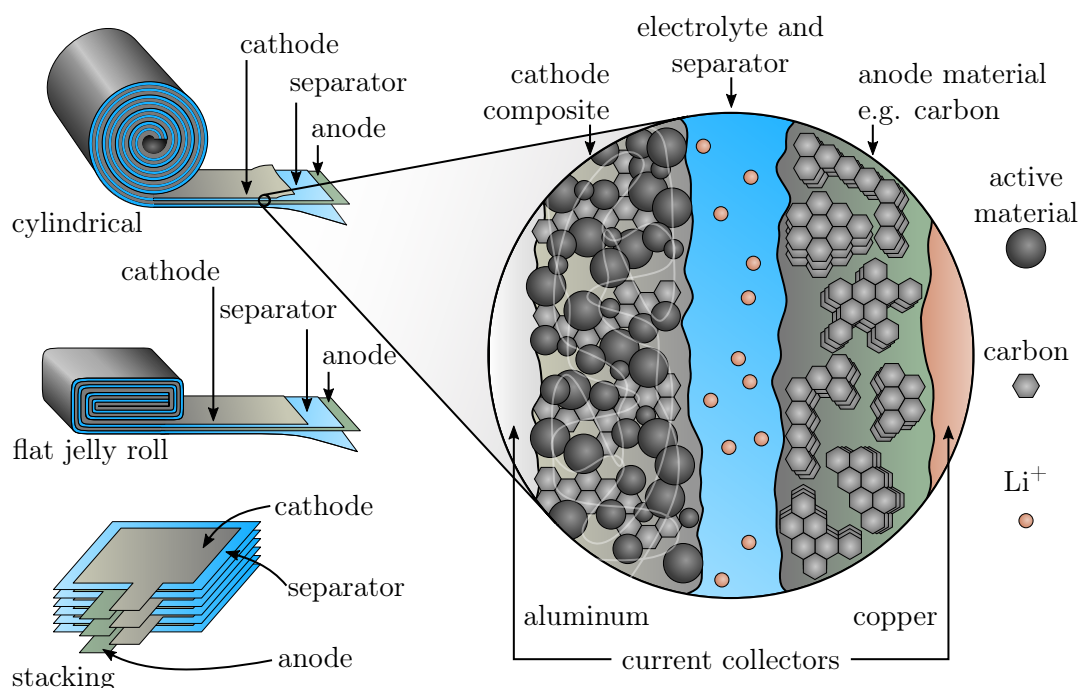


Figure 3.5: Schematic images of different battery cell stack configurations for LIBs (left) and the single components in a cell comprising current collectors, electrodes, electrolyte, and separator. The labeling of the electrodes corresponds to their function during discharge, where the oxidation takes place at negative electrode and the reduction takes place at the positive electrode. Carbonaceous materials are depicted by (stacked) grey hexagons, electrochemically active material particles at the positive electrode are depicted by dark gray circles, the binding material is represented by semi-transparent white lines and Li⁺ ions are depicted by orange circles in the electrolyte/separator region only. Adapted by permission from Springer Nature Customer Service Centre GmbH: Springer Nature, “*Lithium-Ion Batteries: Basis and Applications*” by R. Korthauer © (2018).

3.4 Positive Electrode Materials for Lithium-Ion Batteries

In order to overcome issues identified in using LiCoO₂ as a positive electrode material in LIBs, other materials and approaches have been investigated (see references 7–26 in publication 2). As a consequence, many different positive electrode materials were suggested as alternatives including other layered TMOs, spinel oxides, or polyanionic compounds [199, 206–209].

An important group of positive electrode materials, which attracts remarkable scientific interests due to advantageous properties in terms of battery performance, is the group of layered mixed TMOs with the general composition Li(Ni_{1-y-z}Co_yMn_z)O₂ (NCM) [210]. This group can conceptually be derived from LiCoO₂ upon substitution of Co³⁺ ions by Mn and Ni ions. The oxidation states of Mn and Ni in the NCM will depend on the exact composition [210]. The term “layered TMO” refers to the structure of this group of materials. They crystallize in a structure with the symmetry of the space group $R\bar{3}m$. It is similar to the structure of α -NaFeO₂, i.e. alternating layers of TMOs and Li⁺ ions are stacked. The structure with three TMO layers in its hexagonal unit cell is called “O3”

structure, referring to the octahedral coordination of Li^+ ions and the number of TMO layers in one unit cell [210]. The structure is depicted in figure 3.6.

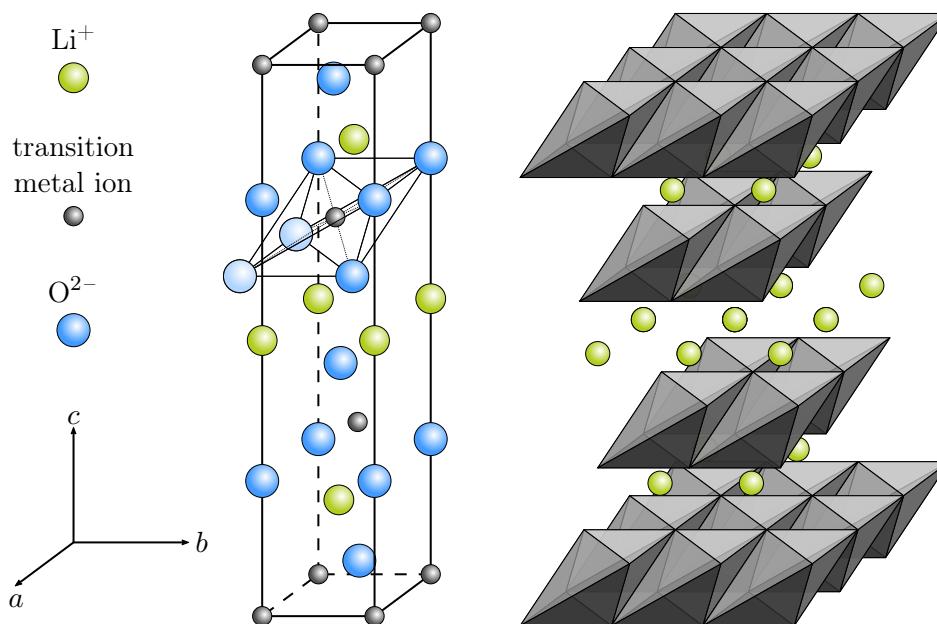


Figure 3.6: Schematic depiction of the unit cell of an NCM material in the $\alpha\text{-NaFeO}_2$ -type structure with the frame of a single TMO octahedron (left) and the layered structure of such materials with Li^+ ions between the TMO layers (right). Transition metal ions, as well as TMO octahedra are depicted in gray, O^{2-} ions in blue and Li^+ ions in green. The brighter representation of two O^{2-} ions is used to indicate that these ions are not located inside the depicted unit cell. Adapted with permission from [206]. Copyright © 2010 American Chemical Society.

The transition metal ions in NCM materials are octahedrally coordinated by O^{2-} ions, similar to the coordination of W^{6+} ions by O^{2-} ions in WO_3 . The differences between the structures are mainly that the WO_6 octahedra in WO_3 share corners, while TMO octahedra in NCM materials share edges. In addition, the formation of a layered structure allows faster Li^+ ion diffusion between and slower Li^+ ion diffusion perpendicular to the TMO layers. In contrast to that WO_3 and the analogous LiWO_3 are characterized by the three dimensional network of WO_6 octahedra providing a less anisotropic host material for Li^+ ion diffusion.

By combining different transition metals, the advantageous impact of each type of ion on the properties of the positive electrode material can be used to improve the performance of the positive electrode material in a battery. An increase in the nickel content increases the specific charge, due to the oxidation of Ni^{2+} in the discharged state to Ni^{4+} in the charged state. Also the costs for production can be reduced, due to the lower prices of nickel compared to cobalt. Drawbacks from a larger nickel content are an increase in the structural and thermal instability, as well as cation-disorder, due to the similar size of Ni^{2+} ions (0.69 \AA) and Li^+ ions (0.76 \AA). This can be suppressed by a higher cobalt content,

which also increases the rate performance, but comes along with the drawbacks already mentioned. The substitution of cobalt by manganese leads to the reduction in the specific charge, since manganese does not take part in the redox reaction, but it increases the structural and thermal stability of the material and is less expensive than nickel [210]. Some alternative positive electrode materials to LiCoO_2 that have been commercialized are LiMn_2O_4 , $\text{LiNi}_{1/3}\text{Co}_{1/3}\text{Mn}_{1/3}\text{O}_2$, $\text{LiNi}_{0.8}\text{Co}_{0.15}\text{Al}_{0.05}\text{O}_2$, and LiFePO_4 , which generally represent compromises between a desired reduction of the costs and the size or weight of the batteries as well as increased safety [196].

Regardless of the chemical composition of the electrode material, the active materials of both electrodes are usually powders, which are processed in a slurry-based preparation procedure of composite electrodes (see [196], as well as references 27–56 in publication 2). A procedure for the preparation of composites for positive electrodes frequently reported starts with a mixture of the electrochemically active material(s), electronically conducting agent(s) like carbons, and mechanically stabilizing binder(s) such as PVDF. Depending on the solubility of the binder, the compounds are dispersed in a solvent (N-methyl pyrrolidone (NMP) for PVDF) to dissolve the binder and ensure its homogeneous distribution in the slurry. The latter is pasted on a current collector and releases NMP during an appropriate heat treatment [196, 211]. The exact composition of the additives vary between 1 % to 5 % for the conducting agents and 2 % to 8 % for the binding material, depending on whether batteries with high energies or high power are desired [196]. It is often assumed that the additives in a composite positive electrode are electrochemically inactive or that their presence has only negligible influence on the electrochemical properties of the composite beyond their intended purpose. However, according to several reports (see [212, 213] as well as references 27–56 in publication 2), this assumption cannot be expected to hold in general.

Very similar to the investigation of properties of WO_3 thin films, the development and improvement of electrode materials for LIBs is to a large extent studied in terms of the performance of half- or full-cell setups, in which the materials are employed in. The performance of a cell together with low costs for the materials and safe operation, are some of the most essential specifications, which decide on the applicability of certain materials or material systems and are crucial to characterize. However, the results from such experiments on half- or full-cell setups themselves are in general not suitable to evaluate selected properties of single components or even single materials in the system. This is a very important aspect to consider in order to understand the plethora of results on properties of positive electrode materials reported in the literature. The extent to which single materials in a composite electrode influence certain properties of the composite or influence the overall electrochemical performance is still hardly known. This might especially be due to the complexity of technologically relevant material systems in terms of morphology and composition, which leads to difficulties in systematic variation of a single property. Technologically relevant positive electrode active materials are in most cases used in the form of more or less porous particles with mean diameters between several hundreds of

nanometers and a few micrometers. They are made up by smaller crystalline primary particles, which are sintered to form spherical secondary particles [214, 215]. This inherently complicates the systematic investigation of fundamental properties by means of established experimental approaches simply due to the small size and the disadvantageous morphology of the particles. Systematic investigations on such particles are therefore generally related to experimental efforts exceeding cycling tests of composites or standard electrochemical techniques in half- or full-cell setups.

To overcome the aforementioned issue and to investigate essential properties like charge transport in positive electrode active materials, several approaches have been reported. Two approaches with comparably low additional experimental effort are the preparation of pressed or pressed and sintered pellets [216] or the investigation of loose agglomerates of particles [217]. This allows the characterization of a macroscopic agglomerate of single particles with contacts of varying quality between each other. The charge transport through such an agglomerate is determined by its microstructure, as well as by the properties of grains and grain boundaries. Experiments on such agglomerates rather provide access to information on average properties of the agglomerate than on bulk properties of the positive electrode active material particles. How much average properties differ from the intrinsic properties is the subject of current research. Furthermore, it is not clear whether the particle network obtained by sintering or compressing primary particles actually corresponds to that of a porous secondary particle.

For these reasons, it is desirable to also obtain information on the charge transport in single secondary particles, which would allow systematic investigations of possible correlations between charge transport in pressed pellets and single secondary particles. Furthermore, computational studies on LIBs frequently depend on assumptions about the conductivity of the positive electrode active material or about the effective conductivity of single particles [218]. The assumptions might in some cases be adequate enough, but require a certain experimental foundation and validation.

4 Results and Discussion

The goal of this work was the development of experimental approaches capable of addressing the lack of results in the field of charge transport in TMOs, which were identified in the literature and described in the previous chapter. Some of the results obtained during this process of development, as well as conclusions drawn from the interpretation of experimental data were published in scientific journals, which led to the two peer-reviewed publications this thesis is based on.

4.1 Diffusion of Hydrogen in WO₃ Thin Films (Publication 1)

The lack of results on diffusion in WO₃ obtained from experimental approaches different from those of electrochemical approaches accompanied the work in this field from the beginning. This statement is independent of the morphology of the thin films: neither for amorphous nor for polycrystalline thin films has the evolution of the ion concentration in the diffusion process been resolved in space and time.

In order to investigate the diffusion of ions in WO₃ thin films, it is necessary to generate a gradient in the concentration of ions in the film. This requires locally confined insertion of ions and the monitoring of the ion diffusion perpendicular to the direction of ion insertion. This was achieved by making use of a specially designed electrochemical cell in three-electrode configuration with a working electrode (a WO₃ thin film), a counter electrode (a platinum tube), a Ag/AgCl-reference electrode and a liquid electrolyte (H₂SO₄, 0.1 mol L⁻¹). The cell design was adopted from Wallys et al. and modified by Darmawi et al. to allow for the in situ measurement of the optical transmittance/reflectance [113, 219]. A detailed description of the cell can be found in section A of the appendix. The local confinement of the ion insertion, i.e. the avoidance of homogeneous ion insertion and the formation of a concentration gradient was achieved by a thin layer of poly(methyl methacrylate) (PMMA) on top of the WO₃ surface facing toward the liquid electrolyte. The PMMA layer was patterned by electron beam lithography in a way that a gap with a width of 50 μm was exposed and dissolved during the development. This created a spatially confined area, through which ion insertion could take place. After being electrochemically inserted by the application of a voltage ($E_{WE} = -0.3\text{ V vs. } E_{Ag/AgCl}$), the ions diffuse perpendicular to the direction of insertion through the film. Due to the EC properties of WO₃, the diffusing ions induce a coloration in the film. This change in absorbance served as a qualitative indicator for the ion concentration in the film. It was measured in terms

of the transmittance by employing a white light source, a microscope objective, a subtractive double spectrometer and a charged coupled device (CCD) image sensor. By this, the ion concentration in the film is resolved in space and time, while changes in the reflectivity upon coloration are neglected. The assumption that the reflectivity is not changing upon coloration does explicitly not hold for crystalline WO_3 thin films and wavelengths above 1000 nm. For the spectral range selected by the subtractive double spectrometer ((637 ± 15) nm) however, the changes in the reflectivity are reported to be small [148] and are estimated to be below $\Delta R = \pm 0.06$ upon coloration [132].

The ideas, the concept, and the experimental setup itself were developed by S. Darmawi, M. T. Elm, and P. J. Klar and first experiments were conducted by me together with S. Darmawi prior to the work on my PhD thesis. The subsequent work concentrated on the representation of the obtained experimental data, the interpretation and simulations of several models including diffusion with one or two constant diffusion coefficients. Additional experiments with supporting character necessary to prove the direct correlation between the overall changes in the transmittance and those detected in the spectral range of (637 ± 15) nm were conducted. Numerical simulations were developed in collaboration with and conducted by B. Lani-Wayda. The manuscript was written by me and edited by the co-authors. The article is reprinted with permission from *Advanced Materials Interfaces*, **2018**, *5* (6), 1701587. (DOI: <https://doi.org/10.1002/admi.201701587>)

Copyright © 2018 WILEY-VCH Verlag GmbH & Co. KGaA, Weinheim

In Situ Monitoring of Lateral Hydrogen Diffusion in Amorphous and Polycrystalline WO₃ Thin Films

Simon Burkhardt, Matthias T. Elm,* Bernhard Lani-Wayda, and Peter J. Klar

Thin films of electrochromic materials such as tungsten trioxide (WO₃) are essential components of electrochromic devices such as “Smart Windows.” The transport of charge carriers in WO₃ thin films has been investigated intensively over the past decades, yielding a wide spread of diffusion coefficients of hydrogen in WO₃. Most of those analyses are based on measurements by electrochemical methods. However, such analyses are only applicable and the results reliable in cases where diffusive transport is the rate-determining process. Here, WO₃ thin films of different morphology are prepared by electron-beam evaporation of WO₃ powder. The combined lateral diffusion of protons and electrons is investigated inside amorphous and polycrystalline WO₃ thin films by in situ transmission spectroscopy during electrochemical hydrogen insertion into the film. The insertion of the protons is carried out locally and lateral diffusion of H takes place in the film plane. The induced change of the film absorbance at a wavelength of (637 ± 15) nm is monitored and spatially and temporally resolved. The results reveal a concentration-dependent diffusion process of hydrogen in both, amorphous and polycrystalline WO₃, which are critically discussed in the context of existing data from literature.

1. Introduction


Tungsten trioxide (WO₃) and its electrochromic properties have been studied intensively since first reported by Deb almost 40 years ago.^[1] Driving force are its use in a variety of applications such as “smart windows” or gas sensors.^[2] Recent research also addressed the application of WO₃ thin films as electrode material in lithium-ion batteries.^[3] All these applications rely on the reversible insertion and extraction of ions and electrons. Understanding the fundamental processes of insertion

S. Burkhardt, Dr. M. T. Elm, Prof. P. J. Klar
 Institute of Experimental Physics I,
 Heinrich-Buff-Ring 16, 35392 Giessen, Germany
 E-mail: matthias.elm@exp1.physik.uni-giessen.de

S. Burkhardt, Dr. M. T. Elm, Prof. P. J. Klar
 Center for Materials Research (LaMa)
 Heinrich-Buff-Ring 16, 35392 Giessen, Germany

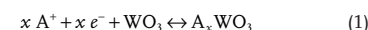
Dr. M. T. Elm
 Institute of Physical Chemistry
 Heinrich-Buff-Ring 17, 35392 Giessen, Germany

Prof. B. Lani-Wayda
 Mathematical Institute
 Arndtstrasse 2, 35392 Giessen, Germany

 The ORCID identification number(s) for the author(s) of this article can be found under <https://doi.org/10.1002/admi.201701587>.

DOI: 10.1002/admi.201701587

and transport of ions and electrons in WO₃ thin films comprises an important task in the optimization of existing and the development of future devices. The amount of work published on thin film deposition methods, characterization of electrochromic coloration processes, and possible coloration mechanisms is huge.^[4] In a simplified picture, the electrochromic coloration and bleaching of WO₃ can be described by a reversible insertion and extraction of electrons and ions according to Equation (1)



where A⁺ denotes a small ion such as H⁺, Li⁺, or Na⁺ and leads to the reduction of W⁶⁺ states to W⁵⁺ or W⁴⁺ states. The changed oxidation state of W modifies the electronic structure of the material such that photons in the visible region of the electromagnetic spectrum may be absorbed. Despite long-lasting intensive

research and commercialization of WO₃-based electrochromic devices, the fundamental processes of the correlated insertion of electrons and ions into the crystal structure of WO₃ and their impact on the absorption of visible light are still under debate.^[5] Thus, more advanced methods are still continuously developed to yield additional insight into the effects of cation and electron insertion into WO₃.^[6] Besides the work on insertion and extraction of charge carriers into WO₃, the diffusive transport of the inserted species itself also has been investigated in WO₃ thin films, in particular, the diffusion of hydrogen in thin films of different morphology.^[7] The term “morphology” is used here to emphasize that different thin film preparation methods and postdeposition treatments not only influence the crystallinity but also other structural properties of the film, in particular, its microstructure, e.g., size and shape of the grains, type of grain boundaries, and film porosity. It should be noted that most of the results published are based on the derivation of diffusion coefficients from electrochemical experiments such as chronoamperometry or electrochemical impedance spectroscopy. The results obtained during such measurements usually do not deliver spatially resolved information, but rather an integrated view of the diffusion processes taking place. Furthermore, the kinetics of proton insertion at the interface between electrode and electrolyte tend to influence the results obtained by distorting the view on the diffusional transport in the WO₃ lattice. Spatial resolution on the microscale is necessary to resolve

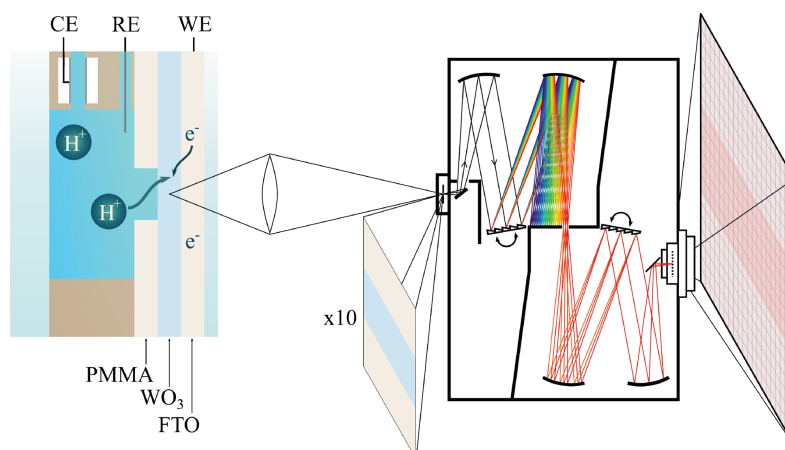


Figure 1. Experimental setup used for resolving the lateral hydrogen distribution in WO_3 thin films during locally confined electrochemical hydrogen insertion: A magnified image of the sample back surface passes a subtractive double spectrometer, where it is imaged onto the active area of a CCD detector array (CE: counter electrode, RE: reference electrode, WE: working electrode).

morphological effects on transport properties and rate determining steps. These prescribe cycling and switching behavior of the thin films and are therefore of major interest for performance enhancement. To study the diffusive transport of hydrogen in thin films, a concentration gradient perpendicular to the thin film normal must be established. This requires a locally confined insertion of electrons and protons, forming atomic hydrogen.^[8]

2. Results and Discussion

In this work we locally confined the electrochemical insertion of hydrogen into WO_3 thin films by making use of an additional microstructured polymethylmethacrylate (PMMA) layer on top of the WO_3 film. Our approach is somewhat similar to that of Vértés and Schiller.^[9] To analyze the diffusion process, we performed in situ UV–vis transmission spectroscopy which has been established as a valuable tool in studies of many other materials showing optical transitions.^[10] The spectral range suitable for spatial and temporal transmission imaging is selected based on a compromise between the magnitude of the hydrogen-induced change of the WO_3 absorption and a high signal-to-noise ratio of the absorbance calculated from transmission data. The back surface of the sample is imaged onto the active area of a CCD detector array using the transmitted light in the spectral region of interest. Images taken at subsequent moments in time allow us to monitor the time-evolution of the diffusion process. A schematic image of our experimental setup for acquiring spatially and temporally resolved transmission data is shown in Figure 1 (see the Experimental Section for additional information).

On the basis of Lambert-Beer's law the experimental results can be directly converted into the spatial and temporal evolution of the hydrogen distribution in the WO_3 films. The diffusion coefficients of hydrogen in amorphous and polycrystalline WO_3

can be extracted by comparing the experimental results with numerical simulations of the diffusion process.

WO_3 thin films without an additional cyclic PMMA layer have been colored homogeneously using cyclic voltammetry (CV). The CV data obtained from a polycrystalline thin film are depicted in Figure 2a (see X-ray diffraction patterns in Figure S1 and scanning electron microscopy images in Figure S2 of the Supporting Information). The cathodic current peaks at -130 mV versus $E_{\text{Ag}/\text{AgCl}}$ and -285 mV versus $E_{\text{Ag}/\text{AgCl}}$ are related to the reduction of W^{6+} to W^{5+} and to the reduction of W^{5+} to W^{4+} , respectively.^[6a] It has been shown that the contributions of both electrochemical reactions to the overall coloration of WO_3 thin films vary significantly, meaning that the main contribution to electrochromic coloration is related to the reduction of W^{5+} to W^{4+} states.^[6a] Inspection of the current integrated during one cycle shows that a significant amount of charge is involved into irreversible reactions in the cathodic regime and cannot be recovered in the anodic part of the CV. Transmission spectra at distinct potentials marked in the CV are depicted in Figure 2b. The transmission spectrum measured at the open cell potential of 179 mV versus $E_{\text{Ag}/\text{AgCl}}$ basically agrees with the spectrum of the halogen lamp, i.e. there is no significant absorption of visible light. This changes, when the potential is lowered. The transmittance is attenuated due to hydrogen insertion and the occurring electrochromic coloration. This process is reversed as the current switches from the cathodic to the anodic regime, leading to an increase of transmission and a bleaching of the WO_3 film.

The change in transmission in the transmission spectra measured is most pronounced at wavelengths above 600 nm. Based on these results, we chose the wavelength of (637 ± 15) nm for monitoring the spatially and temporally resolved diffusion process in the film plane which we will describe in what follows. At this wavelength both, the signal-to-noise ratio of the detection system and the hydrogen-induced change of WO_3 absorbance are high.

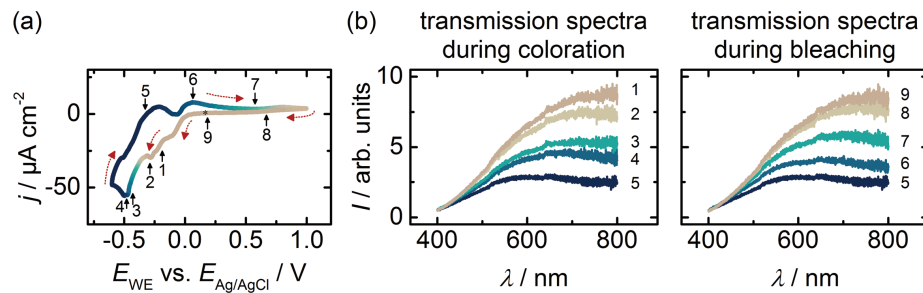


Figure 2. In situ transmission spectroscopy during electrochemical hydrogen insertion: a) Cyclic voltammogram showing two current peaks related to tungsten reduction and a subsequent current increase due to electrolyte decomposition at lower potentials. b) Intensity of transmitted radiation during coloration and bleaching.

The absorbance A_e was calculated using Equation (2)

$$A_e = -\ln\left(\frac{I}{I_0}\right) \quad (2)$$

where I is the intensity of transmitted radiation and I_0 is the intensity of transmitted radiation passing an uncolored WO₃ thin film.^[11] In order to derive hydrogen concentration profiles from the optical measurements, a Lambert–Beer like ansatz is used

$$I = I_0 \exp[-l(\varepsilon_1 c_1 + \varepsilon_2 c_2)] \quad (3)$$

where I_0 is the intensity transmitted through the uncolored sample, l is the absorption path length, ε_1 and ε_2 are the molar absorption coefficients which describe the absorption due to transitions from W⁶⁺ to W⁵⁺ and from W⁵⁺ to W⁴⁺, respectively, and c_1 and c_2 are the corresponding concentrations of W⁵⁺ and W⁴⁺ states. However, as recently discussed by Darmawi et al.,^[6a] the electrochromic coloration is strongly correlated to the formation of W⁴⁺ states upon electrochemical reduction. Taking this into account, ε_1 may be neglected and the absorbance can be approximated by

$$A_e \approx l\varepsilon_2 c_2 \quad (4)$$

Furthermore, assuming a constant molar absorption coefficient ε_2 for the dominating absorption process and a constant film thickness l , the spectral absorbance must be linearly correlated with the concentration of W⁴⁺ states and, thus, with

the concentration of hydrogen in the WO₃ thin film. This interpretation may lead to an overestimation of the hydrogen concentration, since the insertion of extrinsic species into the WO₃ host lattice also leads to changes in the reflectivity of the thin film. However, reflectivity measurements revealed only minor changes in the reflectivity of WO₃ thin films upon electrochromic coloration in the spectral range investigated in this work.^[12] This approach also neglects changes of absorption and reflectivity of both the FTO film and the glass substrate. However, these are not expected to play a significant role.

Prior to the spatially and temporally resolved measurements, we have to prove that the analysis of the diffusion process based on the sample's response at the single wavelength of (637 ± 15) nm is representative for the hydrogen-induced change of the spectrally integrated response of the sample, i.e., the correlation between the amount of hydrogen inserted and the electrochromic coloration process. This is justified, if a linear correlation between the response at the single wavelength and the integrated response holds. For this purpose, the changes of the absorbance at (637 ± 15) nm and the corresponding values integrated over the entire spectral range are extracted from transmission spectra taken during one CV cycle and compared. **Figure 3a** shows the time evolution of both, the absorbance $A_{\text{int,total}}$ integrated over the full spectral range from 400 to 800 nm and the absorbance $A_{\text{int,partial}}$ integrated over a spectral range from 622 to 652 nm. Both integrated absorbance curves exhibit the same time evolution. They increase upon hydrogen insertion and decrease upon hydrogen extraction. A plot of $A_{\text{int,partial}}$ versus $A_{\text{int,total}}$ depicted in **Figure 3b** further confirms the linear relationship between the two entities.

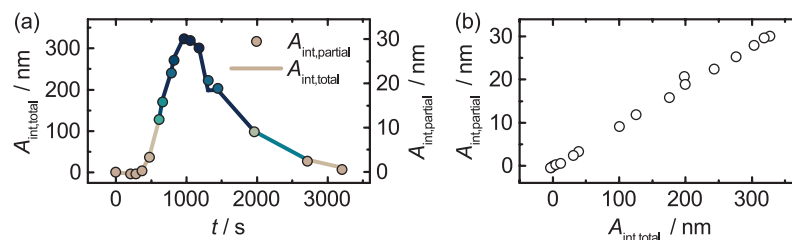


Figure 3. a) Temporal evolution of the absorbance integrated over the whole spectral range from 400 to 800 nm $A_{\text{int,total}}$ and the absorbance integrated over the spectral range from 622 to 652 nm $A_{\text{int,partial}}$. b) Depiction of the linear relationship between $A_{\text{int,total}}$ and $A_{\text{int,partial}}$.

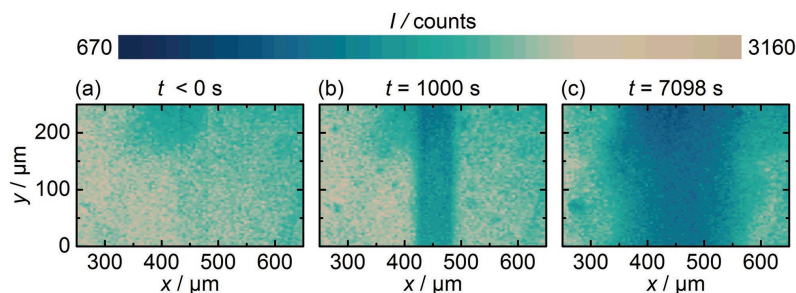


Figure 4. Transmission images of the diffusion process recorded a) prior to applying a constant potential, b) 1000 s, and c) 7098 s after applying -0.3 V versus $E_{\text{Ag}/\text{AgCl}}$.

Thus, the results depicted in Figures 2 and 3 justify the assumption that the transmission variation in the spectral range of (637 ± 15) nm is representative for the variation of the hydrogen concentration in the WO_3 thin films.

We used various WO_3 thin films each with a patterned PMMA layer on top may lead for the spatially and temporally resolved measurements (see the Experimental Section for details). Light with a wavelength of (637 ± 15) nm passing through the sample in the areas next to the $50 \mu\text{m}$ wide stripe-like gap in the PMMA layer is imaged onto the CCD detector array. As an example, **Figure 4** shows such images of the transmission of a polycrystalline WO_3 thin film obtained at different stages of the diffusion process.

In the uncolored state of the WO_3 thin film, only weak signs of the PMMA layer can be seen in the image (see **Figure 4a**), therefore, it can be assumed in the following that additional absorption due to PMMA is negligible. The cathodic voltage applied to

the sample leads to the insertion of hydrogen and electrochromic coloration in the gap area of the PMMA layer. The continuous insertion and the lateral diffusion of hydrogen lead to transmission changes below the PMMA layer (**Figure 4b,c**).

The intensity changes have been used to calculate the absorbance according to Equation (2) after correcting the obtained data for the dark current of the CCD detector array. Single absorbance profiles are evaluated along the x direction, i.e. perpendicular to the gap of the PMMA layer, to analyze the lateral diffusion of hydrogen in the sample plane. It is justified to treat the lateral diffusion as 1D along x as the stripe is much longer than wide. Intensity values for each x have been obtained by averaging the readings of 10 CCD pixels in the y -direction (representing $6.45 \mu\text{m}$ in real space). **Figure 5a,b** shows the time evolution of the absorbance in the gap of the PMMA layer for an amorphous and polycrystalline WO_3 thin film, respectively. The corresponding extracted spatial absorbance profiles

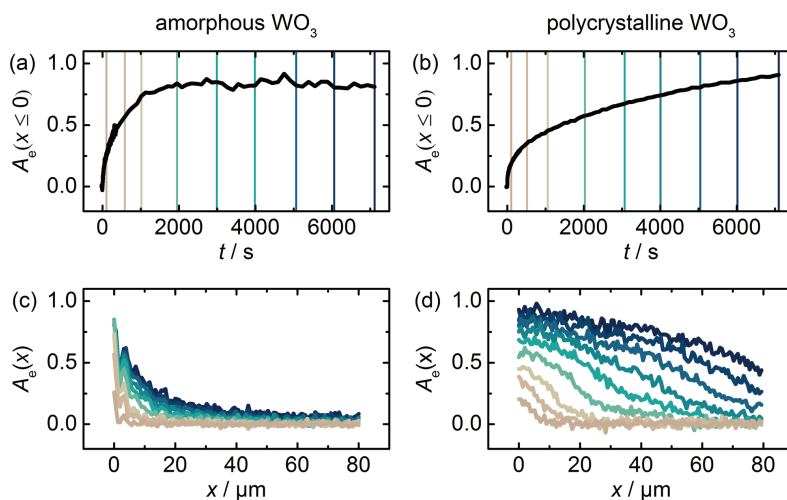


Figure 5. Absorbance resolved temporally and averaged over sample spots (corresponding to $x \leq 0$) located in the gap of the PMMA layer on top of a) an amorphous and b) a polycrystalline WO_3 thin film. Spatially resolved absorbance perpendicular to the gap in the PMMA layer and in plane of c) an amorphous and d) a polycrystalline WO_3 thin film, respectively. Vertical lines in (a) and (b) mark times at which a spatial absorbance profile is shown in (c) and (d), respectively.

perpendicular to the edge of the PMMA layer are plotted in Figure 5c and d for different times corresponding to the duration of the insertion process.

The absorbance in both amorphous and polycrystalline films are strongly affected by the WO₃ thin film morphology. Not only the kinetics of the potentiostatic insertion of hydrogen, but also the lateral diffusion kinetics differs significantly. The insertion kinetics of hydrogen can be monitored in the gap of the PMMA layer ($x \leq 0$). In an amorphous environment (Figure 5a), absorbance shows a faster increase and saturates after ≈ 2000 s of continuous insertion. A very similar behavior has also been observed by Dini et al. during potentiostatic measurements (however, no detailed information about the WO₃ thin film morphology was given).^[13] Hydrogen insertion into polycrystalline films is much slower and does not saturate during the duration of the experiment of 7100 s (Figure 5b). The observation of different electrochromic coloration kinetics has been widely observed and reported in literature.^[4c] In particular, the strong impact of thin film deposition and annealing parameters on film morphology complicate a comparison of results obtained by different authors and, thus, a detailed explanation. For example, the thermal treatment used to initiate the crystallization of an amorphous WO₃ film may lead to a decrease of film porosity.^[4c,14] This has been shown to impede ion insertion and extraction.^[15] The fast increase of absorbance in our measurements may be attributed to the less dense structure of the amorphous WO₃ thin film compared to the polycrystalline film. The lower density facilitates a penetration of the film by the electrolyte solution. Thermal treatment is also known to reduce the contact resistance between the WO₃ film and the substrate and to increase the electronic conductivity of the WO₃ film.^[14,16] Since there were only slight variations of the open cell potentials before the start of each measurement and the applied potential is set to -0.3 V versus $E_{\text{Ag}/\text{AgCl}}$ in both experiments, an increase of the conductivity of the thin film leads to a reduced potential drop across the polycrystalline WO₃ thin film. Thus, the potential difference at the interface between electrolyte and sample surface initiating the coloration process is higher, leading to a slightly higher overall electrochromic coloration of the polycrystalline WO₃ film. A saturation of absorbance in the polycrystalline WO₃ thin film is then expected to occur at larger time scales.

While many other groups found that diffusion of hydrogen in amorphous WO₃ thin films is faster than in polycrystalline films (see Table 2), a qualitative analysis of the results presented in Figure 5c,d supports the picture of faster diffusion of hydrogen in polycrystalline WO₃ thin films. This is indicated by the finding that changes of the absorbance occur at larger horizontal distances from the gap in the PMMA layer in polycrystalline films at all times in our measurements. Furthermore, the diffusion processes taking place seem to differ. The absorbance profile observed in the amorphous film (Figure 5c), at first sight, seems to correspond to the standard solution of the diffusion equation with a constant diffusion coefficient. As will be shown later, the diffusion coefficient in the amorphous WO₃ thin film decreases as a function of concentration as already shown by Vértés and Schiller.^[9] In contrast, the absorbance profile in the polycrystalline film shows

a decreasing slope as a function of spatial coordinate x after ≈ 2000 s. This cannot originate from a diffusion process with a constant diffusion coefficient. It rather indicates that the diffusion coefficient increases with increasing hydrogen content.

To obtain a more detailed understanding of the diffusion profiles depicted in Figure 5c,d, numerical simulations have been performed. The description of the diffusion process in WO₃ is based on the differential equation for concentration-dependent diffusion

$$\frac{\partial c}{\partial t} = \frac{\partial}{\partial x} \left(D(c) \frac{\partial c}{\partial x} \right), t \geq 0, x \in [0, L] \quad (5)$$

where L denotes the spatial range investigated. The concentration-dependence of the diffusion coefficient D is modelled on an empirical basis assuming the mathematical dependence

$$D(c) = D_i + \Delta D \sigma \quad (6)$$

where

$$\Delta D = D_f - D_i \quad (7)$$

is the difference between an initial and a final diffusion coefficient D_i and D_f and $\sigma(c)$ describes a monotonic transition between both diffusion coefficients. The transition from D_i to D_f is assumed to begin at a threshold concentration c_0 and to end at a concentration c_{max} , which corresponds to the last data points measured in experiment. Thus, $\sigma(c)$ needs to satisfy $\sigma(c \leq c_0) = 0$ and $\sigma(c \geq c_{\text{max}}) = 1$. The qualitative shape of the transition is defined by

$$\frac{\partial \sigma(c)}{\partial c} = k \left(\frac{c - c_0}{c_{\text{max}} - c_0} \right)^p \left(1 - \frac{c - c_0}{c_{\text{max}} - c_0} \right)^q \quad (8)$$

This dependence of $\sigma(c)$ leads to an approximate behavior of the form $(c - c_0)^{(p+1)}$ in the limit $c \rightarrow c_0$ and $1 - (c_{\text{max}} - c)^{(q+1)}$ in the limit $c \rightarrow c_{\text{max}}$. The coefficient k in Equation (8) is used to normalize $\sigma(c_{\text{max}}) = 1$ and can be calculated explicitly, if $q \in \{0, 1, 2, \dots\}$, whereas p is chosen to be a number in $[-1, \infty)$, to avoid singularities in the transition function $\sigma(c)$. The diffusion coefficient $D(c)$ obtained by fitting this model to experimental data is characterized by the initial diffusion coefficient D_i , the final diffusion coefficient D_f , the threshold concentration c_0 and the parameters p and q . According to Equations (4) and (5) the results from numerical simulations are assumed to hold for the measured absorbance A_e as well as the hydrogen concentration c .

Table 1. Summary of the parameters used in the numerical simulations to fit experimental data of the various samples studied. Experimental results depicted in Figure 5 are denoted by sample number 1.

	Sample number	A_0	D_i [cm ² s ⁻¹]	D_f [cm ² s ⁻¹]	p	q
a-WO ₃	1	0.038	1.33×10^{-8}	2.90×10^{-10}	-0.75	6
	2	0.011	1.42×10^{-8}	3.20×10^{-10}	-0.85	7
p-WO ₃	1	0.450	0.27×10^{-8}	3.28×10^{-8}	0.00	0
	2	0.510	0.21×10^{-8}	3.57×10^{-8}	0.00	0

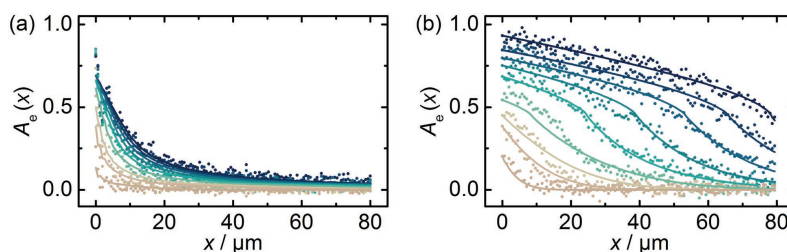


Figure 6. Comparison of experimental (dots) and simulated values (lines) for $A_e \propto c$ in a) an amorphous (sample 1 in Table 1) and b) a polycrystalline (sample 1 in Table 1) WO_3 thin films.

Thus, the threshold concentration c_0 corresponds to the absorbance A_0 . Additional information about the implementation of the model in numerical simulations is given in the Supporting Information. Best agreement between experimental and simulated data was found for the values summarized in Table 1.

A comparison between the experimental results depicted in Figure 5c,d and numerically simulated values of the absorbance is given in Figure 6, showing that the numerical simulations describe the experiments very well. This is strong evidence that the diffusion coefficients of hydrogen in both types of WO_3 thin films are indeed concentration-dependent and, furthermore, that the concentration dependence depends on film morphology. The result of the simulations, the variation of the diffusion coefficients in amorphous and polycrystalline WO_3 thin films are depicted in Figure 7.

It should be noted that the results obtained by numerical simulations give no information about the details of the microscopic mechanisms behind concentration-dependent diffusion processes yielding the electrochromic behavior observed. The concentration-dependence of the diffusion coefficients is approximated within the limits of the mathematical description

given by Equations (6)–(8). Explaining the dependence found empirically on a microscopic level and describing the motion of individual charge carriers or ions is a task of future work and beyond the scope of this work.

A comparison of the results presented here with those from earlier reports on hydrogen diffusion in WO_3 thin films is given in Table 2.

The magnitude of the diffusion coefficient in amorphous films determined in this work fits well into the range of published values, although mostly concentration-independent diffusion in amorphous WO_3 films was investigated. A comparison of our results with those from Vértés and Schiller reveals a very similar qualitative dependence of the diffusion coefficient on hydrogen concentration, whereas the absolute values of the diffusion coefficients differ significantly. The model used by those authors was based on the assumption of two intertwining diffusion channels of different diffusivities for hydrogen.^[9] An alternative explanation of the decrease of the diffusion coefficient with increasing hydrogen concentration could be the reduction of the number of unoccupied lattice sites accessible for protons. This in turn would also reduce the number of dif-

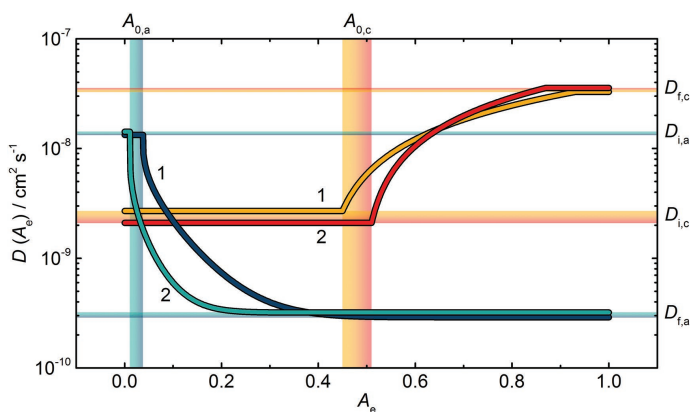


Figure 7. Dependence of hydrogen diffusion coefficient D on absorbance $A_e \propto c$ in two amorphous (blue and cyan) and two polycrystalline (red and orange) WO_3 thin films extracted by numerical simulations (labelling of the curves corresponds to the sample numbers in Table 1). Colored areas in the background depict the variation of the offset absorbance in amorphous ($A_{0,a}$) and polycrystalline ($A_{0,c}$) WO_3 thin films, as well as the variation of the initial ($D_{i,a}$, $D_{i,c}$) and final diffusion coefficients ($D_{f,a}$, $D_{f,c}$) in both kinds of films.

fusion paths and thus restrict the transport of protons through the WO_3 lattice. Furthermore, lattice sites with different capabilities of trapping extrinsic ions are present in amorphous WO_3 , those interplay may play an important role in the diffusion process.^[26] Malmgren et al. very recently reported on a potential-dependent effective diffusion coefficient of lithium ions in amorphous sputtered WO_3 thin films.^[27] This clearly indicates that the assumption of a constant diffusion coefficient in WO_3 thin films does not necessarily hold, which in turn requires for a more careful interpretation of results obtained by electrochemical experiments. The results on hydrogen diffusion in polycrystalline WO_3 thin films are several orders of magnitude higher than most of those, found in literature for amorphous and polycrystalline material. Since the majority of data reported in literature is derived from electrochemical methods, the diffusion coefficients published tend to reflect the overall kinetics of electrochemical insertion/extraction of

Table 2. Overview of the diffusion coefficients of hydrogen in WO₃ films of different morphology and electrons in WO₃ films determined in this work and published in literature.

D [cm ² s ⁻¹]	Method	Ref.
Amorphous WO ₃ (a-WO ₃)		
5.28×10^{-8}	Chronoamperometry	[7b]
2.00×10^{-8}	Chronoamperometry	[5f]
3.45×10^{-9} – 5.10×10^{-10}	Cyclic voltammetry	[17]
2.40×10^{-9}	Cyclic voltammetry	[18]
1.70×10^{-9} – 3.40×10^{-10}	Impedance Spectroscopy	[19]
1.00×10^{-9}	Chronoamperometry	[20]
1.00×10^{-9} – 2.00×10^{-10}	Cyclic voltammetry	[7c]
6.50×10^{-10} – 3.90×10^{-11}	Impedance Spectroscopy	[16]
4.00×10^{-10}	Chronoamperometry	[21]
1.80×10^{-10}	Chronoamperometry	[7a]
1.06×10^{-10} – 8.16×10^{-11}	CA-Boltzmann ^{a)}	[9]
3.00×10^{-12} – 1.00×10^{-12}	Chronoamperometry	[15]
1.33×10^{-8} – 2.90×10^{-10}	This work	
Crystalline WO ₃ (c-WO ₃)		
4.95×10^{-10}	Nuclei Magnetic Resonance	[22]
4.60×10^{-11} – 5.20×10^{-12}	Impedance Spectroscopy	[19]
2.00×10^{-11} – 1.10×10^{-11}	Chronoamperometry	[7a]
3.28×10^{-8} – 2.70×10^{-9}	This work	
Anodic WO ₃		
3.00×10^{-7}	Chronoamperometry	[20]
6.00×10^{-8}	Chronoamperometry	[21]
5.00×10^{-8}	Cyclic voltammetry	[7c]
7.10×10^{-11} – 2.90×10^{-11}	Impedance Spectroscopy	[23]
Electrons in WO ₃		
5.05×10^{-3} – 1.26×10^{-3}	Gating ^{b)}	[24]
2.50×10^{-3}	Short circuit In wire ^{c)}	[25]

^{a)}H-saturating WO₃ film via chronoamperometry, analyzing diffusion profile via Boltzmann-method; ^{b)}Electrolyte gating using ionic liquid; ^{c)}Short-circuit indium wire and WO₃ film, immersed in electrolyte.

hydrogen, rather than the pure diffusive transport in crystalline WO₃ thin films. Only if the diffusive transport of hydrogen in the WO₃ lattice is the rate-determining process and not the transport of protons through the electrolyte or across the double-layer at the electrolyte-WO₃-interface, electrochemical methods yield the real diffusion coefficient in WO₃. If these requirements are not fulfilled, the diffusion coefficient extracted must be considered an effective one and can be considerably smaller than the real one. Furthermore, models describing the bleaching of crystalline WO₃ thin films need to take chemical side reactions such as pronounced self-bleaching in the case of hydrogen into account.^[5c,28] The results presented here show that the hydrogen diffusion process itself in polycrystalline WO₃ thin films is probably not the rate-determining process in such electrochemical insertion/extraction experiments as widely assumed. The desirable combination of a small diffusing species and an open crystal structure with diffusion channels

leads to large diffusion coefficients of hydrogen in polycrystalline WO₃ thin films, compared to amorphous WO₃ thin films. Thus, the likelihood that the diffusive transport process is the rate-determining step in electrochemical measurements of amorphous WO₃ is higher. In particular, as the insertion and extraction kinetics is much faster and the porosity is higher as already discussed.^[4c,29] Assuming that the diffusion coefficient of hydrogen is determined by the independent motion of electrons and protons, the diffusion coefficient depends on the partial conductivities of electrons σ_e and protons σ_{ion} according to^[30]

$$D_H \propto \frac{\sigma_e \sigma_{ion}}{\sigma_e + \sigma_{ion}} \quad (9)$$

The conductivity of a specific charge carriers σ_i is directly linked to its diffusion coefficient D_i by the following relationship

$$\sigma_i = \frac{c_i z_i^2 F^2}{RT} D_i \quad (10)$$

Here, c_i is the molar concentration of the species, z_i is the valency, F is the Faraday constant, R is the gas constant, and T is the temperature. Since the diffusion coefficient of electrons in WO₃ is found to be several orders of magnitude higher than the diffusion coefficient of protons/hydrogen (see Table 2), the transport of protons through the lattice is expected to determine the magnitude of the transport coefficients of hydrogen. Thus, the change in the diffusion coefficient of hydrogen observed in polycrystalline WO₃ films cannot be understood in terms of an insulator-to-metal-transition often observed in WO₃ upon charge insertion.^[31] The process responsible for the change in hydrogen diffusivity needs to influence the diffusive transport of protons. This is most likely explained by the structural phase transition accompanying the insulator-to-metal-transition. The change of crystal structure aligns the WO₆ octahedral groups.^[6b,32] This alignment in turn increases the channel size and enhances diffusive transport. Another possible explanation of the observed change in diffusivity could be the competing diffusion in grains and along grain boundaries. As reported in literature, fast or even exclusive proton diffusion along grain boundaries takes place in various materials.^[33] Future investigations including the systematic variation of thin film crystallinity and morphology addressing the observed phenomenon will have to be performed to clarify the microscopic origin of the experimental findings. However, the results show that the derivation of diffusion coefficients from results gathered in electrochemical measurements not necessarily takes into account morphological details such as porosity, tortuosity or interfaces, thus making it harder to compare results from samples of different morphology. The advantage of the experimental approach presented here is that spatial and temporal information about the hydrogen distribution in WO₃ film is obtained simultaneously, which is necessary to resolve concentration-dependent diffusion processes. Moreover, data gathered in electrochemical measurements could contain contributions from side reactions. The influence of side reactions can be excluded in the approach used here. Thus, investigating diffusion processes using optical

methods is a promising way to establish a better understanding of these processes in electrochromic materials. Such an understanding is not only desirable from a fundamental point of view, but gains importance due to the intensified use of these materials in commercial devices. Results from electrochemical studies demand a more complex analysis, if concentration-dependent diffusion are present in the material.

3. Conclusion

A remarkable effect of thin film morphology on hydrogen diffusion in WO₃ thin films has been revealed. The results obtained have been discussed qualitatively and analyzed quantitatively by parameterizing the concentration-dependence of the diffusion coefficients of various samples. As a result of numerical simulations the diffusion coefficient in amorphous WO₃ has been found to decrease by two orders of magnitude as the hydrogen concentration increases. In contrast, the diffusivity of hydrogen in polycrystalline WO₃ thin films is found to increase with the concentration of hydrogen. The latter is most probably originating from changes in the crystal structure upon hydrogenation. The concentration dependent changes of hydrogen diffusivity in polycrystalline WO₃ thin films are less pronounced than in amorphous WO₃ thin films.

4. Experimental Section

Sample Preparation: Fluorine doped tin oxide (F₂SnO₂, e.g., FTO) coated glass slides with a sheet resistance of $R = 7 \Omega \text{ sq}^{-1}$ (purchased at "Sigma-Aldrich") were used as substrates. WO₃ powder (purity: 99.995%, purchased at "chemPUR GmbH") was electron beam evaporated out of a molybdenum crucible using a 100 W electron beam of a V_e-beam electron gun system (Veeco Instruments INC). At a pressure below 10⁻² Pa, ≈150 nm WO₃ were deposited onto the FTO coated surface of the water cooled substrate at a rate of 1–5 nm s⁻¹. A small area along an edge of the FTO-coated substrate was masked during WO₃ thin film deposition to retain a direct electrical contact. This area was coated with 7.2 nm chromium and 73.5 nm gold subsequently by thermal evaporation at comparable pressures and rates to enhance the quality of the electrical contact. Heating the obtained thin films at 450 °C for 1 h with a heating rate of 100 °C h⁻¹ led to a transition from amorphous WO₃ thin films to polycrystalline thin films (see Figure S1 in the Supporting Information for X-ray diffraction data). To deposit an additional microstructured film on top of the WO₃ films, 150 μL of a solution containing 4% polymethylmethacrylate (PMMA) in anisole (MicroChem Corp.) were spin coated at 3000 rpm for 45 s with a Delta6 RC spin coater (SÜSS MicroTec AG). After a subsequent heat treatment on a hot plate at 180 °C for 2 min, a PMMA film with a thickness of ≈200 nm was obtained. The PMMA film was microstructured by electron beam lithography in a modified scanning electron microscope ("JEOL JSM 7001F"). With an electron beam current of 200 pA and an acceleration voltage of 15 kV, a line pattern with a width of 50 μm across the whole sample was exposed, resulting in a 50 μm wide gap in the PMMA layer after developing the exposed sample in a mixture of isopropyl alcohol and purified water (2:1, volume ratio) for 45 s.

Electrochemical Hydrogen Insertion: Electrochemical experiments were performed using a specially designed compact electrochemical cell with a three electrode arrangement. The design was adapted from Wallys et al. and enabled the use of the samples prepared as a working electrode.^{13,41} A silver chloride (Ag/AgCl) microreference electrode, generally stored in a saturated KCl solution when not in use ($E_0 = 0.197 \text{ V}$ vs standard hydrogen electrode, "Driref-450" purchased from World Precision

Instruments), and a platinum counter electrode have been used. Diluted sulfuric acid with a concentration of 0.1 mol L⁻¹ (purchased from Sigma-Aldrich) was used as electrolyte. For the insertion of hydrogen into nonstructured samples, CV measurements have been performed. The potential was swept between -0.6 and 1.0 V versus $E_{\text{Ag/AgCl}}$ with a sweep rate of 1 mV s⁻¹ starting from the open cell potential. Hydrogen insertion into microstructured samples has been achieved by applying a constant voltage of -0.3 V versus $E_{\text{Ag/AgCl}}$ with a Jaisle IMP 83 potentiostat.

In Situ Transmission Spectroscopy: During electrochemical hydrogen insertion, the sample was illuminated with a halogen lamp. In situ transmission measurements on WO₃ thin films without an additional PMMA layer have been performed with an ASEQ LR1 compact spectrometer with a spectral resolution of about 5 nm. In the case of spatially and temporally resolved experiments, transmitted radiation was analyzed by magnifying the image of the sample with a tenfold magnification microscope objective and focusing it onto the entrance slit (0.1 mm width) of a subtractive double spectrometer (Spex 1680 b, Horiba Jobin Yvon GmbH). The spectrometer acted as a bandpass filter. It was equipped with two gratings with a groove density of 300 mm⁻¹, a blaze wavelength of 500 nm, and a blaze angle of 4.18°. It imaged the transmitted radiation with a wavelength of (637 ± 15) nm onto the ICX258AL sensor of the CCD (pco.1400, purchased from PCO AG) having a pixel size of (6.45 × 6.45) μm² and an overall size of (1392 × 1040) pixels. With this experimental setup transmitted radiation has been resolved in two spatial coordinates with a resolution of ± 0.645 μm. The best temporal resolution was determined by the time interval between acquiring two image frames with the LabVIEW software (purchased from National Instruments Corp.). The time interval comprises the integration time (50 ms) and a resting time (2 s) of the CCD.

Supporting Information

Supporting Information is available from the Wiley Online Library or from the author.

Acknowledgements

Financial support is provided by the DFG via the GRK (Research Training Group) 2204 "Substitute Materials for sustainable Energy Technologies." This article was amended on March 23, 2018 to correct Equation 8.

Conflict of Interest

The authors declare no conflict of interest.

Keywords

concentration-dependent diffusion, electrochromism, hydrogen diffusion, in situ transmission spectroscopy, tungsten trioxide

Received: December 5, 2017

Revised: December 22, 2017

Published online: January 23, 2018

[1] S. K. Deb, *Appl. Opt.* **1969**, *8*, 192.

[2] a) C. G. Granqvist, *Thin Solid Films* **2014**, *564*, 1; b) D. T. Gillaspie, R. C. Tenent, A. C. Dillon, *J. Mater. Chem.* **2010**, *20*, 9585; c) T. Tesfamichael, M. Arita, T. Boström, J. Bell, *Thin Solid Films* **2010**, *518*, 4791.

- [3] a) W.-J. Li, Z.-W. Fu, *Appl. Surf. Sci.* **2010**, 256, 2447; b) M. Sasidharan, N. Gunawardhana, M. Yoshio, K. Nakashima, *Nano Energy* **2012**, 1, 503; c) S. Yoon, S.-G. Woo, K.-N. Jung, H. Song, *J. Alloys Compd.* **2014**, 613, 187.
- [4] a) C. G. Granqvist, *Handbook of Inorganic Electrochromic Materials*, Elsevier Science B.V., Amsterdam **1995**; b) C. G. Granqvist, *Sol. Energy Mater. Sol. Cells* **2000**, 60, 201; c) K. Bange, *Sol. Energy Mater. Sol. Cells* **1999**, 58, 1.
- [5] a) S. K. Deb, *Sol. Energy Mater. Sol. Cells* **2008**, 92, 245; b) E. Broclawik, A. Góra, P. Liguzinski, P. Petelenz, H. A. Witek, *J. Chem. Phys.* **2006**, 124, 054709; c) J.-G. Zhang, D. K. Benson, C. E. Tracy, S. K. Deb, A. W. Czanderna, C. Bechinger, *J. Electrochem. Soc.* **1997**, 144, 2022; d) S.-H. Lee, M.-J. Seong, H. M. Cheong, E. Ozkan, E. C. Tracy, S. K. Deb, *Solid State Ionics* **2003**, 156, 447; e) O. F. Schirmer, E. Salje, *Solid State Commun.* **1980**, 33, 333; f) B. W. Faughnan, R. S. Crandall, M. A. Lampert, *Appl. Phys. Lett.* **1975**, 27, 275; g) L. Berggren, J. C. Jonson, G. A. Niklasson, *J. Appl. Phys.* **2007**, 102, 083538.
- [6] a) S. Darmawi, S. Burkhardt, T. Leichtweiss, D. A. Weber, S. Wenzel, J. Janek, M. T. Elm, P. J. Klar, *Phys. Chem. Chem. Phys.* **2015**, 17, 15903; b) Y. He, M. Gu, H. Xiao, L. Luo, Y. Shao, F. Gao, Y. Du, S. X. Mao, C. Wang, *Angew. Chem.* **2016**, 128, 6352; *Angew. Chem., Int. Ed.* **2016**, 55, 6244.
- [7] a) M. L. Hitchman, *Thin Solid Films* **1979**, 61, 341; b) S. K. Mohapatra, *J. Electrochem. Soc.* **1978**, 125, 284; c) B. Reichman, A. J. Bard, D. Laser, *J. Electrochem. Soc.* **1980**, 127, 647.
- [8] a) P. G. Dickens, R. J. Hurditch, *Nature* **1967**, 215, 1266; b) P. G. Dickens, D. J. Murphy, T. K. Halstead, *J. Solid State Chem.* **1973**, 6, 370.
- [9] A. Vértes, R. Schiller, *J. Appl. Phys.* **1983**, 54, 199.
- [10] a) I. Denk, F. Noll, J. Maier, *J. Am. Ceram. Soc.* **1997**, 80, 279; b) J. H. Yu, J.-S. Lee, J. Maier, *Angew. Chem., Int. Ed.* **2007**, 46, 8992; c) J. J. Kim, S. R. Bishop, N. J. Thompson, D. Chen, H. L. Tuller, *Chem. Mater.* **2014**, 26, 1374; d) D. Sugak, Y. Zhydachevskii, O. Buryy, S. Ubizskii, A. Börger, M. Schrader, K.-D. Becker, *Acta Mater.* **2008**, 56, 6310; e) O. Buryy, S. Ubizskii, I. I. Syvorotka, K.-D. Becker, *Acta Phys. Pol., A* **2010**, 117, 184.
- [11] E. R. Cohen, T. C. Vitaz, J. G. Frey, B. Holmström, K. Kuchitsu, R. Marquardt, I. Mills, F. Pavese, M. Quack, J. Stohner, H. L. Strauss, M. Takami, A. J. Thor, *Quantities, Units and Symbols in Physical Chemistry*, IUPAC & RSC Publishing, Cambridge **2008**.
- [12] a) O. F. Schirmer, V. Wittwer, G. Baur, G. Brandt, *J. Electrochem. Soc.* **1977**, 124, 749; b) R. B. Goldner, D. H. Mendelsohn, J. Alexander, W. R. Henderson, D. Fitzpatrick, T. E. Haas, H. H. Sample, R. D. Rauh, M. A. Parker, T. L. Rose, *Appl. Phys. Lett.* **1983**, 43, 1093.
- [13] D. Dini, F. Decker, E. Masetti, *J. Appl. Electrochem.* **1996**, 26, 647.
- [14] K. Miyake, H. Kaneko, M. Sano, N. Suedomi, *J. Appl. Phys.* **1984**, 55, 2747.
- [15] G. Nagy, R. Schiller, *Int. J. Hydrogen Energy* **1989**, 14, 567.
- [16] C. Bohnke, O. Bohnke, *J. Appl. Electrochem.* **1988**, 18, 715.
- [17] K. M. Karuppasamy, A. Subrahmanyam, *J. Phys. D: Appl. Phys.* **2009**, 42, 095301.
- [18] K. A. MacDonald, J. M. Bell, J. Barczynska, G. Voelkel, *Proc. SPIE* **1993**, 2017, 95.
- [19] J.-P. Randin, R. Viennet, *J. Electrochem. Soc.* **1982**, 129, 2349.
- [20] B. Reichman, A. J. Bard, D. Laser, *J. Electrochem. Soc.* **1979**, 126, 583.
- [21] O. Bohnke, M. Rezaei, B. Vuillemin, C. Bohnke, P. A. Gillet, C. Rousselot, *Sol. Energy Mater. Sol. Cells* **1992**, 25, 361.
- [22] K. Nishimura, *Solid State Commun.* **1976**, 20, 523.
- [23] L. Bóbcis, L. Szirák, G. G. Láng, *Electrochem. Commun.* **2008**, 10, 283.
- [24] X. Meng, F. Quenneville, F. Venne, E. Di Mauro, D. Işık, M. Barbosa, Y. Drolet, M. N. Natile, D. Rochefort, F. Soavi, C. Santato, *J. Phys. Chem. C* **2015**, 119, 21732.
- [25] R. S. Crandall, B. W. Faughnan, *Appl. Phys. Lett.* **1975**, 26, 120.
- [26] R.-T. Wen, C. G. Granqvist, G. A. Niklasson, *Nat. Mater.* **2015**, 14, 996.
- [27] S. Malmgren, S. V. Green, G. A. Niklasson, *Electrochim. Acta* **2017**, 247, 252.
- [28] a) J.-G. Zhang, D. K. Benson, C. E. Tracy, J. Webb, S. K. Deb, *Proc. SPIE* **1993**, 2017, 104; b) H. Kamal, A. A. Akl, K. Abdel-Hady, *Phys. B* **2004**, 349, 192.
- [29] X. Sun, Z. Liu, H. Cao, *J. Alloys Compd.* **2010**, 504S, S418.
- [30] a) J. Maier, *J. Am. Ceram. Soc.* **1993**, 76, 1213; b) H. Rickert, *Electrochemistry of Solids, An Introduction*, Springer, Berlin **1982**.
- [31] a) K. Yoshimatsu, T. Soma, A. Ohtomo, *Appl. Phys. Express* **2016**, 9, 075802; b) X. Leng, J. Pereiro, J. Strle, G. Dubuis, A. T. Bollinger, A. Gozar, J. Wu, N. Litombe, C. Panagopoulos, D. Pavuna, I. Božović, *npj Quantum Mater.* **2017**, 2, 35; c) S. G. Altendorf, J. Jeong, D. Passarello, N. B. Aetukuri, M. G. Samant, S. S. P. Parkin, *Adv. Mater.* **2016**, 28, 5284; d) S. Nishihaya, M. Uchida, Y. Kozuka, Y. Iwasa, M. Kawasaki, *ACS Appl. Mater. Interfaces* **2016**, 8, 22330.
- [32] Q. Zhong, J. R. Dahn, K. Colbow, *Phys. Rev. B* **1992**, 46, 2554.
- [33] a) R. A. De Souza, J. A. Kilner, J. F. Walker, *Mater. Lett.* **2000**, 43, 43; b) S. Kim, H. J. Avila-Paredes, S. Wang, C.-T. Chen, R. A. De Souza, M. Martin, Z. A. Munir, *Phys. Chem. Chem. Phys.* **2009**, 11, 3035; c) H. J. Avila-Paredes, C.-T. Chen, S. Wang, R. A. De Souza, M. Martin, Z. A. Munir, S. Kim, *J. Mater. Chem.* **2010**, 20, 10110; d) E. Navickas, T. M. Huber, Y. Chen, W. Hetaba, G. Holzlechner, G. Rupp, M. Stöger-Pollach, G. Friedbacher, H. Hutter, B. Yildiz, J. Fleig, *Phys. Chem. Chem. Phys.* **2015**, 17, 7659.
- [34] J. Wallys, J. Teubert, F. Furtmayr, D. M. Hofmann, M. Eickhoff, *Nano Lett.* **2012**, 12, 6180.

4.2 Charge Transport in Single NCM 111 Secondary Particles (Publication 2)

The demand for experimental access to transport properties of single secondary particles with diameters on the micrometer scale and to the dependence of these properties on size motivated the development of an appropriate measurement approach.

The idea was to immobilize single secondary particles in a way that two contacts on opposite sides could be formed. The conductivity of these contacts should allow the transport of either electrons or ions and should lead to the measurement of an ionically or electronically dominated measurement signal. The way in which single secondary particles were immobilized was developed based on existing experiences in microfabrication techniques and particle arrangement. The properties of an epoxy-based, near-UV, negative tone resist (SU-8) [220, 221], which can be patterned by photolithography and is known to be electronically insulating [222, 223] were advantageous here. Adapting the approach of earlier work published by the research group [224, 225], a mask for the fabrication of SU-8 thin films with heights in the range of the particle diameter and cylindrical openings (traps) penetrating the films at defined positions was developed. The mask was used to successfully pattern SU-8 thin films on squared glass substrates coated with copper or gold, as well as FTO-coated glass substrates for testing purposes. The pattern was designed in such a way, that the corners of a substrate with dimensions of $1\text{ cm} \times 1\text{ cm}$ would not be covered by the SU-8 thin films but remain accessible for contacting. The size of the traps was adjusted to the size of the secondary particles used for testing purposes and the demonstration of the approach. Single secondary particle measurements were expected to require a large number of experimental attempts. This was taken into account by preparing four independent particle traps on a single substrate. In order to arrange the particles in the traps, the particles were dispersed in propylene carbonate. It was chosen because of its use as a solvent in electrolytes for LIBs [196]. A “rough” arrangement of the particles on top of the patterned surface was achieved by the meniscus-force method and modified with a single-hair brush under the light microscope, if necessary. By this, particle arrangements with up to 5 different particles in a single particle trap with a diameter of $35\text{ }\mu\text{m}$ could be prepared. Secondary particles lying on top of the SU-8 surface and in the vicinity of a trap could be displaced properly. The exact arrangement was investigated with a light microscope and a corresponding picture was used to determine the size of the particles arranged.

The specially designed cell was developed and constructed to match the requirements given by the results of the microfabrication process. It was not sure at that time, whether the measurements needed to be conducted in a protective atmosphere or not. In order to ensure comparability between measurements with and without liquid electrolytes and to suppress their possible tendency to evaporate, the cell was designed to be gas-tight. A detailed description of the cell is provided in section C of the appendix. After assembling the cell, the sample containing immobilized secondary particles was contacted at defined

positions. Four copper cylinders contacted the surface of the squared substrate near its corners (bottom contact). Four more contacts to the trap areas were implemented by stainless steel cylinders with a diameter of 1 mm (top contact). In experiments, in which a metal coated glass substrate was used, the bottom part of the steel cylinders were coated with the same metal by thermal evaporation to ensure a symmetric cell configuration.

Particles with diameters exceeding the height of the SU-8 film were contacted by two metal planes on opposite sides and plastically deformed. The degree of plastic deformation was determined by the height of the SU-8 film and the diameter of the particle. The mechanical properties of the latter also influenced the morphology of the plastically deformed particle. This deformation, certainly being an aspect to improve, was necessary to obtain a well-defined contact area. To investigate the influence of this plastic deformation, a modified version of the contact-forming part was developed and constructed, which allows the successive increase of the load applied by the steel cylinder. However, for the sake of comparability, results on which this publication is based on, were obtained by experiments with the first version of the cell. Experimental data was restricted to data obtained from particles, which could be identified under the light microscope after disassembling the cell.

The measurement signals employed for the investigation of charge transport in single particles were obtained by cyclic voltammetry, i.e. the acquisition of current-voltage curves, chronoamperometric, and -potentiometric measurements and impedance spectroscopy. The measurement configuration comprising ionically blocking contact materials allowed the interpretation of the impedance spectra in terms of resistances describing ionic and electronic charge transport. The values for both resistances were obtained by simulating the impedance of an equivalent circuit and fitting it to experimental impedance data. The resistances describing electronic charge transport were found to correlate with the size of the particles. A model describing such a correlation [226, 227] was employed to develop a fitting routine. The good agreement between simulated and experimental data motivated to proceed similarly with the values obtained for the resistances describing ionic charge transport. Their correlation with the size of the secondary particles was less pronounced compared to the correlation of resistances describing electronic charge transport. During the submission process, “R-values” for the quantification of the fits were requested. These were calculated based on the definition of R_1^2 in [228], considering that the logarithm of the resistances were used to minimize the deviation between simulated and measured resistance values.

The manuscript was written by me and edited by all the co-authors. The preparation of the NCM 111 secondary particles was carried out by N. Bohn, A. C. Wagner, and J. R. Binder at the Institute for Applied Materials (IAM-EES) (Karlsruher Institute of Technology). The microfabrication process was developed by me, M. T. Elm, and P. J. Klar, and optimized in project works of J. K. Eckhardt and M. S. Friedrich, who also conducted the experiments that produced the data on which the publication is based on. The electrochemical cell employed for single particle measurements was developed by me in collaboration with T. Wasem. Several SEM investigations were conducted by M. S.

Friedrich, and me, as well as M. Osenberg at the Department of Materials Science and Technology (Technische Universität Berlin), who also conducted FIB-SEM tomography on two particles after being measured. Raman experiments were carried out by L. Chen, profilometric investigations of the sample surface by me. The simulation of the impedance of an equivalent circuit and the fitting to measured impedances of single particles was done by me using the software RelaxIS 3 (version 3.0.11.12, rhd instruments GmbH & Co. KG, Otto-Hesse-Str. 19 / T3, D-64293 Darmstadt). The simulation of ionic and electronic resistances as a function of the particle radius, as well as the implementation of a fitting routine in the software “Wolfram Mathematica[®]” (version 11.2.0.0., Wolfram Research, Inc., 100 Trade Center Drive, Champaign, IL 61820-7237, USA) was carried out by me. The article is reprinted with permission from *ACS Energy Letters*, **2019**, *4* (9), 2117–2123. (DOI: <https://doi.org/10.1021/acsenergylett.9b01579>)

Copyright © 2019 American Chemical Society


Charge Transport in Single NCM Cathode Active Material Particles for Lithium-Ion Batteries Studied under Well-Defined Contact Conditions

Simon Burkhardt,^{†,‡} Markus S. Friedrich,^{†,‡} Janis K. Eckhardt,^{†,‡} Amalia C. Wagner,[§] Nicole Bohn,[§] Joachim R. Binder,[§] Limei Chen,^{†,‡} Matthias T. Elm,^{†,‡,||} Jürgen Janek,^{‡,||} and Peter J. Klar^{*,†,‡,||}

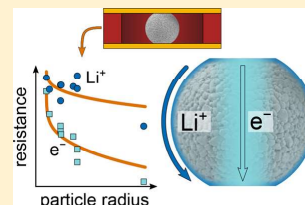
[†]Institute of Experimental Physics I and [‡]Center for Materials Research (LaMa), Justus Liebig University Giessen, Heinrich-Buff-Ring 16, 35392 Giessen, Germany

[§]Institute for Applied Materials (IAM-ESS), Karlsruher Institute of Technology, Hermann-von-Helmholtz-Platz 1, 76344 Eggenstein-Leopoldshafen, Germany

^{||}Institute of Physical Chemistry, Justus Liebig University Giessen, Heinrich-Buff-Ring 17, 35392 Giessen, Germany

 Supporting Information

ABSTRACT: We present a technique for systematically investigating electronic and ionic charge transport in single $\text{Li}(\text{Ni}_{1/3}\text{Co}_{1/3}\text{Mn}_{1/3})\text{O}_2$ (NCM 111) secondary particles as a function of size. We perform electrochemical impedance spectroscopy employing ion-blocking electrodes. Micrometer-sized spherical particles are arranged in cylindrical particle traps on a patterned substrate. A specially designed electrochemical cell is used to contact and measure individual immobilized particles in a defined contact geometry. The obtained electronic and ionic resistances of the particles as a function of size are compared with model calculations based on a homogeneous sphere with finite contact areas. The modeling reveals that electronic transport mainly occurs in the bulk of the NCM 111 particles, whereas ionic transport takes place along the particle surface. The extracted material parameters are in good agreement with literature values, showing the reliability of our measurement technique and its potential for systematic studies on the single-particle level.



High demand for high-performance batteries in, e.g., mobile electronic devices, large-scale energy storage, or electric vehicles, has led to a diversification of battery systems. Today's state-of-the-art battery technology in portable applications and electric vehicles is the lithium-ion battery (LIB). It consists of a graphite-based anode, a liquid electrolyte, and a composite cathode as electrochemical key components; current collectors, separator, and various additives complement the cell components. The cathode is mainly composed of the cathode active material (CAM), conducting carbon additive, and a polymer binder.¹ Energy and power density as well as cycle lifetimes of CAMs used today, e.g., $\text{Li}_{1-x}(\text{Ni}_y\text{Co}_z\text{Mn}_{1-y-z})\text{O}_2$ (NCM) or $\text{Li}_{1-x}(\text{Ni}_y\text{Co}_z\text{Al}_{1-y-z})\text{O}_2$ (NCA), still require optimization^{2–4} to comply with future energy demands.^{5,6} Furthermore, the extensive use of NCM and NCA is critical with respect to natural resources of cobalt and nickel compromising mass production at low cost. Approaches to improve energy and power density without changing to “beyond Li-ion battery” concepts, such as Li–air or Li–S technologies, are, e.g., “excess metal CAMs”,^{7–12} coatings for cathode materials,^{13–17} all-

solid-state LIBs,^{18–23} or optimizing the architecture of CAMs toward hierarchically structured and porous networks of primary particles.^{24–26}

All these approaches have the characterization and optimization of particulate matter in common, which is usually carried out empirically by investigating the performance of composite electrodes in half or full-cell setups. Such approaches yield easy access to effective characteristics of the composite as a whole, e.g., specific energy density, capacity retention, or cycle lifetime. However, as the interplay of material components and the microstructure of the composite electrode determine its effective properties,^{27–56} the individual contributions of its components or of interfaces and interphases formed between them cannot be easily separated. Little can be learned about the intrinsic properties of the CAM within the composite electrode, e.g., effects of size of primary

Received: July 23, 2019

Accepted: August 9, 2019

Published: August 9, 2019

and secondary CAM particles or of network formation. A systematic investigation of the fundamental microscopic processes taking place in the CAM during cycling is necessary to reach a higher level of optimization. The identification and understanding of structural limitations on different length scales are crucial for optimizing the properties of CAMs and finally composite cathodes in a controlled manner.

Different strategies for studying charge transport in CAM particles have been reported in the literature. One is the investigation of macroscopic ensembles like pellets of compacted CAM particles^{57–60} or CAM powders,⁶¹ which yields average properties of bulk and grain boundaries of a polycrystalline CAM sample only. Moreover, the porosity of pressed pellets is often below 5%^{58,59} while the porosity of secondary CAM particles used in composite cathodes lies between 5% and 50%. Because porosity may influence charge transport^{62–65} or mechanical properties⁶⁶ significantly, values obtained from experiments using macroscopic ensembles are only to some extent representative for composite cathodes.⁶⁷ Measurements on single CAM particles actually employed in the composite cathodes are mandatory to determine a realistic dependence of charge transport properties on size. This holds especially for hierarchical structures, where effects of the primary particle network are always present and the secondary particles exhibit an often not well-characterized size distribution. Most of the single-particle measurements reported were performed on single particles placed on top of an electrolyte-soaked separator and contacted using a platinum or gold wire sealed in a glass tube.^{68–76} Another approach reported is the attachment of a single particle to a current-collecting micromanipulator using metal deposition in a focused ion beam scanning electron microscopy (FIB-SEM) system and performing electrochemical measurements employing a low-vapor-pressure electrolyte inside a SEM instrument⁷⁷ or a standard liquid electrolyte inside a glovebox.⁷⁸ Further reports are based on contacting single particles with a conducting tip of an atomic force microscope,⁷⁹ combining a scanning micropipette contact method with SEM,⁸⁰ or immobilizing a single particle between a gold micro disc electrode and a glass pressing tool and immersing this ensemble in a liquid electrolyte.⁸¹ All these approaches have at least one aspect in common that prevents the discrimination of ionic and electronic charge transport in the single particles as a function of size. Because of the use of liquid electrolytes, asymmetric contacting, ill-defined point-contacts, or nonideally ion-blocking electrode materials, ion and electron transport can hardly be distinguished. These experiments only offer the electrochemical response of a single particle in combination with a very small and poorly defined contact to the current collector. Conclusions drawn from these experiments depend on assumptions concerning the influence of the contact on rate-limiting processes, which also may explain the lack of reports on the separation of electronic and ionic charge transport in single CAM particles. Indeed, no studies on mixed conduction in single CAM particles could be found during extensive literature research, even though such information is crucial for theoretical studies and simulations of the performance of composite cathodes in batteries.^{82–84} In contrast, the experimental approach presented here allows measuring the impedance of single particles between symmetric and selectively blocking electrodes. By using this method for the investigation of mixed charge transport in single Li(Ni_{1/3}Co_{1/3}Mn_{1/3})O₂ (NCM 111) secondary particles, evi-

dence for preferred conduction pathways of electrons and ions is revealed for the first time. Instead of using microelectrodes, we present an alternative novel approach for investigating ionic and electronic transport in single NCM 111 secondary particles. Despite NCM 622 and materials with higher Ni content becoming state-of-the-art, NCM 111 is still an important CAM in present LIBs, and values of its electronic and ionic conductivities are reported in the literature; therefore, it serves as a suitable model system to validate the approach presented.

In this approach, individual secondary particles are immobilized in traps patterned into an insulating SU-8 layer and then electrically contacted by macroscopic contact pins in a capacitor-like arrangement yielding a well-defined contact configuration. A microfabrication process combined with a variant of the meniscus-force deposition method was used to prepare cylindrical openings in the SU-8 layer for trapping the particles (see Figure 1a and Experimental Section in the Supporting Information). Four cylindrical particle traps each having a diameter of 35 μm and each completely penetrating the SU-8 layer to a metallic contact were fabricated on top of a glass substrate. A top view of a particle trap filled with a single secondary particle is depicted in Figure 1c. Transport experiments were conducted using the specially designed cell; its top part is shown in Figure 1b. The pressure caused by the two contacting planes deforms the secondary particles to some extent, as shown in Figure 1d. Sometimes even cracks may arise, which can be detected by optical inspection.

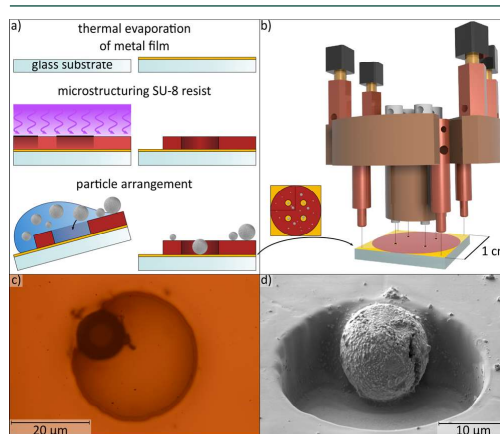


Figure 1. Scheme of the sample preparation process comprising metal film deposition, microstructuring SU-8 resist, and particle arrangement via the meniscus force method (a); photorealistic image of the contact forming part of the specially designed cell (b); image of a single secondary particle in a particle trap recorded under a light microscope (c); SEM image of the same secondary particle after electrochemical measurements (d).

Impedances of various secondary particles with radii between 6 and 16 μm were measured with an AC amplitude of 50 mV. Experimental values of the impedances of three secondary particles with different radii, as well as spectra, calculated on the basis of an equivalent circuit (see Figure 3a) are shown in Figure 2.

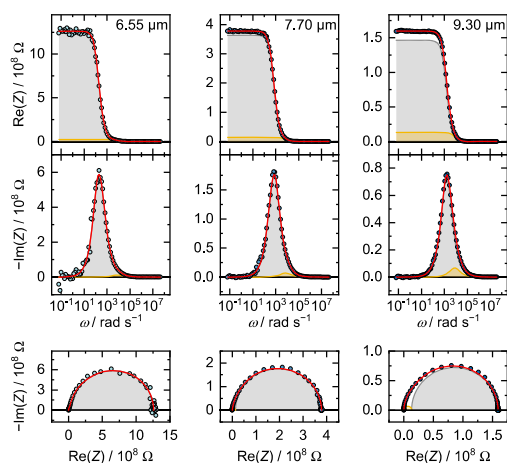


Figure 2. Overview of plots of measured (filled circles) and simulated (straight lines) impedances of various secondary particles of three different radii. The low-frequency resistance decreases with increasing radius. Each column depicts Bode and Nyquist plots for one particle radius.

In all measurements, the impedance of single NCM 111 secondary particles is dominated by a large ohmic resistance in the low-frequency region of the spectra (gray), which decreases with increasing particle radius. Additionally, a second transport process can be distinguished, which contributes to the impedance at a frequency of approximately 10^4 rad s^{-1} (yellow). This transport process has also been observed in the absence of NCM 111 secondary particles between the metal electrodes (see Figure S1 in the Supporting Information).

The equivalent circuit accounting for the two transport processes observed and used for fitting the impedance spectra is depicted in Figure 3a. The impedance representing the first transport process (gray) and assigned to the actual sample consists of three contributions connected in parallel: the electronic charge transport (e), the ionic charge transport (i) including ion blockage at the metal contacts, and the geometric capacitance (g) due to dielectric polarization of all different materials between the metal contacts. This equivalent circuit is typically used for describing the impedance of a mixed ion–electron conductor between ion-blocking electrodes.^{85,86} The second circuit (s) corresponding to the second transport process (yellow) represents the measurement system connected to the sample.

Here, the resistances R_i and R_e describe the ionic and electronic charge transport through the entire volume between the metal contacts, which contain the SU-8 layer surrounding the trap and defining the contact distance as well as the NCM 111 secondary particle inside the trap in an argon atmosphere (corresponding to the atmosphere in the glovebox where the measurements were performed). As proved in Figure S1, R_i and R_e are fully determined by the NCM 111 secondary particle as it possesses much better ionic and electronic conductivities than SU-8 or argon. Thus, the resistances R_i and R_e represent averages arising from the bulk and grain boundary resistances of the primary particle network. The capacitor C_i connected in series with R_i describes the

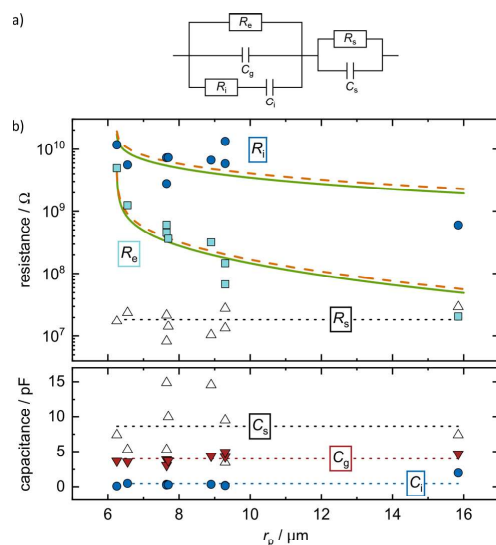


Figure 3. Equivalent circuit used for fitting the impedance spectra of single NCM 111 secondary particles (a) and the obtained resistances and capacitances as a function of the particle radius (b). Dotted lines are guides to the eye only; straight and dashed lines represent results of a least-squares fitting procedure using the model of a homogeneous conducting sphere described in the text.

accumulation of lithium ions at the interfaces between the metal electrodes and the NCM 111 secondary particle, as lithium ions cannot penetrate into the ion-blocking metal electrodes. No capacitor is included in the electronic branch as all electrons may enter the metal electrodes. The capacitor C_g in parallel to the electronic and ionic branches describes the dielectric polarization response of the materials between both metal electrodes, which plays a role at higher frequencies. The dielectric polarization of the SU-8 layer, Ar, and the NCM 111 secondary particle contribute to this so-called geometric capacitance. The resistance R_s as well as the capacitor C_s describe the impedance response of the measurement system. The impedance spectra obtained from single secondary particles with different radii have been fitted based on this equivalent circuit. The optimized values for the different parameters as a function of the secondary particles' radii are depicted in Figure 3b.

The ionic resistance R_i is the largest resistance of the secondary particles at all radii r_p , indicating that the ionic conductivity is lower than the electronic conductivity in this NCM 111 material. The reports in literature concerning the dominant type of carrier in NCM 111 vary considerably. Either electronic⁵⁸ or ionic⁵⁹ conductivity may be dominant depending on the degree of delithiation of the material.⁵⁸ Here, both resistances R_i and R_e decrease with increasing radius of the secondary particle. However, this effect is less pronounced for the ionic resistance R_i . An increase of the contact area between particle and contact is the main origin of this effect. As will be shown below, the electronic transport takes place via the bulk of the secondary particle, whereas the ionic current is more likely to flow along the surface, rather than through the bulk of the material. The resistance R_s assigned to the measurement

system is always smaller than the ionic and electronic resistances of the NCM 111 secondary particles except for the largest secondary particle, justifying the experimental approach. To additionally verify the results gathered from impedance spectroscopy, DC polarization measurements of a single secondary particle were performed subsequently after measuring the impedance (see the [Supporting Information](#) for experimental details and results). The DC resistance $R_{DC} = (144 \pm 2) \text{ M}\Omega$ deviates less than 10% from the low-frequency impedance $R_{low\text{-}freq} = (159.6 \pm 0.6) \text{ M}\Omega$ of the same secondary particle. This deviation is acceptable, taking into account that the measured currents are in the range of several nanoamperes, which is close to the current resolution limit of the potentiostat used. The geometric capacitance C_g is virtually constant, fluctuating between 3.5 pF and 5 pF. Considering the dimensions of the plate capacitor built by assembling the electrochemical cell, C_g is expected to be dominated by the SU-8 layer, which covers more than 99.8% of the area between the metal electrodes. Assuming an average SU-8 polymer layer thickness of 10 μm and values of 3.5,⁸⁷ 1,⁸⁸ and approximately 50 ± 15 for the relative permittivity of SU-8, argon, and the NCM 111 material, respectively, indicates that only negligible contributions of argon and the secondary particles to the total geometric capacitance are expected. (The permittivity of NCM 111 has been investigated using pressed and sintered pellets. A comprehensive study of all the experimental information gathered from experiments on pressed and sintered pellets as well as a comparison between these and results from single-particle measurements will be published elsewhere.)

The geometrical model for describing the transport through the secondary particles theoretically (see the [Supporting Information](#)) is based on a homogeneous sphere truncated on top and bottom to yield finite contact areas. Essentially, three model parameters are used in the fitting procedure: the contact area size as a parameter determined by the measurement geometry and two material parameters, a surface resistance (R_{surf}) and a bulk resistivity (ρ_{bulk}). The secondary particle's internal structure consisting of a porous network of primary particles is neglected. Despite its simplicity and significant scattering of the data points, the model well reproduces the observed size dependence of ionic and electronic resistances R_i and R_e . Simultaneous least-squares fitting of $R_e(r_p)$ and $R_i(r_p)$ with resulting coefficients of determination (R^2) of 86.87% and 37.04%, respectively, yields $\rho_{e,bulk} = (4.17 \pm 0.01) \text{ k}\Omega\text{m}$ and $R_{e,surf} > 100 \text{ T}\Omega$ for NCM 111. The values should be considered as effective material parameters for the porous network of primary particles. Excluding the data obtained from the largest secondary particle with $r_p = 15.85 \mu\text{m}$ in the fitting procedure (dashed orange line in [Figure 3b](#)) slightly increases the bulk resistivity to $\rho_{e,bulk} = (4.78 \pm 0.01) \text{ k}\Omega\text{m}$. The mean of both values of $\rho_{e,bulk}$ is equivalent to an effective electronic bulk conductivity of $\sigma_{e,bulk} = (2.25 \pm 0.15) \mu\text{S cm}^{-1}$. The electronic conductivity data at room temperature reported for NCM 111 with different degrees of lithiation vary between 0.0245 and $3.2 \mu\text{S cm}^{-1}$ for fully lithiated NCM 111^{4,58,59} and are reported to increase up to 6.14 mS cm^{-1} upon delithiation.⁵⁸ Thus, the value determined for the electronic bulk conductivity of the secondary particles ($2.25 \mu\text{S cm}^{-1}$) is in good agreement with the ones reported for fully lithiated NCM 111. The ionic surface resistance $R_{i,surf}$ obtained is $(14.9 \pm 0.1) \text{ G}\Omega$. Excluding the data obtained from the largest secondary particle yields $(17.5 \pm 0.1) \text{ G}\Omega$ for the ionic surface resistance. Though the

interpretation of the surface resistance in terms of the ionic surface conductivity requires more detailed information about the properties of the surface, we estimate a surface conductivity by assuming that charge transport along the surface takes place in a spherical shell of a thickness d of 10 nm. The mean ionic surface resistance of $R_{i,surf} = 16.2 \text{ G}\Omega$ then corresponds to effective ionic surface conductivities between 10 and $50 \mu\text{S cm}^{-1}$, depending on the contact angle (see the [Supporting Information](#)). The results of this estimation are reasonable in view of results on lithium-ion conductivity of surface layers like Li_2CO_3 that are known to be formed on NCM 111 surfaces, as will be discussed below. The values for the effective electronic surface resistance ($R_{e,surf}$) as well as for the effective ionic bulk resistivity ($\rho_{i,bulk}$) of NCM 111 did not converge in the modeling. Within the model employed, this indicates that both currents flowing along the surface and through the bulk of the secondary particle differ by several orders of magnitude. Therefore, we tentatively assign the surface current to the ionic current and the bulk current to be arising from electronic charge carriers in the secondary particle in agreement with recent results on $\text{Li}(\text{Ni}_{0.98}\text{Co}_{0.01}\text{Mn}_{0.01})\text{O}_2$.⁸⁹ The ionic surface conductivity can either be attributed to the surface of NCM 111 secondary particles itself or be a property of a surface layer, which, as is well-known, may be present on CAMs because of reactions involving propylene carbonate⁹⁰ or the atmosphere containing carbon dioxide, water, and oxygen.^{91–94} We have taken Raman spectra of single NCM 111 secondary particles prior to and after the impedance measurement (see [Figure S4](#) in the [Supporting Information](#)). The spectra do not reveal any changes at the surface of the secondary particles. Nevertheless, this finding cannot entirely rule out the formation of a surface layer such as lithium carbonate^{92,93,95} or mixed hydrous carbonate hydroxides containing nickel⁹⁴ during synthesis, storage, or impedance measurements as the Raman cross section of the corresponding material may be very low and its Raman features very broad, in particular, in the case of amorphous materials. Such surface layers could explain the ionic surface conductivity as lithium carbonate, for example, is a Li-ion conductor,^{96–98} with a lithium-ion conductivity varying between $1 \mu\text{S cm}^{-1}$ ⁹⁹ and 0.4 nS cm^{-1} ¹⁰⁰ at 300 K.

The average height of the SU-8 layer deduced from the least-squares fitting is $12.48 \mu\text{m}$, which is close to the diameter of the smallest secondary particle and in good agreement with results from profilometric measurements (see [Figure S5](#) in the [Supporting Information](#)).

In summary, we present a novel and successful approach for investigating the electric properties of single NCM 111 secondary particles and for revealing preferred transport paths for electrons and ions, which in this case are different for both charge carriers. This approach is not restricted to NCM secondary particles but comprises a very versatile tool for investigating charge transport in any type of particles with sizes in the micrometer range. The well-defined measurement geometry yields the possibility of adding a thin separator soaked with liquid electrolyte and placed on top of the particle. In this way, different half-cell configurations employing a single CAM particle as cathode can be realized easily, enabling the electrochemical characterization of single particles as a function of size using the same measurement system.

■ ASSOCIATED CONTENT

■ Supporting Information

The Supporting Information is available free of charge on the ACS Publications website at DOI: 10.1021/acseenergylett.9b01579.

Details on experimental methods, different contributions to measured impedance, DC polarization of a single secondary particle, modeling of size-dependent resistances, interpretation of the surface resistance, results from Raman spectroscopy, and profilometric investigations of the sample surface (PDF)

■ AUTHOR INFORMATION

Corresponding Author

*E-mail: peter.j.klar@physik.uni-giessen.de. Phone: +49 641 9933190.

ORCID

Matthias T. Elm: 0000-0001-7014-5772

Jürgen Janek: 0000-0002-9221-4756

Peter J. Klar: 0000-0002-4513-0330

Notes

The authors declare no competing financial interest.

■ ACKNOWLEDGMENTS

Financial support is provided by the DFG via the GRK (Research Training Group) 2204 “Substitute Materials for sustainable Energy Technologies” as well as the German Federal Ministry for Economic Affairs and Energy (BMWi) granted through Project Management Jülich (03ET6095A, 03ET6095D). We thank Markus Osenberg (Department of Materials Science and Technology, Technische Universität Berlin) for experimental information gathered by FIB-SEM tomography, as well as SEM investigations and images.

■ REFERENCES

- Orikasa, Y.; Gogyo, Y.; Yamashige, H.; Katayama, M.; Chen, K.; Mori, T.; Yamamoto, K.; Masese, T.; Inada, Y.; Ohta, T.; et al. Ionic Conduction in Lithium Ion Battery Composite Electrode Governs Cross-Sectional Reaction Distribution. *Sci. Rep.* **2016**, *6*, 26382.
- de Biasi, L.; Kondrakov, A. O.; Geßwein, H.; Brezesinski, T.; Hartmann, P.; Janek, J. Between Scylla and Charybdis: Balancing Among Structural Stability and Energy Density of Layered NCM Cathode Materials for Advanced Lithium-Ion Batteries. *J. Phys. Chem. C* **2017**, *121* (47), 26163–26171.
- Kondrakov, A. O.; Schmidt, A.; Xu, J.; Geßwein, H.; Mönig, R.; Hartmann, P.; Sommer, H.; Brezesinski, T.; Janek, J. Anisotropic Lattice Strain and Mechanical Degradation of High- and Low-Nickel NCM Cathode Materials for Li-Ion Batteries. *J. Phys. Chem. C* **2017**, *121* (6), 3286–3294.
- Noh, H.-J.; Youn, S.; Yoon, C. S.; Sun, Y.-K. Comparison of the Structural and Electrochemical Properties of Layered $\text{Li}[\text{Ni}_x\text{Co}_y\text{Mn}_z]\text{O}_2$ ($x = 1/3, 0.5, 0.6, 0.7, 0.8$ and 0.85) Cathode Material for Lithium-Ion Batteries. *J. Power Sources* **2013**, *233*, 121–130.
- Luntz, A. Beyond Lithium Ion Batteries. *J. Phys. Chem. Lett.* **2015**, *6* (2), 300–301.
- Turcheniuk, K.; Bondarev, D.; Singhal, V.; Yushin, G. Ten Years Left to Redesign Lithium-Ion Batteries. *Nature* **2018**, *559*, 467–471.
- Min, K.; Jung, C.; Ko, D.-S.; Kim, K.; Jang, J.; Park, K.; Cho, E. High-Performance and Industrially Feasible Ni-Rich Layered Cathode Materials by Integrating Coherent Interphase. *ACS Appl. Mater. Interfaces* **2018**, *10* (24), 20599–20610.
- Xia, Y.; Zheng, J.; Wang, C.; Gu, M. Designing Principle for Ni-Rich Cathode Materials with High Energy Density for Practical Applications. *Nano Energy* **2018**, *49*, 434–452.
- Wang, D.; Xu, T.; Li, Y.; Pan, D.; Lu, X.; Hu, Y.-S.; Dai, S.; Bai, Y. Integrated Surface Functionalization of Li-Rich Cathode Materials for Li-Ion Batteries. *ACS Appl. Mater. Interfaces* **2018**, *10* (48), 41802–41813.
- Zuo, Y.; Li, B.; Jiang, N.; Chu, W.; Zhang, H.; Zou, R.; Xia, D. A High-Capacity O_2 -Type Li-Rich Cathode Material with a Single-Layer Li_2MnO_3 Superstructure. *Adv. Mater.* **2018**, *30* (16), 1707255.
- Yang, Z.; Zhong, J.; Li, J.; Liu, Y.; Niu, B.; Kang, F. Li-Rich Layered Oxide Coated by Nanoscale MoO_x Film with Oxygen Vacancies and Lower Oxidation State as a High-Performance Cathode Material. *Ceram. Int.* **2019**, *45* (1), 439–448.
- Assat, G.; Tarascon, J.-M. Fundamental Understanding and Practical Challenges of Anionic Redox Activity in Li-Ion Batteries. *Nat. Energy* **2018**, *3* (5), 373–386.
- Sinha, N. N.; Munichandraiah, N. Synthesis and Characterization of Carbon-Coated $\text{LiNi}_{1/3}\text{Co}_{1/3}\text{Mn}_{1/3}\text{O}_2$ in a Single Step by an Inverse Microemulsion Route. *ACS Appl. Mater. Interfaces* **2009**, *1* (6), 1241–1249.
- Cho, W.; Kim, S.-M.; Song, J. H.; Yim, T.; Woo, S.-G.; Lee, K.-W.; Kim, J.-S.; Kim, Y.-J. Improved Electrochemical and Thermal Properties of Nickel Rich $\text{LiNi}_{0.6}\text{Co}_{0.2}\text{Mn}_{0.2}\text{O}_2$ Cathode Materials by SiO_2 Coating. *J. Power Sources* **2015**, *282*, 45–50.
- Mohanty, D.; Dahlberg, K.; King, D. M.; David, L. A.; Sefat, A. S.; Wood, D. L.; Daniel, C.; Dhar, S.; Mahajan, V.; Lee, M.; et al. Modification of Ni-Rich FCG NMC and NCA Cathodes by Atomic Layer Deposition: Preventing Surface Phase Transitions for High-Voltage Lithium-Ion Batteries. *Sci. Rep.* **2016**, *6*, 26532.
- Zhou, P.; Zhang, Z.; Meng, H.; Lu, Y.; Cao, J.; Cheng, F.; Tao, Z.; Chen, J. SiO_2 -Coated $\text{LiNi}_{0.915}\text{Co}_{0.075}\text{Al}_{0.01}\text{O}_2$ Cathode Material for Rechargeable Li-Ion Batteries. *Nanoscale* **2016**, *8* (46), 19263–19269.
- Zuo, D.; Tian, G.; Li, X.; Chen, D.; Shu, K. Recent Progress in Surface Coating of Cathode Materials for Lithium Ion Secondary Batteries. *J. Alloys Compd.* **2017**, *706*, 24–40.
- Kotobuki, M.; Kanamura, K.; Sato, Y.; Yoshida, T. Fabrication of All-Solid-State Lithium Battery with Lithium Metal Anode Using Al_2O_3 -Added $\text{Li}_7\text{La}_3\text{Zr}_2\text{O}_{12}$ Solid Electrolyte. *J. Power Sources* **2011**, *196*, 7750–7754.
- Kato, Y.; Hori, S.; Saito, T.; Suzuki, K.; Hirayama, M.; Mitsui, A.; Yonemura, M.; Iba, H.; Kanno, R. High-Power All-Solid-State Batteries Using Sulfide Superionic Conductors. *Nat. Energy* **2016**, *1*, 16030.
- Patil, A.; Patil, V.; Shin, D. W.; Choi, J.-W.; Paik, D.-S.; Yoon, S.-J. Issue and Challenges Facing Rechargeable Thin Film Lithium Batteries. *Mater. Res. Bull.* **2008**, *43* (8), 1913–1942.
- Sakuda, A.; Hayashi, A.; Tatsumisago, M. Sulfide Solid Electrolyte with Favorable Mechanical Property for All-Solid-State Lithium Battery. *Sci. Rep.* **2013**, *3*, 2261.
- Wang, D.; Sun, Q.; Luo, J.; Liang, J.; Sun, Y.; Li, R.; Adair, K.; Zhang, L.; Yang, R.; Lu, S.; et al. Mitigating the Interfacial Degradation in Cathodes for High-Performance Oxide-Based Solid-State Lithium Batteries. *ACS Appl. Mater. Interfaces* **2019**, *11* (5), 4954–4961.
- Ates, T.; Keller, M.; Kulisch, J.; Adermann, T.; Passerini, S. Development of an All-Solid-State Lithium Battery by Slurry-Coating Procedures Using a Sulfidic Electrolyte. *Energy Storage Mater.* **2019**, *17*, 204–210.
- Huang, J.; Ge, H.; Li, Z.; Zhang, J. An Agglomerate Model for the Impedance of Secondary Particle in Lithium-Ion Battery Electrode. *J. Electrochem. Soc.* **2014**, *161* (8), E3202–E3215.
- Sun, G.; Sui, T.; Song, B.; Zheng, H.; Lu, L.; Korsunsky, A. M. On the Fragmentation of Active Material Secondary Particles in Lithium Ion Battery Cathodes Induced by Charge Cycling. *Extrem. Mech. Lett.* **2016**, *9*, 449–458.
- Chen, Z.; Wang, J.; Chao, D.; Baikie, T.; Bai, L.; Chen, S.; Zhao, Y.; Sum, T. C.; Lin, J.; Shen, Z. Hierarchical Porous $\text{LiNi}_{1/3}\text{Co}_{1/3}\text{Mn}_{1/3}\text{O}_2$ Nano-/Micro Spherical Cathode Material: Minimized Cation Mixing and Improved Li^+ Mobility for Enhanced Electrochemical Performance. *Sci. Rep.* **2016**, *6*, 25771.

- (27) Jang, D. H.; Shin, Y. J.; Oh, S. M. Dissolution of Spinel Oxides and Capacity Losses in 4 V Li/Li_xMn₂O₄ Cells. *J. Electrochem. Soc.* **1996**, *143* (7), 2204–2211.
- (28) Dominko, R.; Gaberscek, M.; Drogenik, J.; Bele, M.; Pejovnik, S.; Jamnik, J. The Role of Carbon Black Distribution in Cathodes for Li Ion Batteries. *J. Power Sources* **2003**, *119–121*, 770–773.
- (29) Wang, Q.; Su, F.; Tang, Z.; Ling, G.; Yang, Q. Synergetic Effect of Conductive Additives on the Performance of High Power Lithium Ion Batteries. *New Carbon Mater.* **2012**, *27* (6), 427–432.
- (30) Zheng, H.; Yang, R.; Liu, G.; Song, X.; Battaglia, V. S. Cooperation between Active Material, Polymeric Binder and Conductive Carbon Additive in Lithium Ion Battery Cathode. *J. Phys. Chem. C* **2012**, *116* (7), 4875–4882.
- (31) Nakamura, T.; Okano, S.; Yaguma, N.; Morinaga, Y.; Takahara, H.; Yamada, Y. Electrochemical Performance of Cathodes Prepared on Current Collector with Different Surface Morphologies. *J. Power Sources* **2013**, *244*, 532–537.
- (32) Xu, J.; Chou, S.-L.; Gu, Q.-F.; Liu, H.-K.; Dou, S.-X. The Effect of Different Binders on Electrochemical Properties of Li-Ni_{1/3}Mn_{1/3}Co_{1/3}O₂ Cathode Material in Lithium Ion Batteries. *J. Power Sources* **2013**, *225*, 172–178.
- (33) Zhao, D.; Feng, Y.; Wang, Y.; Xia, Y. Electrochemical Performance Comparison of LiFePO₄ Supported by Various Carbon Materials. *Electrochim. Acta* **2013**, *88*, 632–638.
- (34) Bauer, W.; Nötzel, D. Rheological Properties and Stability of NMP Based Cathode Slurries for Lithium Ion Batteries. *Ceram. Int.* **2014**, *40* (3), 4591–4598.
- (35) Chang, Y.-C.; Peng, C.-T.; Hung, I.-M. Effects of Particle Size and Carbon Coating on Electrochemical Properties of LiFePO₄/C Prepared by Hydrothermal Method. *J. Mater. Sci.* **2014**, *49* (20), 6907–6916.
- (36) Han, Z.; Zhan, H.; Zhou, Y. Preparation and Performance of Layered Li[L_{0.182}Ni_{0.182}Co_{0.091}Mn_{0.543}]O₂ Cathode with Different Binders. *Mater. Lett.* **2014**, *114*, 48–51.
- (37) Lee, S.; Kim, E.-Y.; Lee, H.; Oh, E.-S. Effects of Polymeric Binders on Electrochemical Performances of Spinel Lithium Manganese Oxide Cathodes in Lithium Ion Batteries. *J. Power Sources* **2014**, *269*, 418–423.
- (38) Zhang, Z.; Zeng, T.; Lai, Y.; Jia, M.; Li, J. A Comparative Study of Different Binders and Their Effects on Electrochemical Properties of LiMn₂O₄ Cathode in Lithium Ion Batteries. *J. Power Sources* **2014**, *247*, 1–8.
- (39) Guy, D.; Lestriez, B.; Bouchet, R.; Gaudefroy, V.; Guyomard, D. Tailoring the Binder of Composite Electrode for Battery Performance Optimization. *Electrochem. Solid-State Lett.* **2005**, *8* (1), A17–A21.
- (40) Bauer, W.; Nötzel, D.; Wenzel, V.; Nirschl, H. Influence of Dry Mixing and Distribution of Conductive Additives in Cathodes for Lithium Ion Batteries. *J. Power Sources* **2015**, *288*, 359–367.
- (41) Bockholt, H.; Haselrieder, W.; Kwade, A. Intensive Powder Mixing for Dry Dispersing of Carbon Black and Its Relevance for Lithium-Ion Battery Cathodes. *Powder Technol.* **2016**, *297*, 266–274.
- (42) Su, X.; Ha, S.; Ishwait, M. B.; Lei, H.; Oljaca, M.; Blizanac, B.; Dees, D.; Lu, W. Nonlinear Conductivities and Electrochemical Performances of LiNi_{0.5}Co_{0.2}Mn_{0.3}O₂ Electrodes. *J. Electrochem. Soc.* **2016**, *163* (13), A2720–A2724.
- (43) Koerver, R.; Aygün, I.; Leichtweiß, T.; Dietrich, C.; Zhang, W.; Binder, J. O.; Hartmann, P.; Zeier, W. G.; Janek, J. Capacity Fade in Solid-State Batteries: Interphase Formation and Chemomechanical Processes in Nickel-Rich Layered Oxide Cathodes and Lithium Thiophosphate Solid Electrolytes. *Chem. Mater.* **2017**, *29* (13), 5574–5582.
- (44) Nara, H.; Morita, K.; Mukoyama, D.; Yokoshima, T.; Momma, T.; Osaka, T. Impedance Analysis of LiNi_{1/3}Mn_{1/3}Co_{1/3}O₂ Cathodes with Different Secondary-Particle Size Distribution in Lithium-Ion Battery. *Electrochim. Acta* **2017**, *241*, 323–330.
- (45) Zhang, W.; Weber, D. A.; Weigand, H.; Arlt, T.; Manke, I.; Schröder, D.; Koerver, R.; Leichtweiß, T.; Hartmann, P.; Zeier, W. G.; et al. Interfacial Processes and Influence of Composite Cathode Microstructure Controlling the Performance of All-Solid-State Lithium Batteries. *ACS Appl. Mater. Interfaces* **2017**, *9* (21), 17835–17845.
- (46) Chen, X.; Lu, W.; Chen, C.; Xue, M. Improved Electrochemical Performance of LiNi_{0.5}Co_{0.2}Mn_{0.3}O₂ Cathode with Different Carbon Additives for Lithium-Ion Batteries. *Int. J. Electrochem. Sci.* **2018**, *13* (1), 296–304.
- (47) Strauss, F.; Bartsch, T.; de Biasi, L.; Kim, A.-Y.; Janek, J.; Hartmann, P.; Brezesinski, T. Impact of Cathode Material Particle Size on the Capacity of Bulk-Type All-Solid-State Batteries. *ACS Energy Lett.* **2018**, *3* (4), 992–996.
- (48) Bielefeld, A.; Weber, D. A.; Janek, J. Microstructural Modeling of Composite Cathodes for All-Solid-State Batteries. *J. Phys. Chem. C* **2019**, *123* (3), 1626–1634.
- (49) Landesfeind, J.; Eldiven, A.; Gasteiger, H. A. Influence of the Binder on Lithium Ion Battery Electrode Tortuosity and Performance. *J. Electrochem. Soc.* **2018**, *165* (5), A1122–A1128.
- (50) Guy, D.; Lestriez, B.; Bouchet, R.; Guyomard, D. Critical Role of Polymeric Binders on the Electronic Transport Properties of Composites Electrode. *J. Electrochem. Soc.* **2006**, *153* (4), A679–A688.
- (51) Gaberscek, M.; Dominko, R.; Jamnik, J. Is Small Particle Size More Important than Carbon Coating? An Example Study on LiFePO₄ Cathodes. *Electrochem. Commun.* **2007**, *9* (12), 2778–2783.
- (52) Zhang, Q.; Peng, G.; Wang, G.; Qu, M.; Yu, Z. L. Effect of Mesoporous Carbon Containing Binary Conductive Additives in Lithium Ion Batteries on the Electrochemical Performance of the LiCoO₂ Composite Cathodes. *Solid State Ionics* **2009**, *180* (9–10), 698–702.
- (53) Lestriez, B. Functions of Polymers in Composite Electrodes of Lithium Ion Batteries. *C. R. Chim.* **2010**, *13* (11), 1341–1350.
- (54) Lee, J.-H.; Wee, S.-B.; Kwon, M.-S.; Kim, H.-H.; Choi, J.-M.; Song, M.-S.; Park, H. B.; Kim, H.; Paik, U. Strategic Dispersion of Carbon Black and Its Application to Ink-Jet-Printed Lithium Cobalt Oxide Electrodes for Lithium Ion Batteries. *J. Power Sources* **2011**, *196*, 6449–6455.
- (55) Zhang, Q.; Fan, W.; Wang, G.; Qu, M.; Yu, Z. Role of Mesopores on the Electrochemical Performance of LiCoO₂ Composite Cathodes for Lithium Ion Batteries. *Ionics* **2011**, *17* (8), 697–703.
- (56) Liu, G.; Zheng, H.; Song, X.; Battaglia, V. S. Particles and Polymer Binder Interaction: A Controlling Factor in Lithium-Ion Electrode Performance. *J. Electrochem. Soc.* **2012**, *159* (3), A214–A221.
- (57) Patel, R. L.; Park, J.; Liang, X. Ionic and Electronic Conductivities of Atomic Layer Deposition Thin Film Coated Lithium Ion Battery Cathode Particles. *RSC Adv.* **2016**, *6* (101), 98768–98776.
- (58) Amin, R.; Chiang, Y.-M. Characterization of Electronic and Ionic Transport in Li_{1-x}Ni_{0.33}Mn_{0.33}Co_{0.33}O₂ (NMC₃₃₃) and Li_{1-x}Ni_{0.50}Mn_{0.20}Co_{0.33}O₂ (NCM₅₂₃) as a Function of Li Content. *J. Electrochem. Soc.* **2016**, *163* (8), A1512–A1517.
- (59) Wang, S.; Yan, M.; Li, Y.; Vinado, C.; Yang, J. Separating Electronic and Ionic Conductivity in Mix-Conducting Layered Lithium Transition-Metal Oxides. *J. Power Sources* **2018**, *393*, 75–82.
- (60) Seid, K. A.; Badot, J. C.; Dubrunfaut, O.; Caldes, M. T.; Stephant, N.; Gautier, L.; Guyomard, D.; Lestriez, B. Multiscale Electronic Transport in Li_{1+x}Ni_{1/3-x}Co_{1/3-x}Mn_{1/3-x}O₂: A Broadband Dielectric Study from 40 Hz to 10 GHz. *Phys. Chem. Chem. Phys.* **2013**, *15* (45), 19790–19798.
- (61) Shizuka, K.; Kobayashi, T.; Okahara, K.; Okamoto, K.; Kanzaki, S.; Kanno, R. Characterization of Li_{1+x}Ni_xCo_{1-2x}Mn_xO₂ Positive Active Materials for Lithium Ion Batteries. *J. Power Sources* **2005**, *146*, 589–593.
- (62) Bruggeman, D. A. G. Berechnung Verschiedener Physikalischer Konstanten von Heterogenen Substanzen. *Ann. Phys.* **1935**, *416* (7), 636–664.

- (63) Sen, P. N.; Scala, C.; Cohen, M. H. A Self-similar Model for Sedimentary Rocks with Application to the Dielectric Constant of Fused Glass Beads. *Geophysics* **1981**, *46* (5), 781–795.
- (64) Papatthanasious, A. N. Evaluation of the Activation Volume from Ionic Conductivity Measurements under Pressure in Porous Materials. *Phys. Rev. B: Condens. Matter Mater. Phys.* **1998**, *58* (24), 16038–16041.
- (65) Cuevas, F. G.; Montes, J. M.; Cintas, J.; Urban, P. Electrical Conductivity and Porosity Relationship in Metal Foams. *J. Porous Mater.* **2009**, *16* (6), 675–681.
- (66) Xu, R.; Sun, H.; de Vasconcelos, L. S.; Zhao, K. Mechanical and Structural Degradation of LiNi_{0.8}Mn_{0.15}Co_{0.05}O₂ Cathode in Li-Ion Batteries: An Experimental Study. *J. Electrochem. Soc.* **2017**, *164* (13), A3333–A3341.
- (67) Vasconcelos, L. S. de; Xu, R.; Li, J.; Zhao, K. Grid Indentation Analysis of Mechanical Properties of Composite Electrodes in Li-Ion Batteries. *Extrem. Mech. Lett.* **2016**, *9*, 495–502.
- (68) Uchida, I.; Fujiyoshi, H.; Waki, S. Microvoltammetric Studies on Single Particles of Battery Active Materials. *J. Power Sources* **1997**, *68*, 139–144.
- (69) Nishizawa, M.; Uchida, I. Microelectrode-Based Characterization Systems for Advanced Materials in Battery and Sensor Applications. *Electrochim. Acta* **1999**, *44* (21), 3629–3637.
- (70) Dokko, K.; Horikoshi, S.; Itoh, T.; Nishizawa, M.; Mohamedi, M.; Uchida, I. Microvoltammetry for Cathode Materials at Elevated Temperatures: Electrochemical Stability of Single Particles. *J. Power Sources* **2000**, *90*, 109–115.
- (71) Dokko, K.; Nishizawa, M.; Horikoshi, S.; Itoh, T.; Mohamedi, M.; Uchida, I. In Situ Observation of LiNiO₂ Single-Particle Fracture during Li-Ion Extraction and Insertion. *Electrochem. Solid-State Lett.* **1999**, *3* (3), 125–127.
- (72) Dokko, K.; Mohamedi, M.; Fujita, Y.; Itoh, T.; Nishizawa, M.; Umeda, M.; Uchida, I. Kinetic Characterization of Single Particles of LiCoO₂ by AC Impedance and Potential Step Methods. *J. Electrochem. Soc.* **2001**, *148* (5), A422–A426.
- (73) Dokko, K.; Mohamedi, M.; Umeda, M.; Uchida, I. Kinetic Study of Li-Ion Extraction and Insertion at LiMn₂O₄ Single Particle Electrodes Using Potential Step and Impedance Methods. *J. Electrochem. Soc.* **2003**, *150* (4), A425–A429.
- (74) Ando, K.; Yamada, Y.; Nishikawa, K.; Matsuda, T.; Imamura, D.; Kanamura, K. Degradation Analysis of LiNi_{0.8}Co_{0.15}Al_{0.05}O₂ for Cathode Material of Lithium-Ion Battery Using Single-Particle Measurement. *ACS Appl. Energy Mater.* **2018**, *1* (9), 4536–4544.
- (75) Dokko, K.; Nakata, N.; Kanamura, K. High Rate Discharge Capability of Single Particle Electrode of LiCoO₂. *J. Power Sources* **2009**, *189*, 783–785.
- (76) Munakata, H.; Takemura, B.; Saito, T.; Kanamura, K. Evaluation of Real Performance of LiFePO₄ by Using Single Particle Technique. *J. Power Sources* **2012**, *217*, 444–448.
- (77) Miller, D. J.; Proff, C.; Wen, J. G.; Abraham, D. P.; Bareño, J. Observation of Microstructural Evolution in Li Battery Cathode Oxide Particles by In Situ Electron Microscopy. *Adv. Energy Mater.* **2013**, *3* (8), 1098–1103.
- (78) Tsai, P.-C.; Wen, B.; Wolfman, M.; Choe, M.-J.; Pan, M. S.; Su, L.; Thornton, K.; Cabana, J.; Chiang, Y.-M. Single-Particle Measurements of Electrochemical Kinetics in NMC and NCA Cathodes for Li-Ion Batteries. *Energy Environ. Sci.* **2018**, *11* (4), 860–871.
- (79) Li, T.; Song, B.; Lu, L.; Zeng, K. Voltage Induced Electrochemical Reactions in the Single Lithium-Rich Layer-Oxide Nanoparticles. *Phys. Chem. Chem. Phys.* **2015**, *17* (15), 10257–10264.
- (80) Snowden, M. E.; Dayeh, M.; Payne, N. A.; Gervais, S.; Mauzeroll, J.; Schougaard, S. B. Measurement on Isolated Lithium Iron Phosphate Particles Reveals Heterogeneity in Material Properties Distribution. *J. Power Sources* **2016**, *325*, 682–689.
- (81) Palencsár, A.; Scherson, D. A. Electrochemical and In Situ Optical Characterization of Single Micrometer-Size Particles of Spherical Nickel Oxide in Alkaline Aqueous Electrolytes. *Electrochem. Solid-State Lett.* **2003**, *6* (4), E1–E4.
- (82) Less, G. B.; Seo, J. H.; Han, S.; Sastry, A. M.; Zausch, J.; Latz, A.; Schmidt, S.; Wieser, C.; Kehrwald, D.; Fell, S. Micro-Scale Modeling of Li-Ion Batteries: Parameterization and Validation. *J. Electrochem. Soc.* **2012**, *159* (6), A697–A704.
- (83) Wiedemann, A. H.; Goldin, G. M.; Barnett, S. A.; Zhu, H.; Kee, R. J. Effects of Three-Dimensional Cathode Microstructure on the Performance of Lithium-Ion Battery Cathodes. *Electrochim. Acta* **2013**, *88*, 580–588.
- (84) Ledovskikh, A. V.; Verhallen, T. W.; Wagemaker, M. The Non-Ohmic Nature of Intercalation Materials and the Consequences for Charge Transport Limitations. *Energy Storage Mater.* **2019**, *18*, 476–490.
- (85) Maier, J. Evaluation of Electrochemical Methods in Solid State Research and Their Generalization for Defects with Variable Charges. *Z. Phys. Chem.* **1984**, *140* (2), 191–215.
- (86) Huggins, R. A. Simple Method to Determine Electronic and Ionic Components of the Conductivity in Mixed Conductors: A Review. *Ionics* **2002**, *8* (3), 300–313.
- (87) Xu, J.; Wong, C. P. High Dielectric Constant SU8 Composite Photoresist for Embedded Capacitors. *J. Appl. Polym. Sci.* **2007**, *103* (3), 1523–1528.
- (88) Bryan, A. B. The Dielectric Constants of Argon and Neon. *Phys. Rev.* **1929**, *34* (4), 615–617.
- (89) Kim, J.-H.; Kim, S. J.; Yuk, T.; Kim, J.; Yoon, C. S.; Sun, Y.-K. Variation of Electronic Conductivity within Secondary Particles Revealing a Capacity-Fading Mechanism of Layered Ni-Rich Cathode. *ACS Energy Lett.* **2018**, *3* (12), 3002–3007.
- (90) Thomas, M. G. S. R.; Goodenough, J. B. AC Impedance Analysis of Polycrystalline Insertion Electrodes: Application to Li_{1-x}CoO₂. *J. Electrochem. Soc.* **1985**, *132* (7), 1521–1528.
- (91) Matsumoto, K.; Kuzuo, R.; Takeya, K.; Yamanaka, A. Effects of CO₂ in Air on Li Deintercalation from LiNi_{1-x-y}Co_xAl_yO₂. *J. Power Sources* **1999**, *81*–82, 558–561.
- (92) Edström, K.; Gustafsson, T.; Thomas, J. O. The Cathode-Electrolyte Interface in the Li-Ion Battery. *Electrochim. Acta* **2004**, *50* (2–3), 397–403.
- (93) Mijung, N.; Lee, Y.; Cho, J. Water Adsorption and Storage Characteristics of Optimized LiCoO₂ and LiNi_{1/3}Co_{1/3}Mn_{1/3}O₂ Composite Cathode Material for Li-Ion Cells. *J. Electrochem. Soc.* **2006**, *153* (5), A935–A940.
- (94) Jung, R.; Morasch, R.; Karayalali, P.; Phillips, K.; Maglia, F.; Stinner, C.; Shao-Horn, Y.; Gasteiger, H. A. Effect of Ambient Storage on the Degradation of Ni-Rich Positive Electrode Materials (NMC811) for Li-Ion Batteries. *J. Electrochem. Soc.* **2018**, *165* (2), A132–A141.
- (95) Gauthier, M.; Carney, T. J.; Grimaud, A.; Giordano, L.; Pour, N.; Chang, H.-H.; Fenning, D. P.; Lux, S. F.; Paschos, O.; Bauer, C.; et al. Electrode-Electrolyte Interface in Li-Ion Batteries: Current Understanding and New Insights. *J. Phys. Chem. Lett.* **2015**, *6* (22), 4653–4672.
- (96) Dissanayake, M. A. K. L.; Mellander, B.-E. Phase Diagram and Electrical Conductivity of the Li₂SO₄-Li₂CO₃ System. *Solid State Ionics* **1986**, *21* (4), 279–285.
- (97) Mizusaki, J.; Tagawa, H.; Saito, K.; Uchida, K.; Tezuka, M. Lithium Carbonate as a Solid Electrolyte. *Solid State Ionics* **1992**, *53*–56, 791–797.
- (98) Hornsveld, N.; Put, B.; Kessels, W. M. M.; Vereecken, P. M.; Creatore, M. Plasma-Assisted and Thermal Atomic Layer Deposition of Electrochemically Active Li₂CO₃. *RSC Adv.* **2017**, *7* (66), 41359–41368.
- (99) Xiang, B.; Wang, L.; Liu, G.; Minor, A. M. Electromechanical Probing of Li/Li₂CO₃ Core/Shell Particles in a TEM. *J. Electrochem. Soc.* **2013**, *160* (3), A415–A419.
- (100) Shi, S.; Qi, Y.; Li, H.; Hector, L. G. Defect Thermodynamics and Diffusion Mechanisms in Li₂CO₃ and Implications for the Solid Electrolyte Interphase in Li-Ion Batteries. *J. Phys. Chem. C* **2013**, *117* (17), 8579–8593.

5 Conclusions and Outlook

The experimental approaches developed in the framework of this Ph.D. work and presented in this thesis provide unique experimental access to properties of technologically relevant thin films and particles, respectively, which were not accessible by conventional approaches. Both approaches, to a certain extent, rely on micro- and nanofabrication techniques. The results obtained demonstrate that the additional experimental effort in preparing samples was justified. The approaches proved to be suitable for proper investigations of diffusion processes in WO_3 thin films and charge transport in single NCM 111 secondary particles as a function of particle size.

The results on diffusion in WO_3 thin films were interpreted in terms of concentration-dependent diffusion. They gave direct evidence of different concentration ranges, in which the diffusion coefficient of hydrogen is either constant or depending on the concentration of hydrogen. This finding is of great importance for the interpretation of experimental results gathered from electrochemical experiments and has not been investigated to this extent before. However, some aspects still remain to be studied in the future.

The first aspect is the correlation between the absorbance of the films and the actual hydrogen concentration. The differences in the concentration-dependent diffusion of hydrogen in amorphous and polycrystalline WO_3 imply a strong influence of the thin film morphology on hydrogen diffusion. On the other hand, e.g. the degree of crystallinity of a WO_3 thin film itself has given rise to different models for the EC coloration in the past. In this work, the diffusion process was investigated by monitoring the transmittance of light through WO_3 thin films. A very fundamental study of the influence of morphology and crystallinity on EC coloration and hydrogen diffusion seems very desirable. This would allow the estimation of the extent, to which changes of optical properties are attributed to changes in the ion concentration. A possible consequence could be a correlation between the ion concentration and the transmittance of the WO_3 film that is different from the one assumed by following a Lambert-Beer-like ansatz (see equations (3) and (4) in publication 1). This would lead to deviations between the dependence of the diffusion coefficient on the transmittance, which is the quantity measured in the experiments, and the ion concentration. Thus, the concentration-dependence of the diffusion coefficient may be altered and even become negligible. However, the diffusion coefficient of hydrogen in WO_3 thin films is not expected to be independent of the ion concentration. A change in the activation energy for the coupled diffusion of $\Delta E_a = \pm 60$ meV would change the diffusion coefficient at room temperature by one order of magnitude. Such changes in the activation energy could probably be explained by the changes in the crystal structure or the electronic structure, which occur during EC coloration of WO_3 thin films. Due to the uncertainty of the ion

concentration in the film and the significant morphological differences, no attempts were made to describe the data in terms of a percolation model [229]. It was therefore decided to use a model-independent parametrization of the profiles obtained. After a proper correlation between the ion concentration and the absorbance is established, a future project could be investigating the capability of certain models to describe the observed diffusion processes.

Another aspect for future work should address the origin of the changes in the diffusion coefficient in WO_3 thin films. A percolation model based on two different diffusion pathways with different diffusivity was proposed to describe a decreasing diffusion coefficient upon increasing ion concentration in amorphous WO_3 films [229]. In order to study structural changes upon ion insertion in polycrystalline WO_3 thin films, the specially designed electrochemical cell was also employed in subsequent project works of A. G. Strack. The capability of measuring the transmittance of a laser used for Raman spectroscopy during electrochemical coloration of WO_3 thin films creates a very powerful tool in studying structural, optical and electrochemical properties of WO_3 thin films simultaneously. First results from such in situ Raman spectroscopy and transmittance measurements during electrochemical hydrogen insertion into polycrystalline WO_3 thin films were obtained. They reveal strong influences of the applied potential on the crystal structure observed and the transmittance measured. Also changes of the optical properties without changes of the structural properties were observed, which has not been discussed for polycrystalline films in the literature. This indicates that the EC coloration of polycrystalline WO_3 may require even more research efforts to be fully understood than originally anticipated.

As already discussed, the differences between the diffusion coefficients derived from electrochemical measurements and from the approach presented here differ considerably. It is of interest to understand the differences between both diffusion coefficients in more detail. This is partly addressed in project works of J. L. Dornseifer and P. Tuchecker, who investigate diffusion processes in WO_3 thin films by different methods. This is required in order to evaluate the extent of the aforementioned influence of changes in the absorption process upon ion insertion on the interpretation.

The experiments on single NCM 111 secondary particles yielded experimental access to the investigation of charge transport in single particles, with diameters of several micrometers. The approach presented is based on the immobilization of single particles in traps patterned into a polymer film on a conducting substrate. The use of a specially designed cell enabled the contacting of these immobilized particles with metal films at opposite sides. This approach offers the possibility to use different measurement signals for the characterization of charge transport through different types of particles. It can be applied to a large variety of particulate matter, as long as the particles are dispersible in a solvent, which will not harm the SU-8 layer or its adhesion to the substrate. The large variability offered by photolithographic patterning of SU-8 enables the customization of particle arrangements and systematic investigations on e.g. two or more particles connected in parallel. Arrangements with a different number of particles in a single trap were conducted, but have not

shown any pronounced differences to measurement on single particles. This is probably due to the fact that only one of the particles, the largest one, was contacted by both contacts in case of several particles in the trap.

The mounting of the cell is probably the most decisive part of this approach since it is capable of plastically deforming the particles severely, in case of a large difference between the polymer film height and the particle diameter. The deformation of the porous particles mainly affects the size-dependence of the resistance, from which the partial conductivities have been derived. For this reason, a symmetric truncation of the particles was assumed to describe the plastic deformation. This assumption imposes severe boundaries in the application of the method depending on the mechanic properties of each single particle. As already mentioned, a modified version of the cell was also developed, where the load of the top contact on the particle can be increased in a controlled manner. The systematic evaluation of these load-dependent experiments conducted by J. K. Eckhardt and M. S. Friedrich is another task to be done in the future, since such experiments might lead to conclusions about the influence of particle deformation on the results presented.

The interpretation of the conductivities derived is another aspect to discuss. The impedance spectra of a single porous secondary particle represent the impedance of a porous network of primary particles, i.e. grains and grain boundaries. The derived properties are therefore effective properties of such a network rather than properties of the bulk or the surface of the material. This could be further investigated by charge transport studies on single primary particles and across grain boundaries between single primary particles. An approach based on embedding single secondary particles in an SU-8 matrix was developed. By using an argon-ion beam etching system to partially ablate the SU-8 film, the surface of the secondary particle, and thus single primary particles and primary particle agglomerates, can be exposed again. Corresponding trial experiments were successfully conducted by J. K. Eckhardt. In a subsequent step, two gold contacts on a single primary particle or on two adjacent primary particles could be prepared. An electron beam lithographically patterning process with a subsequent thermal evaporation of gold and a liftoff process appears to be suitable for this purpose. Such an approach was presented by J. Zahn (Institute of Physical Chemistry, Justus Liebig University Giessen) for CeO_2 crystallites [230].

A software to simulate the impedance of a porous secondary particle, which is made up by primary particles and grain boundaries in between them was developed by J. K. Eckhardt [231]. A network model for the impedance of a single secondary particle would possibly be capable of describing the experimentally measured impedance of a single particle based on its microstructure. The microstructure of two representative porous secondary particles was successfully derived from FIB-SEM tomography data recorded by M. Osenberg. By this, contributions of charge transport in and along grains, as well as across grain boundaries to the overall effective impedance could be investigated.

Future work should also take advantage of the special design of the cell developed in this work, since it allows the realization of a half-cell setup with a single secondary particle as the

positive electrode active material. Results on single particles, which would be characterized in both configurations, would allow a more detailed investigation of the electrochemical properties of single particles. Ongoing investigations that aim on the identification of single charge transport processes in such half cells are currently conducted by M. S. Friedrich. In this setup, charge transfer, degradation or cyclability can be investigated on a single-particle level, which can deliver valuable insights into the performance of the material in a composite.

The experimental approaches developed and presented are very versatile and powerful tools for the fundamental investigation of charge transport in thin films and particles, respectively. However, their potential relevance and significance will show in the future as more interesting phenomena in materials for energy technologies and beyond are revealed.

References

- [1] Global Energy & CO₂ Status Report, International Energy Agency: Paris, 2018. URL: <https://www.iea.org/geco/>.
- [2] Cook, J.; Nuccitelli, D.; Green, S. A.; Richardson, M.; Winkler, B.; Painting, R.; Way, R.; Jacobs, P.; Skuce, A. Quantifying the consensus on anthropogenic global warming in the scientific literature. *Environ. Res. Lett.* **2013**, *8* (2), 024024.
- [3] Cook, J.; Oreskes, N.; Doran, P. T.; Anderegg, W. R.; Verheggen, B.; Maibach, E. W.; Carlton, J. S.; Lewandowsky, S.; Skuce, A. G.; Green, S. A.; Nuccitelli, D.; Jacobs, P.; Richardson, M.; Winkler, B.; Painting, R.; Rice, K. Consensus on consensus: a synthesis of consensus estimates on human-caused global warming. *Environ. Res. Lett.* **2016**, *11* (4), 048002.
- [4] Althor, G.; Watson, J. E.; Fuller, R. A. Global mismatch between greenhouse gas emissions and the burden of climate change. *Sci. Rep.* **2016**, *6*, 20281.
- [5] CAS REGISTRY Division of the American Chemical Society. CAS REGISTRY 100 Millionth Fun Facts, URL: <https://www.cas.org/support/documentation/chemical-substances/cas-registry-100-millionth-fun-facts> (accessed November 4, 2019).
- [6] Graedel, T. E.; Barr, R.; Chandler, C.; Chase, T.; Choi, J.; Christoffersen, L.; Friedlander, E.; Henly, C.; Jun, C.; Nassar, N. T.; Schechner, D.; Warren, S.; Yang, M. Y.; Zhu, C. Methodology of Metal Criticality Determination. *Environ. Sci. Technol.* **2012**, *46* (2), 1063–1070.
- [7] Peck, D.; Kandachar, P.; Tempelman, E. Critical materials from a product design perspective. *Mater. Des.* **2015**, *65*, 147–159.
- [8] Study on the review of the list of Critical Raw Materials, Publications Office of the European Union: Luxembourg, 2017.
- [9] Tkaczyk, A. H.; Bartl, A.; Amato, A.; Lapkovskis, V.; Petranikova, M. Sustainability evaluation of essential critical raw materials: cobalt, niobium, tungsten and rare earth elements. *J. Phys. D: Appl. Phys.* **2018**, *51* (20).
- [10] Haynes, W. M.; Lide, D. R.; Bruno, T. J., eds. *CRC Handbook of Chemistry and Physics*, 97th ed.; CRC Press: Boca Raton, FL, 2017.
- [11] Regulation (EU) 2017/821 of the European Parliament and of the Council of 17 May 2017 laying down supply chain due diligence obligations for Union importers of tin, tantalum, and tungsten, their ores, and gold originating from conflict-affected and high-risk areas. *Off. J. Eur. Communities: Legis.* **2017**, *60* (L130).
- [12] Dodd-Frank Wall Street Reform and Consumer Protection Act (Pub.L. 111–203, H.R. 4173), United States Government Printing Office: Washington, DC, 2010.

- [13] Granqvist, C. G.; Arvizu, M. A.; Bayrak Pehlivan, İ.; Qu, H.-Y.; Wen, R.-T.; Niklasson, G. A. Electrochromic materials and devices for energy efficiency and human comfort in buildings: A critical review. *Electrochim. Acta* **2018**, *259*, 1170–1182.
- [14] Zhang, H.; Zhao, H.; Khan, M. A.; Zou, W.; Xu, J.; Zhang, L.; Zhang, J. Recent progress in advanced electrode materials, separators and electrolytes for lithium batteries. *J. Mater. Chem. A* **2018**, *6* (42), 20564–20620.
- [15] Syrrakou, E.; Papaefthimiou, S.; Yianoulis, P. Eco-efficiency evaluation of a smart window prototype. *Sci. Total Environ.* **2006**, *359* (1), 267–282.
- [16] Allouhi, A.; El Fouih, Y.; Kousksou, T.; Jamil, A.; Zeraouli, Y.; Mourad, Y. Energy consumption and efficiency in buildings: current status and future trends. *J. Cleaner Prod.* **2015**, *109*, 118–130.
- [17] Tällberg, R.; Jelle, B. P.; Loonen, R.; Gao, T.; Hamdy, M. Comparison of the energy saving potential of adaptive and controllable smart windows: A state-of-the-art review and simulation studies of thermochromic, photochromic and electrochromic technologies. *Sol. Energy Mater. Sol. Cells* **2019**, *200*, 109828.
- [18] NobelPrize.org Nobel Media AB. The Nobel Prize in Chemistry 2019, URL: <https://www.nobelprize.org/prizes/chemistry/2019/summary/> (accessed November 4, 2019).
- [19] Hoekstra, A. The Underestimated Potential of Battery Electric Vehicles to Reduce Emissions. *Joule* **2019**, *3* (6), 1412–1414.
- [20] Xu, J. W.; Chua, M. H.; Shah, K. W., eds. *Electrochromic Smart Materials – Fabrication and Applications*, 1st ed.; Royal Society of Chemistry: London, 2019.
- [21] Global EV Outlook 2019, International Energy Agency: Paris. URL: <https://webstore.iaea.org/global-ev-outlook-2019>.
- [22] Granqvist, C. G. *Handbook of Inorganic Electrochromic Materials*, Elsevier Science B.V.: Amsterdam, 1995.
- [23] Monk, P. M. S.; Mortimer, R. J.; Rosseinsky, D. R. *Electrochromism: Fundamentals and Applications*, VCH: Weinheim, New York, Basel, Cambridge, Tokyo, 1995.
- [24] Mortimer, R. J.; Rosseinsky, D. R.; Monk, P. M. S., eds. *Electrochromic Materials and Devices*, Wiley-VCH Verlag GmbH & Co. KGaA: Weinheim, 2015.
- [25] Platt, J. R. Electrochromism, a Possible Change of Color Producible in Dyes by an Electric Field. *J. Chem. Phys.* **1961**, *34* (3), 862–863.
- [26] Chang, I. F.; Gilbert, B. L.; Sun, T. I. Electrochromic Systems for Display Applications. *J. Electrochem. Soc.* **1975**, *122* (7), 955–962.
- [27] Goddard, N. J.; Jackson, A. C.; Thomas, M. G. Spectroelectrochemical studies of some viologens used in electrochromic display applications. *J. Electroanal. Chem. Interfacial Electrochem.* **1983**, *159* (2), 325–335.
- [28] Granqvist, C. G. Electrochromic tungsten oxide films: Review of progress 1993-1998. *Sol. Energy Mater. Sol. Cells* **2000**, *60* (3), 201–262.

- [29] K., B. Colouration of tungsten oxide films: A model for optically active coatings. *Sol. Energy Mater. Sol. Cells* **1999**, *58* (1), 1–131.
- [30] Padilla, J.; Seshadri, V.; Sotzing, G. A.; Otero, T. F. Maximum contrast from an electrochromic material. *Electrochem. Commun.* **2007**, *9* (8), 1931–1935.
- [31] Invernale, M. A.; Acik, M.; Sotzing, G. A. Thiophene-based electrochromic materials. In *Handbook of Thiophene-Based Materials: Applications in Organic Electronics and Photonics*; Perepichka, I. F., Perepichka, D. F., Eds.; John Wiley & Sons Ltd: Chichester, 2009; pp 757–782.
- [32] Hassab, S.; Shen, D. E.; Österholm, A. M.; Da Rocha, M.; Song, G.; Alesanco, Y.; Viñuales, A.; Rougier, A.; Reynolds, J. R.; Padilla, J. A new standard method to calculate electrochromic switching time. *Sol. Energy Mater. Sol. Cells* **2018**, *185*, 54–60.
- [33] Verhoeven, J. W. Glossary of terms used in photochemistry (IUPAC Recommendations 1996). *Pure Appl. Chem.* **1996**, *68* (12), 2223–2286.
- [34] Lee, S.-H.; Cheong, H. M.; Tracy, C. E.; Mascarenhas, A.; Czanderna, A. W.; Deb, S. K. Electrochromic coloration efficiency of α - WO_{3-y} thin films as a function of oxygen deficiency. *Appl. Phys. Lett.* **1999**, *75* (11), 1541–1543.
- [35] Somani, P. R.; Radhakrishnan, S. Electrochromic materials and devices: present and future. *Mater. Chem. Phys.* **2002**, *77* (1), 117–133.
- [36] Azimirad, R.; Akhavan, O.; Moshfegh, A. Z. Influence of Coloring Voltage and Thickness on Electrochromical Properties of e-beam Evaporated WO_3 Thin Films. *J. Electrochem. Soc.* **2006**, *153* (2), E11–E16.
- [37] Sallard, S.; Brezesinski, T.; Smarsly, B. M. Electrochromic Stability of WO_3 Thin Films with Nanometer-Scale Periodicity and Varying Degrees of Crystallinity. *J. Phys. Chem. C* **2007**, *111* (19), 7200–7206.
- [38] Gillaspie, D. T.; Tenent, R. C.; Dillon, A. C. Metal-oxide films for electrochromic applications: present technology and future directions. *J. Mater. Chem.* **2010**, *20* (43), 9585.
- [39] Sahu, D. R.; Hung, C.-Y.; Wang, S.-C.; Huang, J.-L. Existence of electrochromic reversibility at the 1000th cyclic voltammetry for spin coating WO_3 film. *Ionics* **2017**, *23* (11), 3227–3233.
- [40] Jensen, J.; Hösel, M.; Dyer, A. L.; Krebs, F. C. Development and Manufacture of Polymer-Based Electrochromic Devices. *Adv. Funct. Mater.* **2015**, *25* (14), 2073–2090.
- [41] Czanderna, A. W.; Benson, D. K.; Jorgensen, G. J.; Zhang, J.-G.; Tracy, C. E.; Deb, S. K. Durability issues and service lifetime prediction of electrochromic windows for buildings applications. *Sol. Energy Mater. Sol. Cells* **1999**, *56* (3), 419–436.
- [42] Lampert, C. M.; Agrawal, A.; Baertlien, C.; Nagai, J. Durability evaluation of electrochromic devices – an industry perspective. *Sol. Energy Mater. Sol. Cells* **1999**, *56* (3), 449–463.

- [43] Nagai, J.; McMeeking, G. D.; Saitoh, Y. Durability of electrochromic glazing. *Sol. Energy Mater. Sol. Cells* **1999**, *56* (3), 309–319.
- [44] Sbar, N.; Badding, M.; Budziak, R.; Cortez, K.; Laby, L.; Michalski, L.; Ngo, T.; Schulz, S.; Urbanik, K. Progress toward durable, cost effective electrochromic window glazings. *Sol. Energy Mater. Sol. Cells* **1999**, *56* (3), 321–341.
- [45] Kubo, T.; Tanimoto, J.; Minami, M.; Toya, T.; Nishikitani, Y.; Watanabe, H. Performance and durability of electrochromic windows with carbon-based counter electrode and their application in the architectural and automotive fields. *Solid State Ionics* **2003**, *165* (1), 97–104.
- [46] Syrrakou, E.; Papaefthimiou, S.; Yianoulis, P. Environmental assessment of electrochromic glazing production. *Sol. Energy Mater. Sol. Cells* **2005**, *85* (2), 205–240.
- [47] Papaefthimiou, S.; Syrrakou, E.; Yianoulis, P. Energy performance assessment of an electrochromic window. *Thin Solid Films* **2006**, *502* (1), 257–264.
- [48] Cruz, H.; Jordão, N.; Branco, L. C. Deep eutectic solvents (DESs) as low-cost and green electrolytes for electrochromic devices. *Green Chem.* **2017**, *19* (7), 1653–1658.
- [49] Granqvist, C. G. Out of a niche. *Nat. Mater.* **2006**, *5* (2), 89–90.
- [50] Reisfeld, R.; Zayat, M.; Minti, H.; Zastrow, A. Electrochromic glasses prepared by the sol-gel method. *Sol. Energy Mater. Sol. Cells* **1998**, *54* (1), 109–120.
- [51] Ehrmann, W.; Gressmann, M.; Nutsch, W.; Pahl, H.-J. *Fenster-, Türen- und Fassadentechnik für Metallbauer und Holztechniker*, 3rd ed.; Verlag Eurpoa-Lehrmittel, Nourney, Wollmer GmbH & Co. KG: Haan-Gruiten, 2008.
- [52] Gordon, J.; Mathew, H.; Sapers, S. P.; Cumbo, M. J.; O'Brien, N. A.; Sargent, R. B.; Raksha, V. P.; Lahaderne, R. B.; Hichwa, B. P. Large area electrochromics for architectural applications. *J. Non-Cryst. Solids* **1997**, *218*, 342–346.
- [53] O'Brien, N. A.; Gordon, J.; Mathew, H.; Hichwa, B. P. Electrochromic coatings—applications and manufacturing issues. *Thin Solid Films* **1999**, *345* (2), 312–318.
- [54] Kraft, A.; Rottmann, M. Properties, performance and current status of the laminated electrochromic glass of Gesimat. *Sol. Energy Mater. Sol. Cells* **2009**, *93* (12), 2088–2092.
- [55] Xu, C.; Ma, C.; Kong, X.; Taya, M. Vacuum filling process for electrolyte in enhancing electrochromic polymer window assembly. *Polym. Adv. Technol.* **2009**, *20* (3), 178–182.
- [56] Berzelius, J. J. Untersuchung der Zusammensetzung der bis jetzt bekannten Wolframate. *Journal für Chemie und Physik* **1816**, *16* (4), 476–488.
- [57] Kobosew, N.; Nekrassow, N. I. Bildung freier Wasserstoffatome bei Kathodenpolarisation der Metalle. *Z. Elektrochem. Angew. Phys. Chem.* **1930**, *36* (8), 529–544.
- [58] Deb, S. K. A Novel Electrophotographic System. *Appl. Opt.* **1969**, *8* (S1), 192–195.

- [59] Meisel, K. Rheniumtrioxyd. III. Mitteilung. Über die Kristallstruktur des Rheniumtrioxyd. *Z. Anorg. Allg. Chem.* **1932**, 207 (1), 121–128.
- [60] Goodenough, J. B. Metallic oxides. *Prog. Solid State Chem.* **1971**, 5, 145–399.
- [61] Hirose, T. Structural Phase Transition and Semiconductor-Metal Transition in WO_3 . *J. Phys. Soc. Jpn.* **1980**, 49 (2), 562–568.
- [62] Hjelm, A.; Granqvist, C. G.; Wills, J. Electronic structure and optical properties of WO_3 , LiWO_3 , NaWO_3 , and HWO_3 . *Phys. Rev. B* **1996**, 54 (4), 2436–2445.
- [63] Corà, F.; Stachiotti, M. G.; Catlow, C. R. A.; Rodriguez, C. O. Transition Metal Oxide Chemistry: Electronic Structure Study of WO_3 , ReO_3 , and NaWO_3 . *J. Phys. Chem. B* **1997**, 101 (20), 3945–3952.
- [64] Bullett, D. W. Bulk and surface electron states in WO_3 and tungsten bronzes. *J. Phys. C: Solid State Phys.* **1983**, 16 (11), 2197–2207.
- [65] Koffyberg, F. P.; Dwight, K.; Wold, A. Interband transitions of semiconducting oxides determined from photoelectrolysis spectra. *Solid State Commun.* **1979**, 30 (7), 433–437.
- [66] Companion, A. L.; Mackin, M. Diffuse Reflectance Spectra of Some Thiometallates and Oxides of the Chromium Family. *J. Chem. Phys.* **1965**, 42 (12), 4219–4222.
- [67] Butler, M. A.; Nasby, R. D.; Quinn, R. K. Tungsten trioxide as an electrode for photoelectrolysis of water. *Solid State Commun.* **1976**, 19 (10), 1011–1014.
- [68] Butler, M. A. Photoelectrolysis and physical properties of the semiconducting electrode WO_2 . *J. Appl. Phys.* **1977**, 48 (5), 1914–1920.
- [69] Chatten, R.; Chadwick, A. V.; Rougier, A.; Lindan, P. J. D. The Oxygen Vacancy in Crystal Phases of WO_3 . *J. Phys. Chem. B* **2005**, 109 (8), 3146–3156.
- [70] Walkingshaw, A. D.; Spaldin, N. A.; Artacho, E. Density-functional study of charge doping in WO_3 . *Phys. Rev. B* **2004**, 70 (16), 165110.
- [71] Wang, Z.; He, Y.; Gu, M.; Du, Y.; Mao, S. X.; Wang, C. Electron Transfer Governed Crystal Transformation of Tungsten Trioxide upon Li Ions Intercalation. *ACS Appl. Mater. Interfaces* **2016**, 8 (37), 24567–24572.
- [72] Wang, W.; Janotti, A.; Van De Walle, C. G. Phase transformations upon doping in WO_3 . *J. Chem. Phys.* **2017**, 146 (21), 214504.
- [73] Wolfram, T.; Ellialtıođlu, Ş. *Electronic and optical Properties of d-Band Perovskites*, Cambridge University Press: Cambridge, New York, Melbourne, Madrid, Cape Town, Singapore, São Paulo, 2006.
- [74] Julien, C. M. Lithium intercalated compounds: Charge transfer and related properties. *Mater. Sci. Eng., R* **2003**, 40 (2), 47–102.
- [75] Georg, A.; Graf, W.; Wittwer, V. Comparison of electrical conductivity and optical properties of substoichiometrically and electrochemically coloured WO_x films of different crystallinity. *Sol. Energy Mater. Sol. Cells* **1998**, 51 (3), 353–370.

- [76] Gerosa, M.; Di Valentin, C.; Onida, G.; Bottani, C. E.; Pacchioni, G. Anisotropic Effects of Oxygen Vacancies on Electrochromic Properties and Conductivity of γ -Monoclinic WO_3 . *J. Phys. Chem. C* **2016**, *120* (21), 11716–11726.
- [77] Jarman, R. H.; Dickens, P. G. Electrochemical Insertion of Hydrogen in WO_3 . *J. Electrochem. Soc.* **1982**, *129* (10), 2276–2278.
- [78] Dupin, J. C.; Gonbeau, D.; Martin-Litas, I.; Vinatier, P.; Levasseur, A. Lithium intercalation/deintercalation in transition metal oxides investigated by X-ray photoelectron spectroscopy. *J. Electron Spectrosc. Relat. Phenom.* **2001**, *120* (1), 55–65.
- [79] Georg, A.; Georg, A.; Krašovec, U. O.; Wittwer, V. Phase Transitions of the WO_3 Layer in Photoelectrochromic Devices. *J. New Mater. Electrochem. Syst.* **2005**, *8* (4), 317–325.
- [80] Berak, J. M.; Sienko, M. J. Effect of Oxygen-Deficiency on Electrical Transport Properties of Tungsten Trioxide Crystals. *J. Solid State Chem.* **1970**, *2* (1), 109–133.
- [81] Wriedt, H. A. The O-W (Oxygen-Tungsten) System. *Bull. Alloy Phase Diagrams* **1989**, *10* (4), 368–384.
- [82] Woodward, P. M.; Sleight, A. W.; Vogt, T. Ferroelectric Tungsten Trioxide. *J. Solid State Chem.* **1997**, *131* (1), 9–17.
- [83] Salje, E. K. H.; Rehmann, S.; Pobell, F.; Morris, D.; Knight, K. S.; Herrmannsdörfer, T.; Dove, M. T. Crystal structure and paramagnetic behaviour of $\varepsilon\text{-WO}_{3-x}$. *J. Phys.: Condens. Matter* **1997**, *9* (31), 6563–6577.
- [84] Sawada, S. Microscopic and X-Ray Studies on Tungsten Oxide (WO_3). *J. Phys. Soc. Jpn.* **1956**, *11* (12), 1246–1252.
- [85] Salje, E. K. H.; Viswanathan, K. Physical Properties and Phase Transitions in WO_3 . *Acta Crystallogr.* **1975**, *A31* (3), 356–359.
- [86] Diehl, R.; Brandt, G.; Salje, E. K. H. The Crystal Structure of Triclinic WO_3 . *Acta Crystallogr.* **1978**, *B34* (4), 1105–1111.
- [87] Woodward, P. M.; Sleight, A. W.; Vogt, T. Structure refinement of triclinic tungsten trioxide. *J. Phys. Chem. Solids* **1995**, *56* (10), 1305–1315.
- [88] Tanisaki, S. Crystal Structure of Monoclinic Tungsten Trioxide at Room Temperature. *J. Phys. Soc. Jpn.* **1960**, *15* (4), 573–581.
- [89] Tanisaki, S. On the Phase Transition of Tungsten Trioxide below Room Temperature. *J. Phys. Soc. Jpn.* **1960**, *15* (4), 566–573.
- [90] Loopstra, B. O.; Boldrini, P. Neutron Diffraction Investigation of WO_3 . *Acta Crystallogr.* **1966**, *21* (1), 158–162.
- [91] Loopstra, B. O.; Rietveld, H. M. Further refinement of the structure of WO_3 . *Acta Crystallogr.* **1969**, *B25* (7), 1420–1421.

- [92] Perri, J. A.; Banks, E.; Post, B. Study of Phase Transitions in WO_3 with a High-Temperature X-Ray Diffractometer. *J. Appl. Phys.* **1957**, *28* (11), 1272–1275.
- [93] Andersson, G. On the Crystal Structure of Tungsten Trioxide. *Acta Chem. Scand.* **1953**, *7* (1), 154–158.
- [94] Ueda, R.; Ichinokawa, T. On the Phase Transition of Tungsten Trioxide. *Phys. Rev.* **1951**, *82* (4), 563–564.
- [95] Vogt, T.; Woodward, P. M.; Hunter, B. A. The High-Temperature Phases of WO_3 . *J. Solid State Chem.* **1999**, *144* (1), 209–215.
- [96] Salje, E. K. H. The Orthorhombic Phase of WO_3 . *Acta Crystallogr.* **1977**, *B33* (2), 574–577.
- [97] Locherer, K. R.; Swainson, I. P.; Salje, E. K. H. Transition to a new tetragonal phase of WO_3 : crystal structure and distortion parameters. *J. Phys.: Condens. Matter* **1999**, *11* (21), 4143–4156.
- [98] Locherer, K. R.; Salje, E. K. H. The refinement of a tetragonal phase of WO_3 using a novel PSD high temperature X-ray powder diffractometer. *Phase Transitions* **1999**, *69* (1), 85–93.
- [99] Kehl, W. L.; Hay, R. G.; Wahl, D. The Structure of Tetragonal Tungsten Trioxide. *J. Appl. Phys.* **1952**, *23* (2), 212–215.
- [100] Siedle, A. R.; Wood, T. E.; Brostrom, M. L.; Koskenmaki, D. C.; Montez, B.; Oldfield, E. Solid-State Polymerization of Molecular Metal Oxide Clusters: Aluminum 12-Tungstophosphate. *J. Am. Chem. Soc.* **1989**, *111* (5), 1665–1669.
- [101] LeGore, L. J.; Lad, R. J.; Moulzolf, S. C.; Vetelino, J. F.; Frederick, B. G.; Kenik, E. A. Defects and morphology of tungsten trioxide thin films. *Thin Solid Films* **2002**, *406* (1), 79–86.
- [102] Crichton, W. A.; Bouvier, P.; Grzechnik, A. The first bulk synthesis of ReO_3 -type tungsten trioxide, WO_3 , from nanometric precursors. *Mater. Res. Bull.* **2003**, *38* (2), 289–296.
- [103] Glazer, A. M. The Classification of Tilted Octahedra in Perovskites. *Acta Crystallogr.* **1972**, *B28* (11), 3384–3392.
- [104] Roussel, P.; Labbé, P.; Groult, D. Symmetry and twins in the monophosphate tungsten bronze series $(\text{PO}_2)_4(\text{WO}_3)_{2m}$ ($2 \leq m \leq 14$). *Acta Crystallogr.* **2000**, *B56* (3), 377–391.
- [105] Glemser, O.; Naumann, C. Kristallisierte Wolframblauerbindungen: Wasserstoffanaloga der Wolframbronzen H_xWO_3 . *Z. Anorg. Allg. Chem.* **1951**, *265* (4-6), 288–302.
- [106] Wiseman, P. J.; Dickens, P. G. The Crystal Structure of Cubic Hydrogen Tungsten Bronze. *J. Solid State Chem.* **1973**, *6* (3), 374–377.
- [107] Dickens, P. G.; Hurditch, R. J. X-ray and Neutron Diffraction Studies of a Tetragonal Hydrogen Bronze H_xWO_3 . *Nature* **1967**, *215* (5107), 1266–1267.

- [108] Zhong, Q.; Dahn, J. R.; Colbow, K. Lithium intercalation into WO_3 and the phase diagram of Li_xWO_3 . *Phys. Rev. B* **1992**, *46* (4), 2554–2560.
- [109] Genin, C.; Driouiche, A.; Gérard, B.; Figlarz, M. Hydrogen bronzes of new oxides of the WO_3 - MoO_3 system with hexagonal, pyrochlore and ReO_3 -type structures. *Solid State Ionics* **1992**, *53-56*, 315–323.
- [110] Runnerstrom, E. L.; Llordés, A.; Lounis, S. D.; Milliron, D. J. Nanostructured electrochromic smart windows: traditional materials and NIR-selective plasmonic nanocrystals. *Chem. Commun.* **2014**, *50* (73), 10555–10572.
- [111] Niklasson, G. A.; Granqvist, C. G. Electrochromics for smart windows: thin films of tungsten oxide and nickel oxide, and devices based on these. *J. Mater. Chem.* **2007**, *17* (2), 127–156.
- [112] Kamal, H.; Akl, A. A.; Abdel-Hady, K. Influence of proton insertion on the conductivity, structural and optical properties of amorphous and crystalline electrochromic WO_3 films. *Phys. B* **2004**, *349* (1), 192–205.
- [113] Darmawi, S.; Burkhardt, S.; Leichtweiss, T.; Weber, D. A.; Wenzel, S.; Janek, J.; Elm, M. T.; Klar, P. J. Correlation of electrochromic properties and oxidation states in nanocrystalline tungsten trioxide. *Phys. Chem. Chem. Phys.* **2015**, *17* (24), 15903–15911.
- [114] Zeller, H. R.; Beyeler, H. U. Electrochromism and Local Order in Amorphous WO_3 . *Appl. Phys.* **1977**, *13* (3), 231–237.
- [115] Wittwer, V.; Schirmer, O. F.; Schlotter, P. Disorder dependence and optical detection of the Anderson transition in amorphous H_xWO_3 bronzes. *Solid State Commun.* **1978**, *25* (12), 977–980.
- [116] Gérard, P.; Deneuve, A.; Courths, R. Characterization of a-“ WO_3 ” thin films before and after colouration. *Thin Solid Films* **1980**, *71* (2), 221–236.
- [117] Yoshimura, T. Oscillator strength of small-polaron absorption in WO_x ($x \leq 3$) electrochromic thin films. *J. Appl. Phys.* **1985**, *57* (3), 911–919.
- [118] Rebane, K. K. *Impurity Spectra of Solids*, Shier, J. S., Ed.; Plenum Press: New York, London, 1970.
- [119] Fowler, W. B. The Imperfect Solid - Color Centers in Ionic Crystals. In *Defects in Solids*; Hannay, N. B., Ed.; Springer US: Boston, MA, 1975; pp 133–181.
- [120] Deb, S. K. Optical and Photoelectric Properties and Colour Centres in Thin Films of Tungsten Oxide. *Philos. Mag.* **1973**, *27* (4), 801–822.
- [121] Hush, N. S. Intervalence-Transfer Absorption. Part 2. Theoretical Considerations and Spectroscopic Data. In *Progress in Inorganic Chemistry*; Cotton, F. A., Ed.; vol. 8; John Wiley & Sons, Inc.: New York, London, Sydney, 1967; pp 391–443.
- [122] Faughnan, B. W.; Crandall, R. S.; Heyman, P. M. Electrochromism in WO_3 Amorphous Films. *RCA Rev.* **1975**, *36* (1), 177–197.

- [123] Gabrusenoks, J. V.; Cikmach, P. D.; Lusiš, A. R.; Kleperis, J. J.; Ramans, G. M. Electrochromic colour centres in amorphous tungsten trioxide thin films. *Solid State Ionics* **1984**, *14* (1), 25–30.
- [124] Denesuk, M.; Uhlmann, D. R. Site-Saturation Model for the Optical Efficiency of Tungsten Oxide-Based Devices. *J. Electrochem. Soc.* **1996**, *143* (9), L186–L188.
- [125] Bechinger, C.; Burdis, M. S.; Zhang, J. G. Comparison between electrochromic and photochromic coloration efficiency of tungsten oxide thin films. *Solid State Commun.* **1997**, *101* (10), 753–756.
- [126] Zhang, J.-G.; Benson, D. K.; Tracy, C. E.; Deb, S. K.; Czanderna, A. W.; Bechinger, C. Chromic Mechanism in Amorphous WO_3 Films. *J. Electrochem. Soc.* **1997**, *144* (6), 2022–2026.
- [127] Lee, S.-H.; Cheong, H. M.; Zhang, J.-G.; Mascarenhas, A.; Benson, D. K.; Deb, S. K. Electrochromic mechanism in a-WO_{3-y} thin films. *Appl. Phys. Lett.* **1999**, *74* (2), 242–244.
- [128] Berggren, L.; Azens, A.; Niklasson, G. A. Polaron absorption in amorphous tungsten oxide films. *J. Appl. Phys.* **2001**, *90* (4), 1860–1863.
- [129] Stolze, M.; Gogova, D.; Thomas, L.-K. Analogy for the maximum obtainable colouration between electrochromic, gasochromic, and electrocolouration in DC-sputtered thin WO_{3-y} films. *Thin Solid Films* **2005**, *476* (1), 185–189.
- [130] Berggren, L.; Niklasson, G. A. Optical charge transfer absorption in lithium-intercalated tungsten oxide thin films. *Appl. Phys. Lett.* **2006**, *88* (8), 081906.
- [131] Berggren, L.; Jonsson, J. C.; Niklasson, G. A. Optical absorption in lithiated tungsten oxide thin films: Experiment and theory. *J. Appl. Phys.* **2007**, *102* (8), 083538.
- [132] Schirmer, O. F.; Wittwer, V.; Baur, G.; Brandt, G. Dependence of WO_3 Electrochromic Absorption on Crystallinity. *J. Electrochem. Soc.* **1977**, *124* (5), 749–753.
- [133] Lee, S.-H.; Seong, M. J.; Cheong, H. M.; Ozkan, E.; Tracy, E. C.; Deb, S. K. Effect of crystallinity on electrochromic mechanism of Li_xWO_3 thin films. *Solid State Ionics* **2003**, *156* (3), 447–452.
- [134] Holstein, T. Studies of of Polaron Motion Part I: The Molecular-Crystal Model. *Ann. Phys.* **1959**, *8* (3), 325–342.
- [135] Holstein, T. Studies of of Polaron Motion Part II: The “Small” Polaron. *Ann. Phys.* **1959**, *8* (3), 343–389.
- [136] Appel, J. Polarons. *Solid State Phys.* **1968**, *21*, 193–391.
- [137] Austin, I. G.; Mott, N. F. Polarons in Crystalline and Non-crystalline Materials. *Adv. Phys.* **1969**, *18* (71), 41–102.
- [138] Hollinger, G.; Minh Duc, T.; Deneuille, A. Charge Transfer in Amorphous Colored WO_3 Films Observed by X-Ray Photoelectron Spectroscopy. *Phys. Rev. Lett.* **1976**, *37* (23), 1564–1567.

- [139] Reik, H. G.; Heese, D. Frequency dependence of the electrical conductivity of small polarons for high and low temperatures. *J. Phys. Chem. Solids* **1967**, *28* (4), 581–596.
- [140] Salje, E. K. H.; Güttler, B. Anderson transition and intermediate polaron formation in WO_{3-x} – Transport properties and optical absorption. *Philos. Mag. B* **1984**, *50* (5), 607–650.
- [141] He, T. Optical absorption of free small polarons at high temperatures. *Phys. Rev. B* **1995**, *51* (23), 16689–16694.
- [142] Larsson, A.-L.; Sernelius, B. E.; Niklasson, G. A. Optical absorption of Li-intercalated polycrystalline tungsten oxide films: comparison to large polaron theory. *Solid State Ionics* **2003**, *165* (1), 35–41.
- [143] Bryksin, V. V. Optical intraband absorption in disordered systems with a strong electron-phonon interaction. *Sov. Phys. Solid State* **1982**, *24* (4), 627–631.
- [144] Hashimoto, S.; Matsuoka, H. Mechanism of electrochromism for amorphous WO_3 thin films. *J. Appl. Phys.* **1991**, *69* (2), 933–937.
- [145] Green, M.; Travlos, A. Sodium-tungsten bronze thin films: I. Optical properties of dilute bronzes. *Philos. Mag. B* **1985**, *51* (5), 501–520.
- [146] Green, M.; Hussain, Z. Optical properties of dilute hydrogen tungsten bronze thin films. *J. Appl. Phys.* **1991**, *69* (11), 7788–7796.
- [147] Hill, M. D.; Egdell, R. G. The sodium tungsten bronzes: a study of the changes in electronic structure with composition using high-resolution electron spectroscopy. *J. Phys. C: Solid State Phys.* **1983**, *16* (32), 6205–6220.
- [148] Goldner, R. B.; Mendelsohn, D. H.; Alexander, J.; Henderson, W. R.; Fitzpatrick, D.; Haas, T. E.; Sample, H. H.; Rauh, R. D.; Parker, M. A.; Rose, T. L. High near-infrared reflectivity modulation with polycrystalline electrochromic WO_3 films. *Appl. Phys. Lett.* **1983**, *43* (12), 1093–1095.
- [149] Goldner, R. B.; Norton, P.; Wong, K.; Foley, G.; Goldner, E. L.; Seward, G.; Chapman, R. Further evidence for free electrons as dominating the behavior of electrochromic polycrystalline WO_3 films. *Appl. Phys. Lett.* **1985**, *47* (5), 536–538.
- [150] Cogan, S. F.; Plante, T. D.; Parker, M. A.; Rauh, R. D. Free-electron electrochromic modulation in crystalline Li_xWO_3 . *J. Appl. Phys.* **1986**, *60* (8), 2735–2738.
- [151] Arntz, F. O.; Goldner, R. B.; Morel, B.; Hass, T. E.; Wong, K. K. Near-infrared reflectance modulation with electrochromic crystalline WO_3 films deposited on ambient temperature glass substrates by an oxygen ion-assisted technique. *J. Appl. Phys.* **1990**, *67* (6), 3177–3179.
- [152] Svensson, J. S.; Granqvist, C. G. Modulated transmittance and reflectance in crystalline electrochromic WO_3 films: Theoretical limits. *Appl. Phys. Lett.* **1984**, *45* (8), 828–830.

- [153] Wemple, S. H.; DiDomenico, M. Behavior of the Electronic Dielectric Constant in Covalent and Ionic Materials. *Phys. Rev. B* **1971**, *3* (4), 1338–1351.
- [154] Hutchins, M. G.; Abu-Alkhair, O.; El-Nahass, M. M.; El-Hady, K. A. Structural and optical characterisation of thermally evaporated tungsten trioxide (WO_3) thin films. *Mater. Chem. Phys.* **2006**, *98* (2), 401–405.
- [155] Hamberg, I.; Granqvist, C. G.; Berggren, K.-F.; Sernelius, B. E.; Engdtröm, L. Band-gap widening in heavily Sn-doped In_2O_3 . *Phys. Rev. B* **1984**, *30* (6), 3240–3249.
- [156] Hamberg, I.; Granqvist, C. G. Evaporated Sn-doped In_2O_3 films: Basic optical properties and applications to energy-efficient windows. *J. Appl. Phys.* **1986**, *60* (11), R123–R159.
- [157] Jin, Z.-C.; Hamberg, I.; Granqvist, C. G. Optical properties of sputter-deposited ZnO:Al thin films. *J. Appl. Phys.* **1988**, *64* (10), 5117–5131.
- [158] Sernelius, B. E.; Berggren, K.-F.; Jin, Z.-C.; Hamberg, I.; Granqvist, C. G. Band-gap tailoring of ZnO by means of heavy Al doping. *Phys. Rev. B* **1988**, *37* (17), 10244–10248.
- [159] Nakamura, A.; Yamada, S. Fundamental Absorption Edge of Evaporated Amorphous WO_3 Films. *Appl. Phys.* **1981**, *24* (1), 55–59.
- [160] Burstein, E. Anomalous Optical Absorption Limit in InSb . *Phys. Rev.* **1954**, *93* (3), 632–633.
- [161] Moss, T. S. The Interpretation of the Properties of Indium Antimonide. *Proc. Phys. Soc. B* **1954**, *67* (10), 775–782.
- [162] Triana, C. A.; Granqvist, C. G.; Niklasson, G. A. Electrochromism and small-polaron hopping in oxygen deficient and lithium intercalated amorphous tungsten oxide films. *J. Appl. Phys.* **2015**, *118* (2), 024901.
- [163] Deneuve, A.; Gérard, P. Influence of substoichiometry, hydrogen content and crystallinity on the optical and electrical properties of H_xWO_y thin films. *J. Electron. Mater.* **1978**, *7* (4), 559–588.
- [164] de Wijs, G. A.; de Groot, R. A. Structure and electronic properties of amorphous WO_3 . *Phys. Rev. B* **1999**, *60* (24), 16463–16474.
- [165] Wong, H. Y.; Ong, C. W.; Kwok, R. W. M.; Wong, K. W.; Wong, S. P.; Cheung, W. Y. Effects of ion beam bombardment on electrochromic tungsten oxide films studied by X-ray photoelectron spectroscopy and Rutherford back-scattering. *Thin Solid Films* **2000**, *376* (1), 131–139.
- [166] Hussain, Z. Optical constants and electrochromic characteristics of M_xWO_3 bronzes. *Appl. Opt.* **2018**, *57* (20), 5720–5732.
- [167] Yoo, H.-I.; Lee, J.-H.; Martin, M.; Janek, J.; Schmalzried, H. Experimental evidence of the interference between ionic and electronic flows in an oxide with prevailing electronic conduction. *Solid State Ionics* **1994**, *67* (3), 317–322.

- [168] Chebotin, V. N. Coupled Chemical Diffusion of Ions and Electrons in Non-stoichiometric Crystals. *Russ. Chem. Rev.* **1986**, *55* (6), 495–510.
- [169] Yokota, I. On the Theory of Mixed Conduction with Special Reference to the Conduction in Silver Sulfide Group Semiconductors. *J. Phys. Soc. Jpn.* **1961**, *16* (11), 2213–2223.
- [170] Crandall, R. S.; Faughnan, B. W. Measurement of the diffusion coefficient of electrons in WO₃ films. *Appl. Phys. Lett.* **1975**, *26* (3), 120–121.
- [171] Meng, X.; Quenneville, F.; Venne, F.; Di Mauro, E.; Işık, D.; Barbosa, M.; Drolet, Y.; Natile, M. M.; Rochefort, D.; Soavi, F.; Santato, C. Electrolyte-Gated WO₃ Transistors: Electrochemistry, Structure, and Device Performance. *J. Phys. Chem. C* **2015**, *119* (37), 21732–21738.
- [172] Ho, C.; Raistrick, I. D.; Huggins, R. A. Application of A-C Techniques to the Study of Lithium Diffusion in Tungsten Trioxide Thin Films. *J. Electrochem. Soc.* **1980**, *127* (2), 343.
- [173] Zhang, J.-G.; Benson, D. K.; Tracy, C. E.; Deb, S. K. The influence of microstructure on the electrochromic properties of Li_xWO₃ thin films: Part I. Ion diffusion and electrochromic properties. *J. Mater. Res.* **1993**, *8* (10), 2649–2656.
- [174] Lee, S.-H.; Cheong, H. M.; Tracy, C. E.; Mascarenhas, A.; Pitts, J. R.; Jorgensen, G.; Deb, S. K. Alternating current impedance and Raman spectroscopic study on electrochromic a-WO₃ films. *Appl. Phys. Lett.* **2000**, *76* (26), 3908–3910.
- [175] Fabregat-Santiago, F.; Garcia-Belmonte, G.; Bisquert, J.; Ferriols, N. S.; Bueno, P. R.; Longo, E.; Antón, J. S.; Castro-García, S. Dynamic Processes in the Coloration of WO₃ by Lithium Insertion. *J. Electrochem. Soc.* **2001**, *148* (7), E302–E309.
- [176] Garcia-Belmonte, G.; Vikhrenko, V. S.; García-Cañadas, J.; Bisquert, J. Interpretation of variations of jump diffusion coefficient of lithium intercalated into amorphous WO₃ electrochromic films. *Solid State Ionics* **2004**, *170* (1), 123–127.
- [177] Peng-Fei, Y.; Zhong-Hui, C.; Wu-Gang, F.; Xiang-Xin, G. Correlation between lithium storage and diffusion properties and electrochromic characteristics of WO₃ thin films. *Chin. Phys. B* **2013**, *22* (3), 038101.
- [178] Lee, S.-H.; Cheong, H. M.; Tracy, C. E.; Mascarenhas, A.; Pitts, R.; Jorgensen, G.; Deb, S. K. Influence of microstructure on the chemical diffusion of lithium ions in amorphous lithiated tungsten oxide films. *Electrochim. Acta* **2001**, *46* (22), 3415–3419.
- [179] Malmgren, S.; Green, S. V.; Niklasson, G. A. Anomalous diffusion of ions in electrochromic tungsten oxide films. *Electrochim. Acta* **2017**, *247*, 252–257.
- [180] Bohnke, C.; Bohnke, O. Impedance analysis of amorphous WO₃ thin films in hydrated LiClO₄-propylene carbonate electrolytes. *Solid State Ionics* **1990**, *39* (3), 195–204.

- [181] Kumagai, N.; Abe, M.; Kumagai, N.; Tanno, K.; Pereira-Ramos, J. P. Kinetics of electrochemical insertion of lithium into WO. *Solid State Ionics* **1994**, 70-71, 451–457.
- [182] Strømme Mattsson, M. Li insertion into WO₃: Introduction of a new electrochemical analysis method and comparison with impedance spectroscopy and the galvanostatic intermittent titration technique. *Solid State Ionics* **2000**, 131 (3), 261–273.
- [183] Xu, G.; Chen, L. Lithium diffusion in WO₃ films. *Solid State Ionics* **1988**, 28-30, 1726–1728.
- [184] Dini, D.; Decker, F.; Masetti, E. A comparison of the electrochromic properties of WO₃ films intercalated with H⁺, Li⁺ and Na⁺. *J. Appl. Electrochem.* **1996**, 26 (6), 647–653.
- [185] Pyun, S.-I.; Kim, D.-J.; Bae, J.-S. Hydrogen transport through r.f.-magnetron sputtered amorphous and crystalline WO₃ films. *J. Alloys Compd.* **1996**, 244 (1), 16–22.
- [186] Molenda, J.; Kubik, A. Transport properties and reactivity of tungsten trioxide. *Solid State Ionics* **1999**, 117 (1), 57–64.
- [187] Wen, R.-T.; Granqvist, C. G.; Niklasson, G. A. Eliminating degradation and uncovering ion-trapping dynamics in electrochromic WO₃ thin films. *Nat. Mater.* **2015**, 14, 996–1001.
- [188] Wen, R.-T.; Niklasson, G. A.; Granqvist, C. G. Sustainable Rejuvenation of Electrochromic WO₃ Films. *ACS Appl. Mater. Interfaces* **2015**, 7 (51), 28100–28104.
- [189] Arvizu, M. A.; Wen, R.-T.; Primetzhofer, D.; Klemberg-Sapieha, J. E.; Martinu, L.; Niklasson, G. A.; Granqvist, C. G. Galvanostatic Ion Detrapping Rejuvenates Oxide Thin Films. *ACS Appl. Mater. Interfaces* **2015**, 7 (48), 26387–26390.
- [190] Baloukas, B.; Arvizu, M. A.; Wen, R.-T.; Niklasson, G. A.; Granqvist, C. G.; Vernhes, R.; Klemberg-Sapieha, J. E.; Martinu, L. Galvanostatic Rejuvenation of Electrochromic WO₃ Thin Films: Ion Trapping and Detrapping Observed by Optical Measurements and by Time-of-Flight Secondary Ion Mass Spectrometry. *ACS Appl. Mater. Interfaces* **2017**, 9 (20), 16995–17001.
- [191] Wen, R.-T.; Malmgren, S.; Granqvist, C. G.; Niklasson, G. A. Degradation Dynamics for Electrochromic WO₃ Films under Extended Charge Insertion and Extraction: Unveiling Physicochemical Mechanisms. *ACS Appl. Mater. Interfaces* **2017**, 9 (14), 12872–12877.
- [192] Bard, A. J.; Faulkner, L. R. *Electrochemical Methods: Fundamentals and Applications*, 2nd ed.; John Wiley & Sons, Inc.: New York, Chichester, Weinheim, Brisbane, Singapore, Toronto, 2001.
- [193] Gür, T. M. Review of electrical energy storage technologies, materials and systems: challenges and prospects for large-scale grid storage. *Energy Environ. Sci.* **2018**, 11 (10), 2696–2767.

- [194] Brodd, R. J.; Bullock, K. R.; Leising, R. A.; Middaugh, R. L.; Miller, J. R.; Takeuchi, E. Batteries, 1977 to 2002. *J. Electrochem. Soc.* **2004**, *151* (3), K1–K11.
- [195] Gritzner, G.; Kreysa, G. Nomenclature, symbols and definitions in electrochemical engineering (IUPAC Recommendations 1993). *Pure Appl. Chem.* **1993**, *65* (5), 1009–1020.
- [196] Korthauer, R., ed. *Lithium-Ion Batteries: Basics and Applications*, Springer-Verlag GmbH Germany, part of Springer Nature: Berlin, Heidelberg, 2018.
- [197] Nishi, Y. The Dawn of Lithium-Ion Batteries. *J. Electrochem. Soc.* **2016**, *25* (3), 71–74.
- [198] Owen, J. R. Rechargeable lithium batteries. *Chem. Soc. Rev.* **1997**, *26* (4), 259–267.
- [199] Ozawa, K., ed. *Lithium Ion Rechargeable Batteries*, Wiley-VCH Verlag GmbH & Co. KGaA: Weinheim, 2009.
- [200] Betz, J.; Bieker, G.; Meister, P.; Placke, T.; Winter, M.; Schmich, R. Theoretical versus Practical Energy: A Plea for More Transparency in the Energy Calculation of Different Rechargeable Battery Systems. *Adv. Energy Mater.* **2019**, *9* (6), 1803170.
- [201] Quinn, J. B.; Waldmann, T.; Richter, K.; Kasper, M.; Wohlfahrt-Mehrens, M. Energy Density of Cylindrical Li-Ion Cells: A Comparison of Commercial 18650 to the 21700 Cells. *J. Electrochem. Soc.* **2018**, *165* (14), A3284–A3291.
- [202] Liu, K.; Li, K.; Peng, Q.; Zhang, C. A brief review on key technologies in the battery management system of electric vehicles. *Front. Mech. Eng.* **2019**, *14* (1), 47–64.
- [203] Harlow, J. E.; Ma, X.; Li, J.; Logan, E.; Liu, Y.; Zhang, N.; Ma, L.; Glazier, S. L.; Cormier, M. M. E.; Genovese, M.; Buteau, S.; Cameron, A.; Stark, J. E.; Dahn, J. R. A Wide Range of Testing Results on an Excellent Lithium-Ion Cell Chemistry to be used as Benchmarks for New Battery Technologies. *J. Electrochem. Soc.* **2019**, *166* (13), A3031–A3044.
- [204] Nikkei Business Publications. Kyocera to Roll Out New Li-ion Battery in 2020, URL: https://tech.nikkeibp.co.jp/dm/atclen/news_en/15mk/070502951/ (accessed October 17, 2019).
- [205] electrive.com – Industry Service for Electric Mobility. CATL reveals new cell-to-pack platform at IAA, URL: <https://www.electrive.com/2019/09/12/catl-reveals-a-new-product-platform-at-the-iaa/> (accessed October 17, 2019).
- [206] Ellis, B. L.; Lee, K. T.; Nazar, L. F. Positive Electrode Materials for Li-Ion and Li-batteries. *Chem. Mater.* **2010**, *22* (3), 691–714.
- [207] Li, W.; Song, B.; Manthiram, A. High-voltage positive electrode materials for lithium-ion batteries. *Chem. Soc. Rev.* **2017**, *46* (10), 3006–3059.
- [208] Masaki, Y.; Noguchi, H. A Review of Positive Electrode Materials for Lithium-Ion Batteries. In *Lithium-Ion Batteries: Science and Technologies*; Yoshio, M., Brodd, R. J., Kozawa, A., Eds.; Springer Science+Business Media, LLC: New York, 2009; pp 9–48.

- [209] Nazri, G.-A.; Pistoia, G., eds. *Lithium Batteries – Science and Technology*, Springer Science+Business Media, LLC: New York, 2003.
- [210] He, P.; Yu, H.; Li, D.; Zhou, H. Layered lithium transition metal oxide cathodes towards high energy lithium-ion batteries. *J. Mater. Chem.* **2012**, *22* (9), 3680–3695.
- [211] Wenzel, V.; Nirschl, H.; Nötzel, D. Challenges in Lithium-Ion-Battery Slurry Preparation and Potential of Modifying Electrode Structures by Different Mixing Processes. *Energy Technol.* **2015**, *3* (7), 692–698.
- [212] Lee, Y. K. The Effect of Active Material, Conductive Additives, and Binder in a Cathode Composite Electrode on Battery Performance. *Energies* **2019**, *12* (4), 658.
- [213] Kondo, H.; Sawada, H.; Okuda, C.; Sasaki, T. Influence of the Active Material on the Electronic Conductivity of the Positive Electrode in Lithium-Ion Batteries. *J. Electrochem. Soc.* **2019**, *166* (8), A1285–A1290.
- [214] Sun, G.; Sui, T.; Song, B.; Zheng, H.; Lu, L.; Korsunsky, A. M. On the fragmentation of active material secondary particles in lithium ion battery cathodes induced by charge cycling. *Extreme Mech. Lett.* **2016**, *9*, 449–458.
- [215] Chen, Z.; Wang, J.; Chao, D.; Baikie, T.; Bai, L.; Chen, S.; Zhao, Y.; Sum, T. C.; Lin, J.; Shen, Z. Hierarchical Porous $\text{LiNi}_{1/3}\text{Co}_{1/3}\text{Mn}_{1/3}\text{O}_2$ Nano-/Micro Spherical Cathode Material: Minimized Cation Mixing and Improved Li^+ Mobility for Enhanced Electrochemical Performance. *Sci. Rep.* **2016**, *6*, 25771.
- [216] Patel, R. L.; Park, J.; Liang, X. Ionic and electronic conductivities of atomic layer deposition thin film coated lithium ion battery cathode particles. *RSC Adv.* **2016**, *6* (101), 98768–98776.
- [217] Shizuka, K.; Kobayashi, T.; Okahara, K.; Okamoto, K.; Kanzaki, S.; Kanno, R. Characterization of $\text{Li}_{1+y}\text{Ni}_x\text{Co}_{1-2x}\text{Mn}_x\text{O}_2$ positive active materials for lithium ion batteries. *J. Power Sources* **2005**, *146* (1), 589–593.
- [218] Wiedemann, A. H.; Goldin, G. M.; Barnett, S. A.; Zhu, H.; Kee, R. J. Effects of three-dimensional cathode microstructure on the performance of lithium-ion battery cathodes. *Electrochim. Acta* **2013**, *88*, 580–588.
- [219] Wallys, J.; Teubert, J.; Furtmayr, F.; Hofmann, D. M.; Eickhoff, M. Bias-Enhanced Optical pH Response of Group III-Nitride Nanowires. *Nano Lett.* **2012**, *12* (12), 6180–6186.
- [220] Teh, W. H.; Dürig, U.; Drechsler, U.; Smith, C. G.; Güntherodt, H.-J. Effect of low numerical-aperture femtosecond two-photon absorption on (SU-8) resist for ultrahigh-aspect-ratio microstereolithography. *J. Appl. Phys.* **2005**, *97* (5), 054907.
- [221] del Campo, A.; Greiner, C. SU-8: a photoresist for high-aspect-ratio and 3D sub-micron lithography. *J. Micromech. Microeng.* **2007**, *17* (6), R81–R95.
- [222] Youn, S.-W.; Ueno, A.; Takahashi, M.; Maeda, R. Microstructuring of SU-8 photoresist by UV-assisted thermal imprinting with non-transparent mold. *Microelectron. Eng.* **2008**, *85* (9), 1924–1931.

- [223] Melai, J.; Salm, C.; Smits, S.; Visschers, J.; Schmitz, J. The electrical conduction and dielectric strength of SU-8. *J. Micromech. Microeng.* **2009**, *19* (6), 065012.
- [224] Fabian, A.; Elm, M. T.; Hofmann, D. M.; Klar, P. J. Hierarchical structures of magnetic nanoparticles for controlling magnetic interactions on three different length scales. *J. Appl. Phys.* **2017**, *121* (22), 224303.
- [225] Dort, K.; Kroth, K.; Klar, P. J. A surface-enhanced Raman-spectroscopic study: Verification of the interparticle gap dependence of field enhancement by triangulation of spherical gold nanoparticle trimers. *J. Raman Spectrosc.* **2019**. Early View (online version of record before inclusion in an issue), DOI: <https://doi.org/10.1002/jrs.5728>.
- [226] Moslehi, G. B.; Self, S. A. Current flow across a sphere with volume and surface conduction. *J. Electrostat.* **1983**, *14* (1), 7–17.
- [227] Moslehi, G. B.; Self, S. A. Electromechanics of Precipitated Particulate Layers. *IEEE Trans. Ind. Appl.* **1984**, *IA-20* (6), 1598–1606.
- [228] Kvålseth, T. O. Cautionary Note About R^2 . *Am. Stat.* **1985**, *39* (4), 279–285.
- [229] Vértés, Á.; Schiller, R. Concentration-dependent diffusivity: Hydrogen percolation in WO_3 . *J. Appl. Phys.* **1983**, *54* (1), 199–203.
- [230] Zahnow, J. Microcontacting and electrochemical analysis of single CeO_2 -crystallites. Master's thesis, Justus Liebig University, Giessen, 2017.
- [231] Eckhardt, J. K. Implementation of a network for modelling the influence of the microstructure on measured and simulated impedance spectra. Master's thesis, Justus Liebig University, Giessen, 2019.

Appendix

The following chapter provides supporting information on the publications discussed earlier. Additionally to the content, which is also available for download free of charge from the websites of the corresponding journals and reprinted here for the sake of completeness and conformity, details on the specially designed cells developed, manufactured and used are provided.

A Cell Design for Simultaneous Electrochemical and Optical Experiments on Thin Films

The specially customized electrochemical cell used for investigations on lateral hydrogen diffusion in WO_3 thin films was designed to provide an optical path through the working electrode and the liquid electrolyte. Two more components are required to obtain a desired three-electrode-setup that is capable of measuring the potential of the electrolyte near the surface of the working electrode. These are the reference electrode and the counter electrode, which generally are not transparent. This sets additional requirements for their position with respect to the optical path and the design of the cell.

The transparent sample is mounted in the cell such that the patterned surface faces toward the cell housing, while two O-rings above and below the sample protect it and seal the cell. The O-ring below the sample, as well as the hole in the center of the plastic plate underneath confine the optical path as illustrated in figure A.1 (left). The O-ring above the sample defines the geometric surface area of the working electrode/sample, which will be in contact with the liquid electrolyte, as implied by the shadow on the sample surface. The sample is mounted to the bottom side of the polyether ether ketone (PEEK) housing (see figure A.1 (right)) to enable the imaging of the sample surface through the transparent substrate by an objective and a subtractive double spectrometer. The gold film on one side of the sample surface is contacted by a wire during assembly.

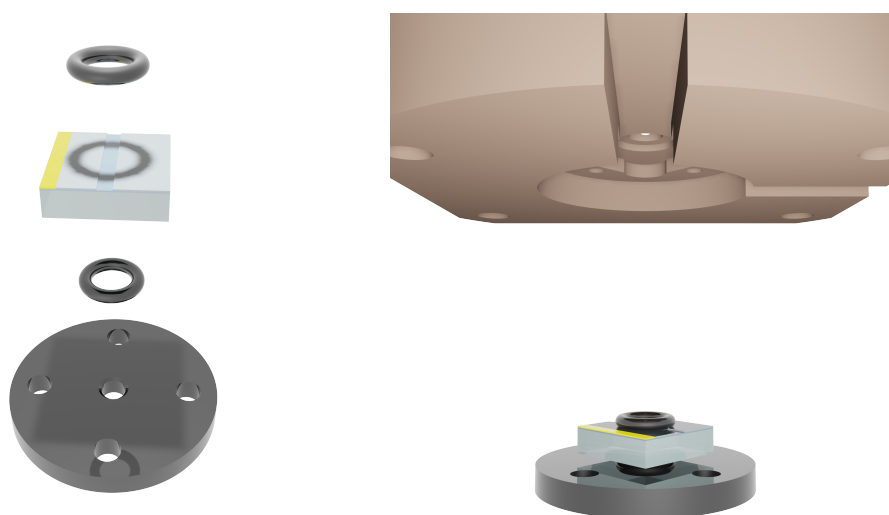


Figure A.1: Exploded view of the components along of the optical path. The hole in the plastic plate defines the field of vision. The electrode area of the patterned sample is visualized by a blue stripe on the sample surface. The O-ring above the sample (see also shadow on the sample surface) defines the area in contact with the electrolyte (left). These components are mounted to the bottom side of the PEEK housing, which leads to the formation of a contact between a wire (not depicted here) and the gold film on top of the sample surface (right).

The PEEK housing has a hole in its center that allows a direct view on the patterned surface of the sample. This view is illustrated in figure A.2 (left). Under experimental conditions, the volume above the sample surface, which is confined by the PEEK housing, is filled with a liquid electrolyte. The light must therefore pass through the electrolyte. This aspect itself does not require the electrochemical cell to be sealed, if the electrolyte is stable at ambient conditions. However, a plane electrolyte surface in the optical path is desired to reduce scattering effects and increase the quality of the imaging process. For this purpose, the top side of the PEEK housing is sealed by a fused silica window with an anti-reflective coating (purchased from Edmund Optics) as depicted in figure A.2 (right).

The desired three-electrode-setup requires a counter and a reference electrode to be added, while the extent to which these occupy the optical path should be minimized. Two ducts in the PEEK housing (see figure A.2 (left)) connect the volume above the sample surface to the outside, where two additional PEEK components can be mounted. These components serve two purposes. On the one hand, they act as inlet and outlet during the filling of the cell with the liquid electrolyte. On the other hand, they contain the counter electrode or enable the reference electrode to be mounted. The counter electrode is realized by a platinum tube, which is fixed inside the electrolyte inlet depicted in figure A.3 (left). A Drifref-450 Ag/AgCl-reference electrode (purchased from World Precision Instruments) is mounted to an additional PEEK component, which also contains the electrolyte outlet, as illustrated in figure A.3 (right). The reference electrode is inside the black PEEK component.

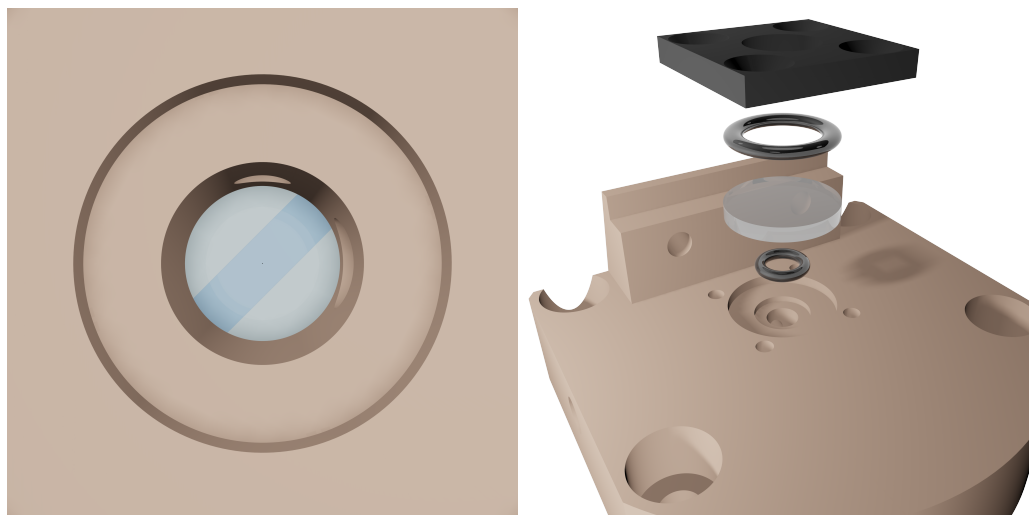


Figure A.2: Top view through the hole in the center of the PEEK housing onto the surface area of the patterned sample that is exposed to a liquid electrolyte (left) and an exploded view on the components that seal this hole under experimental conditions (right).

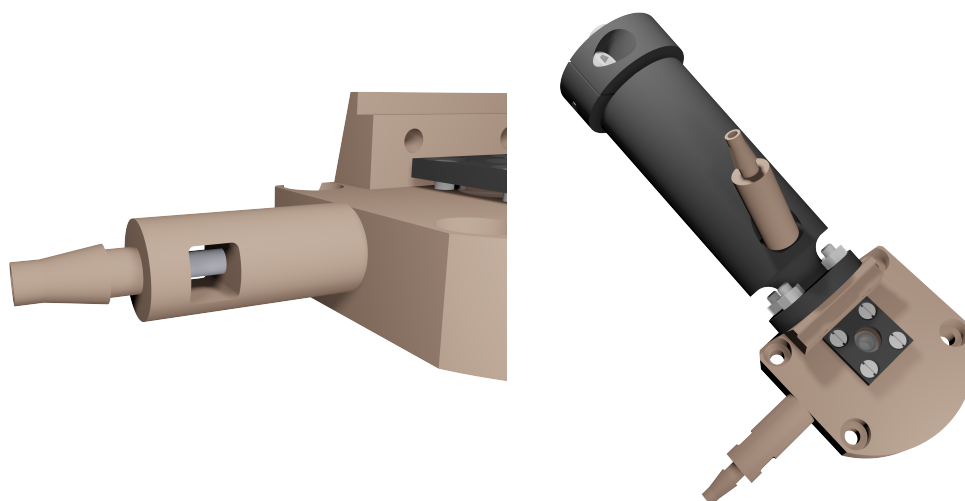


Figure A.3: Inlet and outlet used for filling of the cell with the liquid electrolyte. The inlet contains a platinum tube used as counter electrode (left) and the outlet is mounted to the PEEK component, containing a Driref-450 Ag/AgCl-reference electrode (purchased from World Precision Instruments).

By fully assembling the cell and filling it with a liquid electrolyte, the tip of the reference electrode, which has a diameter of $450\ \mu\text{m}$, is in close proximity to the surface of the working electrode and immersed in the liquid electrolyte. This means, the tip of the reference electrode protrudes slightly into the optical path, allowing the major part of the sample surface to be investigated. The measurement configuration realized under experimental conditions is illustrated in figure A.4, where the PEEK housing above the sample, as well as the PEEK component of the electrolyte inlet are omitted.

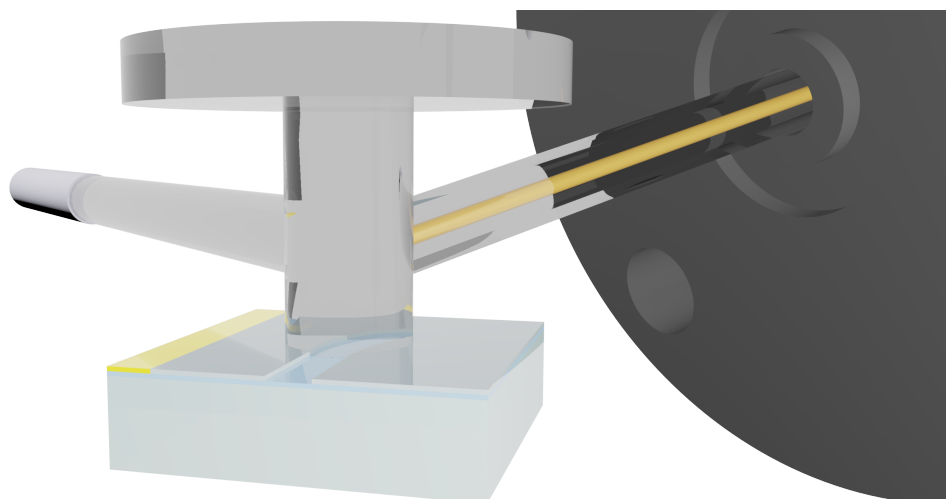


Figure A.4: Measurement configuration inside the electrochemical cell used for monitoring lateral hydrogen diffusion in WO_3 thin films. The optical path goes through a fused silica window, a liquid electrolyte and the patterned sample. A platinum tube and a Driref-450 Ag/AgCl-reference electrode serving as counter and reference electrode, respectively, are positioned outside the optical path.

B Supporting Information on Publication 1

In Situ Monitoring of Lateral Hydrogen Diffusion in Amorphous and Polycrystalline WO_3 Thin Films

Simon Burkhardt, Matthias T. Elm, Bernhard, Lani-Wayda, and Peter J. Klar

X-ray Diffraction Data

X-ray Diffraction Measurements on WO_3 Thin Films after Different Post-Deposition Treatments

Figure S1 depicts the results obtained in XRD experiments on WO_3 thin films, which have been heated to different temperatures in air after thin film deposition onto silicon $\langle 100 \rangle$ wafers. During heat treatment, the temperature increased from room temperature with a heating rate of 100°C h^{-1} to the desired temperature. As the temperature was reached, it was held for one hour before the oven cooled down to room temperature again. Experiments have been performed using a PANalytical EMPYREAN diffractometer equipped with a PIXcel^{3D} detector and a copper anode ($\lambda(\text{CuK}_\alpha) = 1.541 \text{ \AA}$). While no diffraction reflexes originating from a WO_3 thin films as received after deposition can be observed, the diffraction patterns obtained from WO_3 thin films after the heat treatment show additional diffraction reflexes and thus clearly indicate increased crystallinity.

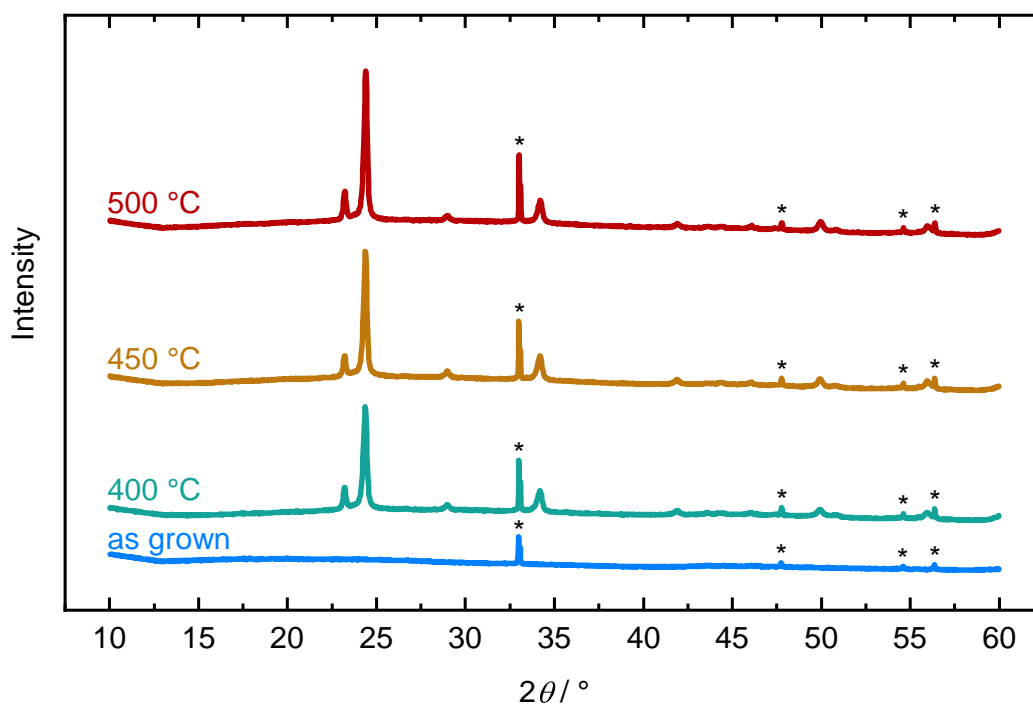


Figure S1: X-ray diffraction patterns of WO₃ thin films as grown and after a heat treatment at 400 °C, 450 °C or 500 °C, respectively. Asterisks mark diffraction angles of silicon <100> wafers used as substrate.

Scanning Electron Microscopy Images Before and After the Heat Treatment

Figure S2 shows scanning electron microscopy images of WO₃ thin film surfaces before and after a heat treatment at 450 °C.

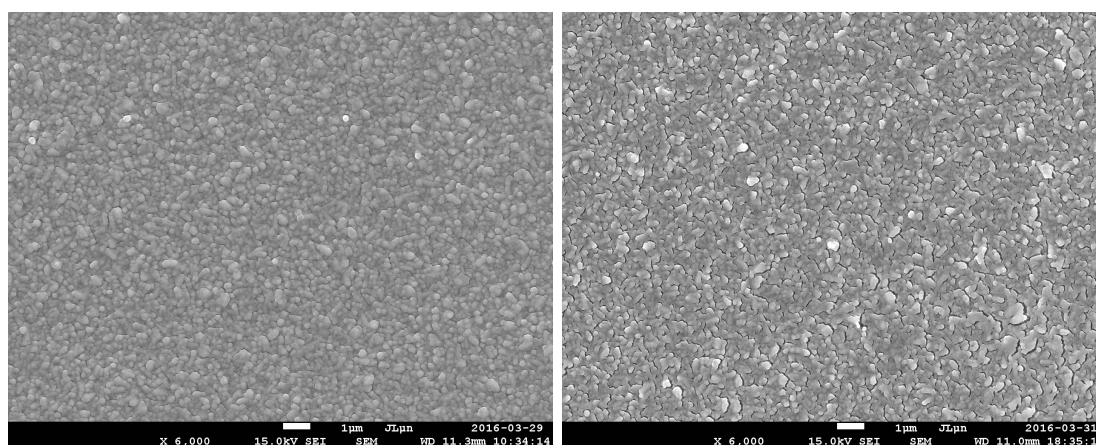


Figure S2: Scanning electron microscopy images of WO₃ thin film surfaces before (left) and after (right) a heat treatment at 450 °C.

Numerical Simulations

Remarks on the implementation of the model

Experimental data for the absorbance A_e gathered in the gap area of the PMMA film have been used in numerical simulations to preset the concentration at $x = 0$, whereas at $x = L$, linear extension has been used. The spatial discretization of the simulation grid used was equal to the size of a pixel of the CCD sensor (0.645 μm), which turned out to be sufficiently fine. For the numerical integration of the nonlinear diffusion equation an Euler scheme of the form

$$c(t + dt) = c[i](t) + c^{(1)}[i], \quad i = 1, \dots, L, \quad (\text{S1})$$

with a suitably small time step dt (typically corresponding to about 0.01 s) was used, where $c^{(1)}[i]$ is a numerically calculated value for the right hand side of Equation 5. Square brackets as in ' $c[i]$ ' are used to describe the discrete representation of quantities in the computer simulation. The calculation of the right hand side of Equation 5 has to be implemented in a way that avoids artificial oscillatory behavior induced by the discretization^[1].

The simulation can be summarized as follows:

- 1) $D(c)$ at index i is not directly computed as the function $D(c[i])$, but as $D(\bar{c}[i])$, where $\bar{c}[i]$ is a local average of c around the index i , typically involving three adjacent data points to the left and the right.
- 2) Derivatives (appearing two times on the right hand side of Equation 5) are in principle evaluated as difference quotients in the form

$$da[i] = \frac{a[i + 1] - a[i - 1]}{2\Delta x} \quad (\text{S2})$$

for an array a of numbers. A local averaging procedure in a discrete version of the formula

$$\bar{a}(x) = \int_{-\infty}^{\infty} P(|x - y|) a(y) dy, \quad (\text{S3})$$

with a narrowly concentrated Gaussian distribution P has been applied. The parameters p and q were optimized along with the parameters c_0 , D_i , and D_f . All these parameters together determine the behavior of the simulated diffusion coefficient. These have been fitted to the experimental data, such that the total sum of squared errors

$$S = \sum_{j=1}^N \sum_{i=1}^L |A_e(t_j, x_i) - c[t_j, i]|^2 \quad (\text{S4})$$

became minimal, where t_j are the N times at which the experimental data $A_e(t_j, x_i)$ were used, and $c[t_j, i]$ are the corresponding computed concentration values. A test of the integration scheme by an example with constant diffusion coefficient and analytically known solutions gave satisfactory results. The procedure was implemented using ETH

Oberon (see, e.g., <https://www.inf.ethz.ch/personal/wirth/Oberon/Oberon07.Report.pdf>). Detailed code is available upon request.

References

- [1] J. Crank, *The mathematics of diffusion* (2nd edition), Clarendon Press, Oxford, 1975.

C Cell Design for Investigations on Single Particles

The special design of the cell used for investigations on single secondary particles consists of four essential parts, which are all made of PEEK. The bottom plate comprises a square-shaped notch and a spherical recess in its center. This is, where the square-shaped and patterned sample, which contains the single particles that are immobilized at defined positions, is mounted. It is placed on top of a fluorocarbon-based synthetic rubber O-ring to protect the sample from breaking during cell assemblage. Once placed inside the square-shaped notch, the sample can be fixed by tightening a screw and thereby clamping the sample. The bottom part together with the sample in an elevated position are depicted on the left-hand side of figure C.1. The middle part of the cell consists of two components. The outer component is mounted to the bottom plate and thereby deforms an O-ring on top of the sample to seal the cell. It also exhibits a central recess for the contact-forming inner component and several tapped holes at the sides for gas-tight bushings. The outer component is depicted on the right-hand side of figure C.1.

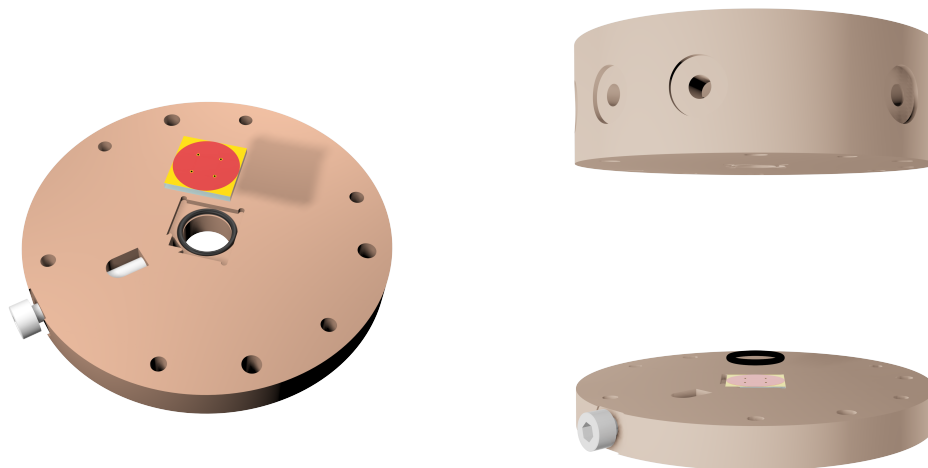


Figure C.1: Two components of the specially designed cell used for investigations of single secondary particles. The sample is placed and fixed in a square-shaped notch in the bottom plate (left). The outer component of the middle part comprises a central recess for contacting the square-shaped sample at defined positions and is mounted to the bottom plate (right).

The outer component of the middle part also provides four contacts. Four copper cylinders form a contact to the metal film underneath the patterned SU-8 layer at the corners of the sample. These cylinders enable the bottom contact to the particles. A spring-loaded

suspension that allows a certain adjustment of the pressure exerted to the sample was realized by a wire.

The inner component of the middle part is mounted to the outer one and forms five individual contacts to defined positions on the sample surface. Four stainless steel cylinders contact the sample at the positions of the particle traps. They form the top contact to the particles. The diameter of the circular area of the top contacts is 1 mm. This allows the formation of the top contact to particles, even if a certain misalignment between the patterned structure and the glass substrate is present. Prior to cell assemblage, the bottom side of the stainless steel cylinders was coated with the same metal used for the bottom contact to the particles. Doing this, a symmetric cell configuration was realized. The top side of the steel cylinders provides an opening for a soldered cable connection to hexagonal copper prisms. In these intermediate contacting points, pins, which are usually used for integrated circuits, were inserted. Two versions of this inner component have been developed. One of them exhibits steel cylinders for the top contact, which are vertically fixed. In a modified version, these cylinders are not fixed, but loose. The cylinders can be lowered by tightening spring-loaded plastic pressure pins with external threads. In both versions, a spring-loaded contact to the center of the substrate was included to enable the use of a currentless reference electrode in experiments with half-cell setups. It is located in the center of this component. Both versions of this component, as well as four copper cylinders for the bottom contact are depicted in figure C.2.

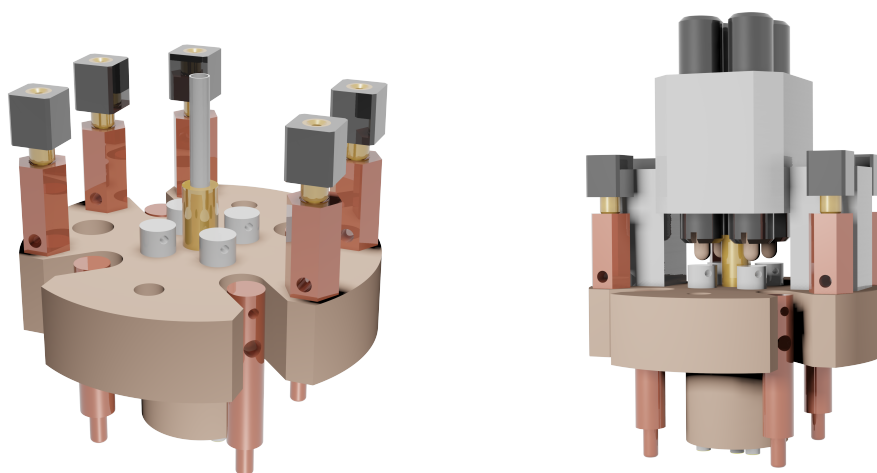


Figure C.2: Two different contact forming components for investigations of single particles. In an early version (left), the cylinders for the top contact to single particles or particle arrangements were pressed and fixed in the PEEK body, while in an advanced version (right) plastic pressure pins with a hexagon socket enable the adjustment of the pressure exerted by the top contact.

As depicted on the left-hand side of figure C.3, the recesses in the outer component of the middle part match the corners of the sample and the positions of the particle traps. After fully assembling the middle part of the cell, nine individual contacts to the sample protrude from the bottom side of the outer component of the middle part, as illustrated

on the right-hand side of figure C.3.

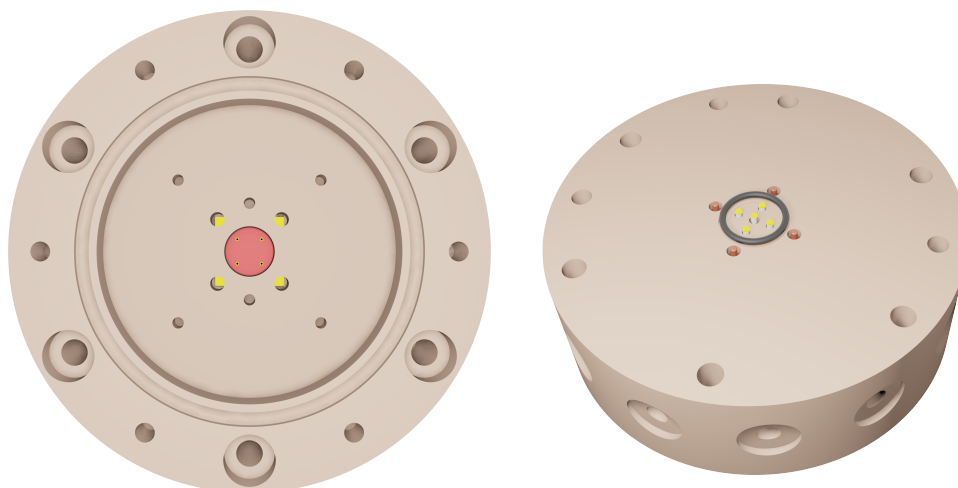


Figure C.3: Top view onto the surface of the sample through recesses in the outer component of the middle part (left) and the nine individual contacts to different points of the sample, which protrude from the bottom side of this part after one of the inner components depicted in figure C.2 is inserted (right).

After the middle part is mounted to the bottom part, each corner of the sample, as well as each particle trap and the center of the sample are contacted individually, as indicated in figure C.4.

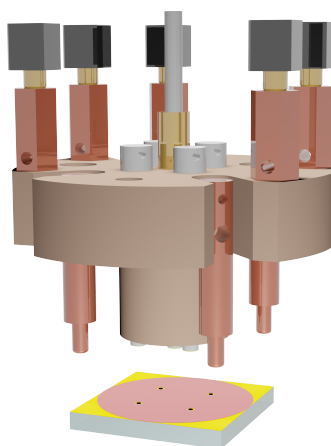


Figure C.4: Inner component of the middle part above a sample, which is contacted at nine individual positions.

An optional top part of the cell was designed to seal it. This was intended to enable experiments outside the protective atmosphere in which the assemblage took place. The cell design also allows additional experiments on single particles in a half-cell setup. For this purpose, a dried separator can be placed on top of the sample and soaked with an electrolyte after the arrangement of the particles. A circular piece of lithium-foil can be attached to the bottom of the stainless steel cylinders and the contact pin for the reference electrode to obtain a half-cell setup with a single particle as the active material.

D Supporting Information on Publication 2

Charge Transport in Single NCM Cathode Active Material Particles for Lithium-Ion Batteries Studied under Well-Defined Contact Conditions

Simon Burkhardt, Markus S. Friedrich, Janis K. Eckhardt, Amalia C. Wagner, Nicole Bohn, Joachim R. Binder, Limei Chen, Matthias T. Elm, Jürgen Janek, and Peter J. Klar

Experimental Methods

Preparation of Particle Traps on Patterned Substrates

A glass substrate as well as the bottom faces of four cylindrical steel contact pins with a diameter of 1 mm were coated with a 200 nm to 250 nm thin film of either gold or copper. After metal film deposition, an SU-8 film was patterned photolithographically on top of the substrate using the following procedure:

The substrate was covered with 0.5 mL of SU-8 10 (purchased at MicroChem Corp.) and rotated first with 500 rpm for 10 s and subsequently with 1750 rpm for 45 s to yield a homogeneous resist film. After spin coating, the sample was heated on top of a hot plate for 120 s at 65 °C and for 300 s at 95 °C. The resist was exposed through a specially designed mask with a pattern, comprising four circles with diameters of 35 μm at defined positions acting as particle traps. Exposure was performed with UV radiation with a wavelength of 365 nm for 22 s. The sample was heated on a hot plate for 60 s at 65 °C and for 120 s at 95 °C before the resist was developed in mr-Dev 600 (purchased at micro resist technology, <https://www.microresist.de/>) for 240 s. The particle traps obtained penetrated the SU-8 layer completely revealing the underlying metal film at the bottom of the trap. The processed resist film thickness varied between 6 μm and 16 μm.

Preparation of Nanostructured Secondary Particles and Powder Characterization

NCM 111 secondary particles have been synthesized and characterized according to the procedure reported earlier.¹ Li(Ni_{1/3}Co_{1/3}Mn_{1/3})O₂ (NCM 111) powder from Toda Kogyo Corp. (NM-3100, Lot. No. 6200613) was suspended in deionized water with Darvan 821A (Vanderbilt Minerals) as dispersant and milled in an agitator bead mill (LabStar LS1, Netzsch) with Y-stabilized ZrO₂ beads of 0.2 mm diameter at 3000 rpm. The grinding process was monitored by laser diffraction in order to determine particle size distribution and was stopped at around 220 nm mean particle size ($d_{50,3}$). After milling 0.25 wt% polyethylene glycol 400 (Sigma Aldrich) was added to the aqueous suspension and subsequently, it was spray dried at 115 °C (MobileMinor, GEA). The as-obtained powder was calcined at 900 °C for 5 h under pressured air with a flowrate of 300 L min⁻¹ at heating and cooling rates of 5 K min⁻¹ and 10 K min⁻¹, respectively. Afterwards granulates were sieved (<45 μm) resulting in a mean secondary particle diameter of 16.4 μm, a specific surface area of 2.52 m² g⁻¹, calculated mean primary particle sizes of 500 nm, and a granulate porosity of 40.6 % determined from mercury intrusion measurements. XRD analysis proved the existence of phase pure NCM 111.

Particle Arrangement, Cell Assemblage and Impedance Measurements

Single NCM 111 secondary particles were dispersed in propylene carbonate (purchased at Sigma-Aldrich) and then arranged in the particle traps by using a variant of the meniscus force method²⁻⁵ or simply placing them on a tilted surface. Remaining propylene carbonate was removed by a heat treatment at 100 °C for 5 min. Once the secondary particles were arranged, substrate and steel cylinders were transferred into an argon-filled glove box. After cell assembling, both, the metal surfaces of the substrate and the bottom face of one steel cylindrical contact pin formed a contact to a single secondary particle. Impedance measurements with an amplitude of the AC signal of 50 mV or 200 mV and frequencies between 60 MHz and 0.1 Hz or 1 Hz were carried out with a bio-logic SP300 potentiostat. The simulation of the spectra based on the equivalent circuit shown in Figure 3 were performed using the commercial software RelaxIS 3 (version 3.0.11.12, rhd instruments GmbH & Co. KG)

Impedance Spectra of Different Configurations

To ensure that the measured impedance response contains separable contributions of the secondary particle in a particle trap and is not dominated solely by the measurement system, different ‘plate capacitor configurations’ have been realized in the electrochemical cell. The following configurations between two gold contacts were studied: solely argon (1), solely SU-8 polymer (2), a single NCM 111 secondary particle with a particle radius of 7.7 μm in an SU-8 trap (3) and a loose agglomerate of many NCM 111 secondary particles (4). In these experiments, the amplitude of the AC signal was 200 mV. The Nyquist diagram of the impedance measurements performed in these configurations is depicted in Figure S1.

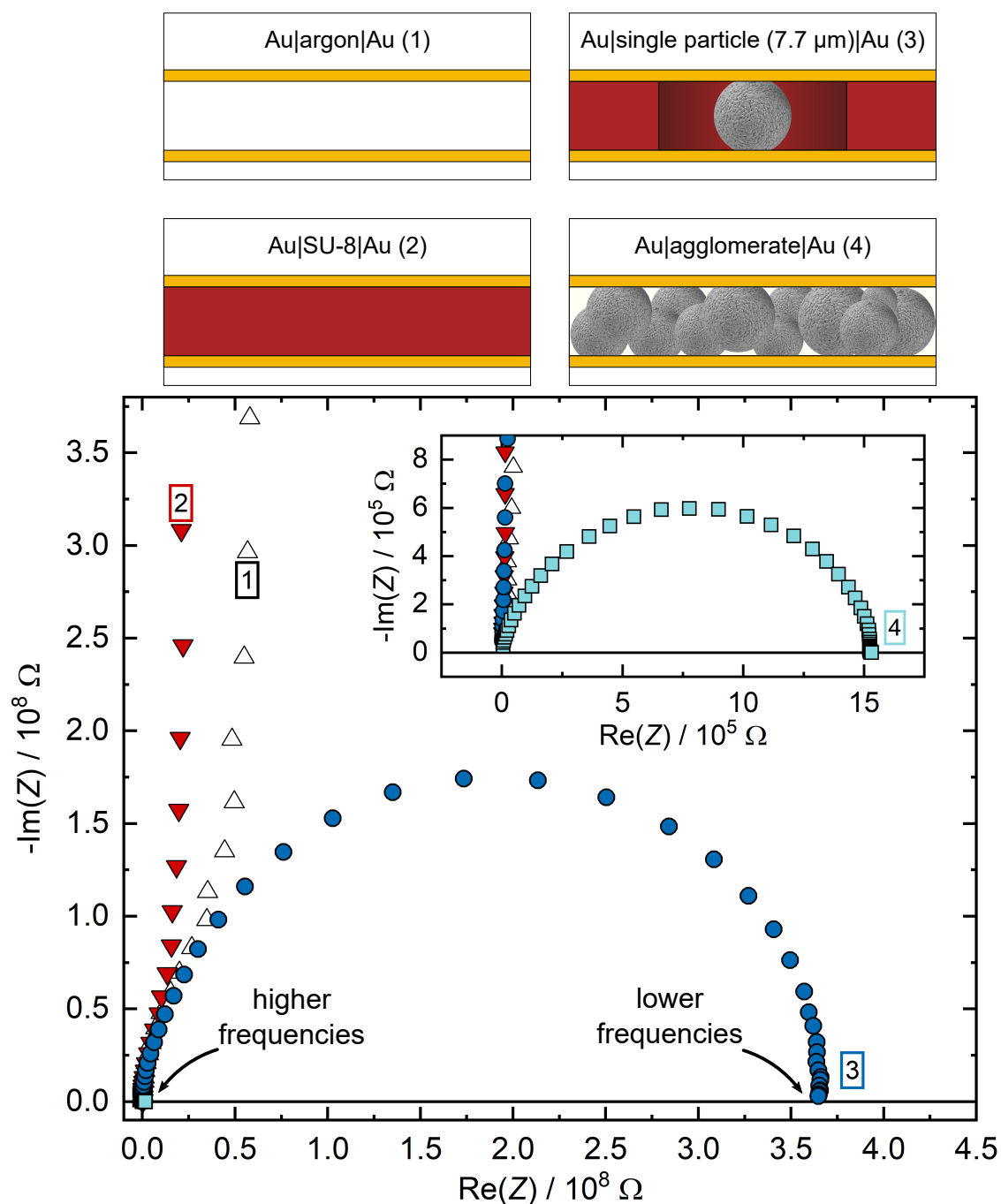


Figure S1: Nyquist representation of the impedance spectra measured with argon (white filled upright triangles), an SU-8 polymer film (red filled upside down triangles), a single NCM 111 secondary particle (blue filled circles) and a loose agglomerate of NCM 111 secondary particles (cyan filled squares) between two gold contacts.

The contributions of the different materials of the cell present during the electrochemical experiments to the measured impedance can clearly be distinguished. Even though, the complex impedance is similar in all configurations at high frequencies (small values for the real and imaginary part of the complex impedance), implying a contribution of the cell setup connected to the samples, clear differences between experiments with and without NCM 111 secondary particles between the gold electrodes can be distinguished at low

frequencies on the right-hand side of the Nyquist plot. The impedance spectra obtained without NCM 111 between the two gold electrodes show a typical capacitor-like behavior that manifests itself in a steep increase of the complex impedance's negative imaginary part with decreasing frequency. The electric field generated across argon or SU-8 is of the order of $10^{-2} \text{ V } \mu\text{m}^{-1}$ and thus too low to lead to a breakdown or a measurable current.⁶ In contrast to that, the presence of either a single NCM 111 secondary particle or an agglomerate of NCM 111 secondary particles closes the electric circuit and leads to a vanishing negative imaginary part at low frequencies. This and the fact that the shape of the impedance spectra obtained from a single NCM 111 secondary particle and the loose particle agglomerate qualitatively match very well, ensures, that the impedance measured in single particle measurements can be related to the material investigated and are not an artifact of the cell setup.

DC Polarization of a Single Secondary Particle

DC polarization of a single secondary particle ($r_p = 9.30 \mu\text{m}$) between two copper electrodes was carried out by applying a current of $(4.362 \pm 0.011) \text{ nA}$ and measuring the potential as a function of time as depicted in Figure S2. Due to ion blocking at the interfaces between the secondary particle and the inert electrodes, the steady-state current is purely electronic. The difference between the open cell potential and the initial potential under DC polarization is $U = (630 \pm 1) \text{ mV}$ which leads to a DC resistance of $R_{\text{DC}} = (144 \pm 2) \text{ M}\Omega$. It should be noted that the measured potential difference under DC polarization might be larger once the electronic charge transfer is hindered, e.g. by Schottky-type contacts. The chemical polarization of the particle and the created concentration gradient of lithium ions leads to diffusion of lithium ions and to a decrease in potential by approximately 19 mV after 12 h. The low-frequency impedance of the same secondary particle is $R_{\text{low freq}} = (159.6 \pm 0.6) \text{ M}\Omega$, which is slightly higher, but the deviation is still below 10 % and probably arises due to the resolution of the measurement setup.

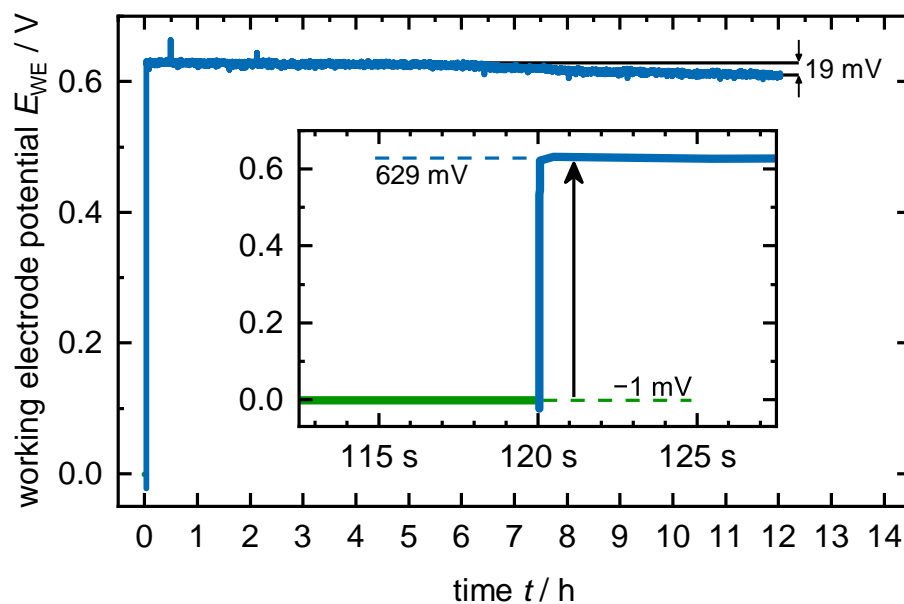


Figure S2: DC polarization curve of a single NCM 111 secondary particle with a radius of $9.30 \mu\text{m}$. The polarization current of 4.362 nA leads to an initial increase of the steady-state-potential of 630 mV . Due to chemical polarization of the material and subsequent diffusion of lithium ions the potential is decreases by approximately 19 mV after 12 h .

Modeling

To describe the radius-dependence of the electronic and ionic resistances of NCM 111 secondary particles, a model for the resistance of a sphere with finite contact area is employed.^{7,8} The model structure is schematically depicted in Figure S3. It assumes the potential distribution of a homogeneous sphere with a radius r_p and a finite and non-vanishing surface resistance R_{surf} and volume resistivity ρ_{bulk} as a starting point.

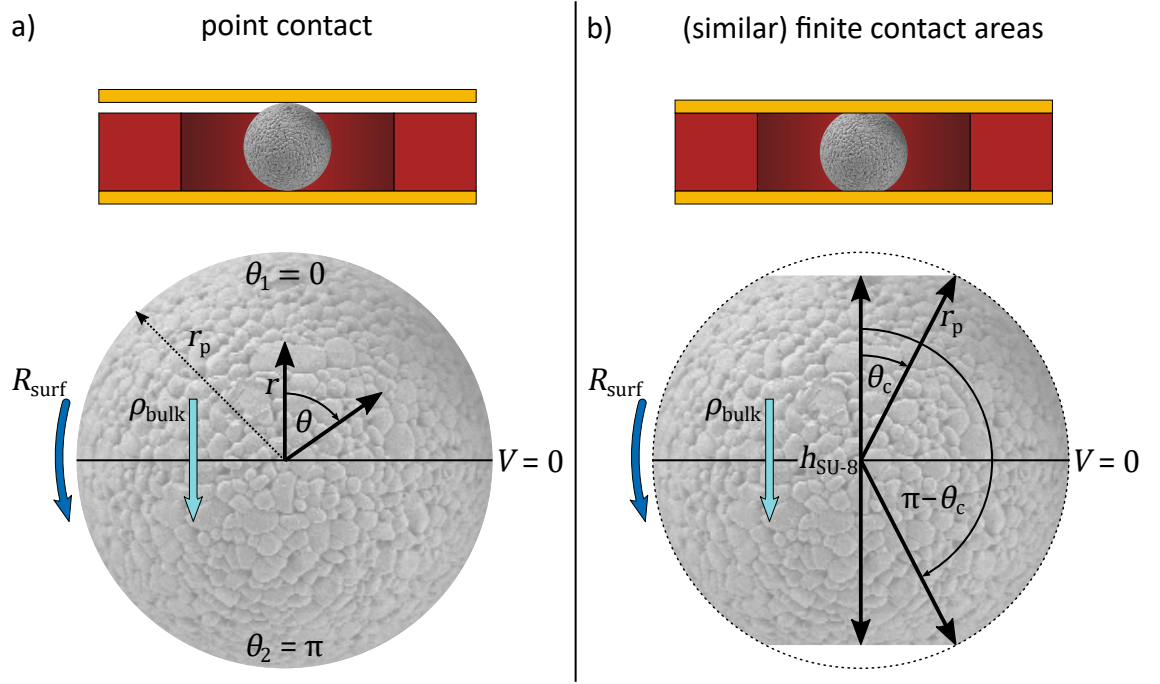


Figure S3: Visualization of the model applied for simulating the resistance of secondary particles starting from a point contact at the poles (a). Symmetric truncation of the secondary particles due to the pressure applied by contacting planes was assumed, to obtain a correlation between the secondary particle radius, the height of SU-8 film and the contact angle θ_c (b).

For a current I entering the sphere at point contacts located at the poles of the sphere ($\theta_1 = 0$ and $\theta_2 = \pi$ in polar coordinates), the potential distribution across the sphere is described by

$$V(r, \theta) = \frac{\rho_{\text{bulk}} \cdot I}{4 \cdot r_p} \cdot F(R_{\text{rat}}, z, \mu) \quad (\text{S1})$$

where $R_{\text{rat}} = R_{\text{surf}} \cdot r_p / \rho_{\text{bulk}}$ is a dimensionless resistivity ratio, $z = r/r_p$ and $\mu = \cos(\theta)$. The integral form of the function $F(R_{\text{rat}}, z, \mu)$ was used for the simulations (see equations (27) and (28) in reference 7).⁷ It should be noted that the derivation of Eq. (1) requires the assumption of a small contact area and does not hold for an ideal point contact.

However, if a finite contact area is assumed a finite resistance of the sphere can be calculated. We assume a deformation of the secondary particles due to the pressure applied by the contacting planes (see Figure S3b). The deformation is approximated by a symmetric truncation of the secondary particles, which defines a contact angle $\theta_c (= \theta_{c,1} = \theta_{c,2})$ in terms of the average height of the SU-8 layer $h_{\text{SU-8}}$ and the radius of the secondary particles r_p as

$$\theta_c(r_p, h_{\text{SU-8}}) = \arccos\left(\frac{h_{\text{SU-8}}}{2r_p}\right) \quad (\text{S2})$$

The resulting ohmic resistance R between two points at the surface can be approximated by the ratio of the potential difference ΔV between the contact points at which the current

is entering ($\theta = \theta_1$) and leaving ($\theta = \theta_2$) the sphere and the current itself leading to⁸

$$R(r_p, \theta_1, \theta_2) = \frac{\rho_{\text{bulk}}}{4r_p} \cdot [F(R_{\text{rat}}, 1, \cos(\theta_2)) - F(R_{\text{rat}}, 1, \cos(\theta_1))] \quad (\text{S3})$$

In our simple model of finite contact areas, the angles θ_1 and θ_2 are equal to θ_c and $\pi - \theta_c$. This together with the symmetric properties of the cosine function allows to simplify equation (3) to

$$R(r_p, \theta_c) = \frac{\rho_{\text{bulk}}}{2r_p} \cdot F(R_{\text{rat}}, 1, \cos(\theta_c)) \quad (\text{S4})$$

Using Eq. (1) to derive the potential at the contact areas in Eq. (3) is an approximation because the equipotential surfaces that result from the derivation of the model applied are curved apart from that at the sphere's equator,⁷ which is not fully displayed by assuming horizontal truncation. The fitting parameters used in the least-squares fitting are the surface resistances $R_{\text{e,surf}}$ and $R_{\text{i,surf}}$, the bulk resistivities $\rho_{\text{e,bulk}}$ and $\rho_{\text{i,bulk}}$ of NCM 111, as well as the average height of the SU-8 polymer film $h_{\text{SU-8}}$.

Interpretation of the Surface Resistance

Due to the geometry assumed, the correlation between the surface resistance R_{surf} of a sphere⁹, which is

$$R_{\text{surf}} = \frac{\rho_{\text{surf}}}{2\pi} \int_{\theta_c}^{\pi-\theta_c} \frac{1}{\sin(\theta)} d\theta \quad (\text{S5})$$

and the corresponding surface conductivity σ_{surf} is given by

$$\sigma_{\text{surf}} = \frac{1}{2\pi \cdot d \cdot R_{\text{surf}}} \cdot \ln \left(\frac{\tan\left(\frac{\pi - \theta_c}{2}\right)}{\tan\left(\frac{\theta_c}{2}\right)} \right) \quad (\text{S6})$$

where d is the thickness of a spherical shell, in which charge transport takes place exclusively and θ_c is the angle of the contact areas at the poles.⁹

Raman Spectroscopy

Raman spectra have been acquired using a Renishaw in Via Raman microscope system employing an edge filter for suppression of the Rayleigh-scattered light and a single-monochromator equipped with a charge-coupled device detector for detecting the spectrally dispersed Raman scattered light in the relative wavenumber range from 100 cm^{-1} to 1200 cm^{-1} . The spectral resolution of the system is better than 1 cm^{-1} in this range. An Ar-ion laser operating at 488 nm was used for excitation. The laser beam with a power of less than 1 mW was focused to a spot with a diameter of $1 \mu\text{m}$ on the particle surface. The Raman scattered light was detected in a backscattering geometry without polarization

optics. The spectra displayed in Figure S4 have been normalized to the intensity of the mode at 595 cm^{-1} and stacked for comparison.

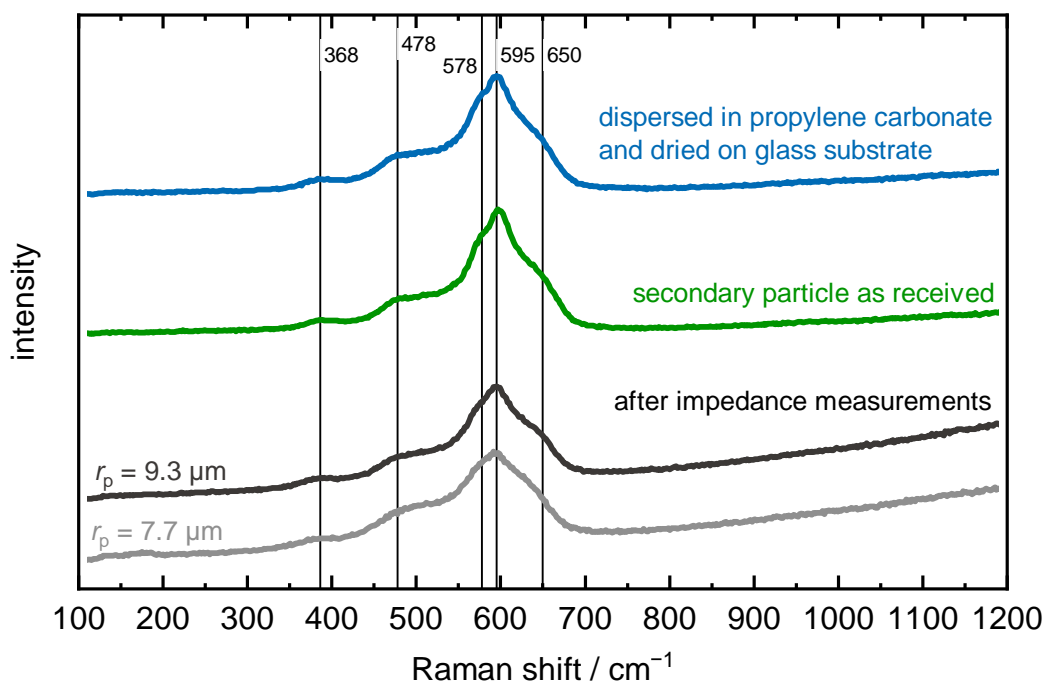


Figure S4: Normalized Raman spectra obtained from NCM 111 secondary particles as received (green), after dispersion in propylene carbonate and drying on a glass substrate (blue) and after impedance measurements on secondary particles with radii of $7.7\text{ }\mu\text{m}$ (gray) and $9.3\text{ }\mu\text{m}$ (dark gray) have been performed.

The Raman spectra obtained from NCM 111 secondary particles as received show modes at 368 cm^{-1} , 478 cm^{-1} , 578 cm^{-1} , 595 cm^{-1} , and 650 cm^{-1} and are in good agreement with results from other groups.¹⁰⁻¹³ Spectra obtained from both, a secondary particle after dispersion in propylene carbonate and drying on a glass substrate, as well as secondary particles after impedance measurements show the same modes without any signatures of other vibrations.

Profilometric Investigation of the Sample Surface

Height profiles of the samples investigated have been measured using a DektakXT Stylus Profiler from Bruker Corporation. A typical height profile along the diagonal of a sample after particle arrangement is shown in Figure S5a. The height of all the SU-8 layers investigated varied between $6\text{ }\mu\text{m}$ and $16\text{ }\mu\text{m}$. The peaks in the profile of Figure S5a originate from secondary particles lying on top of the SU-8 layer. Figure S5b shows a profile across a particle trap and indicates, that SU-8 has been removed completely during the development of the exposed resin. Figure S5c depicts the approximate height of the SU-8 layer near the positions of the particle traps containing the secondary particles investigated in this work. Due to the macroscopic size of the contacting pin and the roughness and unevenness of the SU-8 layer, the exact height of the SU-8 layer determining the distance between both contacting planes cannot be determined accurately. The dashed line visu-

alizes the boundary condition for single particle measurements via our approach, namely the diameter of the secondary particles must exceed the height of the SU-8 layer. As can be seen in Figure S5c, this holds for all the measurements performed. Furthermore, the height of the SU-8 layer obtained during the fitting procedure of the electronic and ionic resistances as a function of the particles' radii is in accordance with the experimental values obtained by the height profiling.

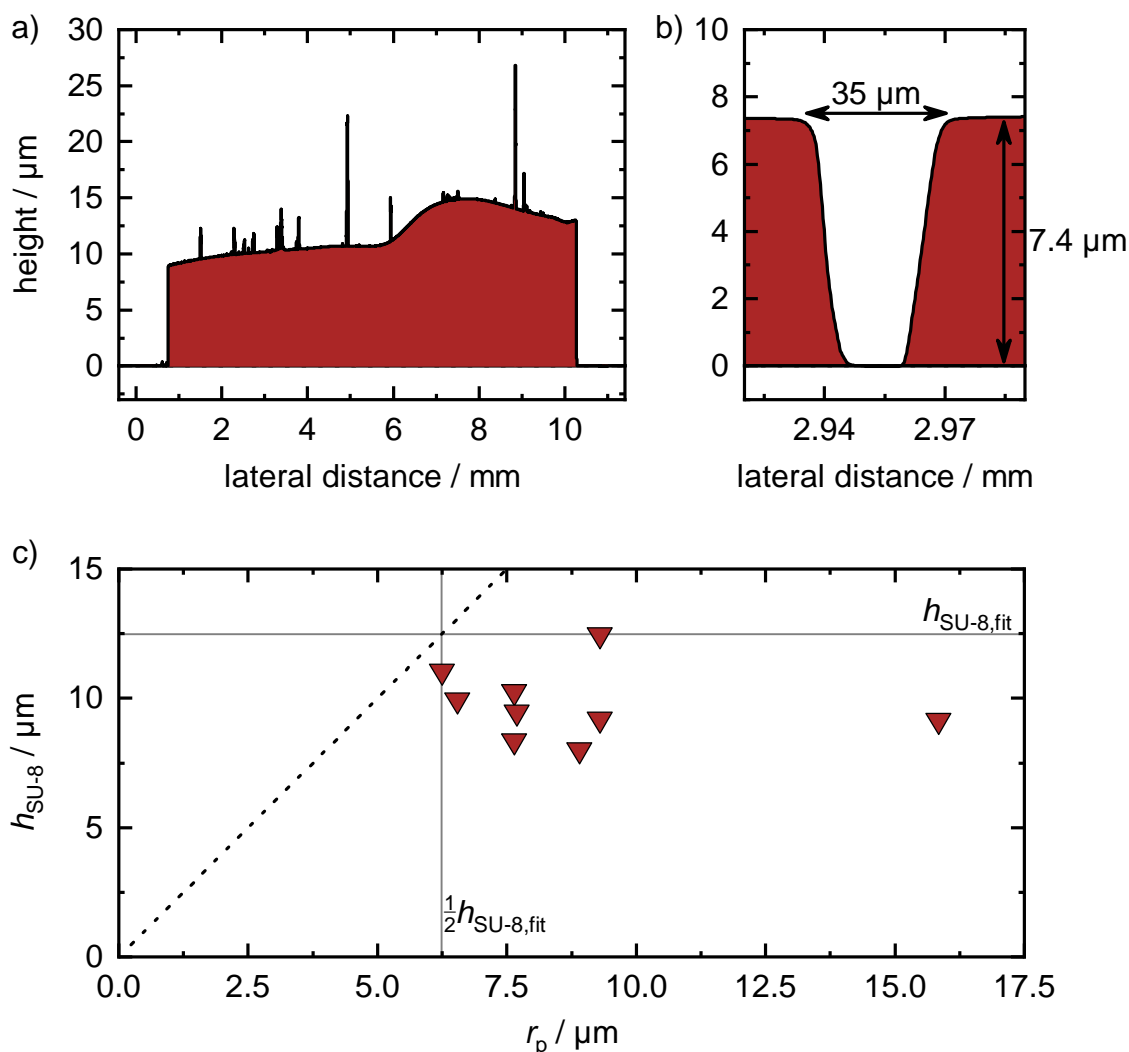


Figure S5: Height profile along the diagonal of a sample showing the unevenness of the SU-8 layer and peaks originating from NCM 111 secondary particles lying on top of its surface (a), height profile of an empty particle trap revealing the penetration of the SU-8 layer (b) and approximate height of the SU-8 layer near the positions of the particle traps containing single NCM 111 secondary particles of different size (c).

References

- (1) Dreizler, A. M.; Bohn, N.; Geßwein, H.; Müller, M.; Binder, J. R.; Wagner, N.; Friedrich, K. A. Investigation of the Influence of Nanostructured $\text{LiNi}_{0.33}\text{Co}_{0.33}\text{Mn}_{0.33}\text{O}_2$ Lithium-Ion Battery Electrodes on Performance and Aging. *J. Electrochem. Soc.* **2018**, *165* (2), A273–A282.

- (2) Cui, Y.; Björk, M. T.; Liddle, J. A.; Sönnichsen, C.; Boussert, B.; Alivisatos, A. P. Integration of Colloidal Nanocrystals into Lithographically Patterned Devices. *Nano Lett.* **2004**, *4* (6), 1093–1098.
- (3) Prevo, B. G.; Velev, O. D. Controlled, Rapid Deposition of Structured Coatings from Micro- and Nanoparticle Suspensions. *Langmuir* **2004**, *20* (6), 2099–2107.
- (4) Ni, S.; Leemann, J.; Wolf, H.; Isa, L. Insights into Mechanisms of Capillary Assembly. *Faraday Discuss.* **2015**, *181*, 225–242.
- (5) Fabian, A.; Elm, M. T.; Hofmann, D. M.; Klar, P. J. Hierarchical Structures of Magnetic Nanoparticles for Controlling Magnetic Interactions on Three Different Length Scales. *J. Appl. Phys.* **2017**, *121* (22), 224303.
- (6) Melai, J.; Salm, C.; Smits, S.; Visschers, J.; Schmitz, J. The Electrical Conduction and Dielectric Strength of SU-8. *J. Micromech. Microeng.* **2009**, *19* (6), 1–7.
- (7) Moslehi, G. B.; Self, S. A. Current Flow across a Sphere with Volume and Surface Conduction. *J. Electrostat.* **1983**, *14* (1), 7–17.
- (8) Moslehi, G. B.; Self, S. A. Electromechanics of Precipitated Particulate Layers. *IEEE Trans. Ind. Appl.* **1984**, *IA-20* (6), 1598–1606.
- (9) McLean, K. J. Cohesion of Precipitated Dust Layer in Electrostatic Precipitators. *J. Air Pollut. Control Assoc.* **1977**, *27* (11), 1100–1103.
- (10) Ruther, R. E.; Callender, A. F.; Zhou, H.; Martha, S. K.; Nanda, J. Raman Microscopy of Lithium-Manganese-Rich Transition Metal Oxide Cathodes. *J. Electrochem. Soc.* **2014**, *162* (1), A98–A102.
- (11) Lanz, P.; Villeveille, C.; Novák, P. Ex Situ and in Situ Raman Microscopic Investigation of the Differences between Stoichiometric LiMO_2 and High-Energy $x\text{Li}_2\text{MnO}_3 \cdot (1-x)\text{LiMO}_2$ ($M = \text{Ni}, \text{Co}, \text{Mn}$). *Electrochim. Acta* **2014**, *130*, 206–212.
- (12) Otoyama, M.; Ito, Y.; Hayashi, A.; Tatsumisago, M. Raman Spectroscopy for $\text{LiNi}_{1/3}\text{Mn}_{1/3}\text{Co}_{1/3}\text{O}_2$ Composite Positive Electrodes in All-Solid-State Lithium Batteries. *Electrochemistry* **2016**, *84* (10), 812–814.
- (13) Jung, R.; Morasch, R.; Karayaylali, P.; Phillips, K.; Maglia, F.; Stinner, C.; Shao-Horn, Y.; Gasteiger, H. A. Effect of Ambient Storage on the Degradation of Ni-Rich Positive Electrode Materials (NMC811) for Li-Ion Batteries. *J. Electrochem. Soc.* **2018**, *165* (2), A132–A141.

Acknowledgments

In den vergangenen Jahren meiner Promotion hatte ich das Glück, viele Menschen kennenlernen zu dürfen und von vielen Menschen auf unterschiedlichste Art und Weise unterstützt und begleitet zu werden. All jenen Personen, die direkt oder indirekt zu dieser Arbeit beigetragen haben, möchte ich an dieser Stelle gerne meinen herzlichen Dank dafür aussprechen! Mein besonderer Dank gilt:

- meinem Betreuer Prof. Dr. Peter J. Klar. Ich habe seine Arbeitsgruppe, die experimentellen Möglichkeiten, das Interesse in Besprechungen und Diskussionen, die wertvollen Kommentare und Ratschläge, das entgegengebrachte Vertrauen sowie seine Arbeitsweise und seine persönliche Art der Betreuung in den vergangenen 5 Jahren sehr zu schätzen gelernt.
- Prof. Dr. Jürgen Janek für die Bereitstellung von Geräten und Laboren, die produktiven Besprechungen, Anmerkungen zu Forschungsergebnissen und darüber hinaus sowie für die Übernahme des Zweitgutachtens.
- der Deutschen Forschungsgemeinschaft (DFG) für die Unterstützung im Rahmen des Graduiertenkollegs 2204 „Substitutionsmaterialien für nachhaltige Energietechnologien“ und dem Bundesministerium für Bildung und Forschung (BMBF) für die Unterstützung im Rahmen des Verbundprojekts „HiKoMat“ zum Themenschwerpunkt „Energiewirtschaftliche Schlüsselemente der Elektromobilität“, welche sowohl in wissenschaftlicher als auch in persönlicher und nicht zuletzt auch in finanzieller Hinsicht von großer Bedeutung waren.
- apl. Prof. Dr. Bernhard Lani-Wayda für das Interesse in den Besprechungen über die Modellierung von Diffusionsprozessen, die Einblicke in die Implementierung verschiedener Modelle in numerische Simulationsprogramme und schließlich auch für die Durchführung numerischer Simulationen von Diffusionsprozessen.
- Dr. Joachim R. Binder, Dr. Amalia C. Wagner und Nicole Bohn (Institut für Angewandte Materialien (IAM-ESS), Karlsruher Institut für Technologie (KIT)) für die Bereitstellung von Kathodenaktivmaterialien zur Untersuchung des Ladungstransportes in einzelnen Sekundärpartikeln sowie den regelmäßigen Austausch über experimentelle Ergebnisse.
- Markus S. Friedrich, Janis K. Eckhardt, Jan-Luka Dornseifer, Alexander G. Strack und Paul Tuchecker, deren Betreuung und Ergebnisse einen großen Teil meiner Promotion ausgemacht und stets zur Vertiefung des Verständnisses experimenteller Ergebnisse beigetragen haben. Die vielen Experimente, die im Rahmen unterschiedlicher

Projektarbeiten durchgeführt wurden sowie deren Besprechung haben den Erkenntnisgewinn maßgeblich mitbestimmt.

- Den Mitarbeitern der Feinmechanik- und der Elektronik-Werkstatt sowie Thomas Wasem für die gemeinsame Konstruktion der elektrochemischen Zelle zur Untersuchung des Ladungstransports in einzelnen Sekundärpartikeln, die Fertigung und die sukzessive Modifizierung der Zelle.
- Dr. Michael Ghidui für die Anmerkungen zur Korrektur dieser Arbeit.
- Julian Zahnw für den wissenschaftlichen und den nicht-wissenschaftlichen Austausch im Zusammenhang mit den vielen Projekt- und Statustreffen mit Projektpartnern sowie für das Korrekturlesen dieser Arbeit.
- Adrian Schürmann für den direkten, unkomplizierten und stets kompetenten Zugang zu experimentellen Möglichkeiten in den Laboren der AG Janek.
- Oleg Birkholz (Institut für Angewandte Materialien (IAM-WBM), Karlsruher Institut für Technologie (KIT)) und Markus Osenberg (Institut für Werkstoffwissenschaften und -technologien, Technische Universität Berlin) für die wissenschaftliche Zusammenarbeit und die angenehmen und unterhaltsamen Vorbesprechungen zu verschiedenen Treffen mit Projektpartnern.
- Sämtlichen Mitarbeitern und ehemaligen Mitarbeitern der AG Klar für die vielen Einblicke in Ansätze und Methoden zur Bearbeitung von mehr oder weniger verwandten Fragestellungen sowie das unterhaltsame und angenehme Arbeitsklima, welches sowohl während als auch zwischen den Arbeitszeiten stets hinreichend viele Möglichkeiten des Austausches bot.
- Max für die intensive Unterstützung und Beratung im Forschungsalltag, wertvollen Tipps zur Darstellung und Interpretation experimenteller Daten, die vielen wissenschaftlichen Diskussionen, die nicht allzu selten auch über wissenschaftliche Fragestellungen hinausgingen, die fast immer unbeschadete, oftmals kulinarisch wertvolle und zumeist kurzweilige und lehrreiche Begleitung auf mehr als 55.000 km Reisestrecke, die stets damit verbundene Thematisierung persönlicher Ängste davor, nie anzukommen und die vielen Einblicke in das schier unüberschaubare Gebiet der Dinge, die Viele ja gar nicht wissen.

Abschließend möchte ich meiner Freundin, meiner Familie und meinen Freunden für die großartige Unterstützung in sämtlichen Lebenslagen, das nicht enden wollende Verständnis, die gelegentliche Ablenkung und alles weitere danken, was mir geholfen hat, diese Arbeit anzufertigen.

DANKE!